Mohamed Bendaoud
Borutzky Wolfgang
Khalid Chikh *Editors*

The Proceedings of the International Conference on Electrical Systems & Automation

Control of Electrical and Electronic Systems—Volume 2

Springer

The Proceedings of the International Conference on Electrical Systems & Automation

Mohamed Bendaoud · Borutzky Wolfgang ·
Khalid Chikh
Editors

The Proceedings of the International Conference on Electrical Systems & Automation

Control of Electrical and Electronic Systems—Volume 2

Springer

Editors
Mohamed Bendaoud
ENSA Khouribga
Sultan Moulay Slimane University
Khouribga, Morocco

Khalid Chikh
ENSA Khouribga
Sultan Moulay Slimane University
Khouribga, Morocco

Borutzky Wolfgang
Bonn-Rhein-Sieg University of Applied Sciences
Sankt Augustin, Germany

ISBN 978-981-19-0038-9 ISBN 978-981-19-0039-6 (eBook)
https://doi.org/10.1007/978-981-19-0039-6

This Springer imprint is published by the registered company Springer Nature Singapore Pte Ltd.
The registered company address is: 152 Beach Road, #21-01/04 Gateway East, Singapore 189721, Singapore

Committees

Honorary Committee

Hmina Nabil, President of Sultan Moulay Slimane University, Morocco
Sajieddine Mohammed, Director of ENSA-Khouribga

General Chairs

Mohamed Bendaoud, Sultan Moulay Slimane University, Morocco
Khalid Chikh, Sultan Moulay Slimane University, Morocco

Conference Co-chairs

Elbarbri Noureddine, Sultan Moulay Slimane University, Morocco
Borutzky Wolfgang, Bonn-Rhein-Sieg University of Applied Sciences, Germany
Ailane Abdellah, Sultan Moulay Slimane University, Morocco

Publication Chairs

Mohamed Bendaoud, Sultan Moulay Slimane University, Morocco
Borutzky Wolfgang, Bonn-Rhein-Sieg University of Applied Sciences, Germany
Khalid Chikh, Sultan Moulay Slimane University, Morocco
Amine El Fathi, Abdelmalek Essaadi University, Morocco

Sponsorship Co-chairs

Benchagra Mohamed, Sultan Moulay Slimane University, Morocco
Khamlich Salahddine, Sultan Moulay Slimane University, Morocco
Amharech Amine, Sultan Moulay Slimane University, Morocco

Communication Co-chairs

Massour El Aoud Mohamed, Sultan Moulay Slimane University, Morocco
Rhofir Karim, Sultan Moulay Slimane University, Morocco
Maaider Kamal, Sultan Moulay Slimane University, Morocco

Technical Programme Chairs

Hihi Hicham, Sidi Mohamed Ben Abdellah University, Morocco
Lokriti Abdesslam, Sultan Moulay Slimane University, Morocco
Er Rachid Ismail, Sultan Moulay Slimane University, Morocco
Amer Ragab Zerek, Zawia University, Libya

Technical Programme Committee

Abouzahir Mohamed, Mohamed V University, Morocco
Abouobaida Hassan, Chouaib Doukkali University, Morocco
Afia Aziz, Hassan II University, Morocco
AlFaouri Yanal Shaher, University of Jordan, Jordan
Amer Ragab Zerek, Zawia University, Libya
Asmaa A. Abdeewi, Polymer Research Center, Libya
Ashok Suryawanshi, Pimpri Chinchwad College of Engineering, India
Barbosa Karina, University of Santiago, Chile
Belkacem Ould bouamama, Polytech of Lille, France.
Binti Mohamed Shah Noraisyah, Universiti Malaya, Malaysia
Boulghasoul Zakaria, Cadi Ayyad University, Morocco
Caines Peter, McGill University, Canada
Chuah joon huang, Universiti Malaya, Malaysia
Elbacha Abdelhadi, Cadi Ayyad University, Morocco
El Aamri Faicel, Hassan II University, Morocco
EL bahir Lhoussain, Cadi Ayyad University, Morocco
El akchioui Nabil, Abdelmalek Essaadi University, Morocco

Yame Julien, CRAN, Nancy, France
Elkari Badr, Euromed University of Fes, Morocco
Gonzalo M López, Faculty of Exact Sciences, Engineering and Surveying, Argentine
Huang Qi, University of Electronic Science and Technology, China
Jamleh Hani, University of Jordan, Jordan
Joao Martins, New University of Lisbon, Portugal
José Barata, New University of Lisbon, Portugal
Khafallah Mohamed, Hassan II University, Morocco
Luis M. Camarinha-Matos, New University of Lisbon, Portugal
Oumoun Mohamed, Cadi Ayyad University, Morocco
Hihi Hicham, Sidi Mohamed Ben Abdellah University, Morocco
Luiz Affonso H Guedes de Oliveira, Federal University of Rio Grande do Norte, Brazil
Marizan Binti Mubin, Universiti Malaya, Malaysia
Mohammad Aminul Islam, Universiti Malaya, Malaysia
Mohd Faiz Bin Mohd Salleh, Universiti Malaya, Malaysia
Rahmani Ahmed, Central School of Lille, France
Schmidt Michael, Offenburg University, Germany
Sheetal Bhandari, Pimpri Chinchwad College of Engineering, India
Varsha Harpale, Pimpri Chinchwad College of Engineering, India
Paplo Adasme, University of Santiago, Chile
Maan El Badaoui El Najjar, University of Lille, France
Borutzky Wolfgang, Bonn-Rhein-Sieg University of Applied Sciences, Germany
Alain Jaafari, ECAM-EPMI, Paris, France
Elourdi Abdelhafid, Paris-Saclay University, France

Preface

This book is the second part of two volumes on "**Control of Electrical and Electronic Systems**" and is a compilation of selected contributions to the International Conference on Electrical Systems & Automation (ICESA'21) which was held on 8–9 December 2021 at the National School of Applied Sciences of Khouribga, Morocco. This conference brings together researchers in industry and academia to exchange their ideas, applications, and innovative techniques in the field of renewable energy and electrical systems.

The book provides rigorous discussions, the state of the art, and recent developments in the modelling, simulation and control of power electronics, industrial systems, and embedded systems. The book will be a valuable reference for beginners, researchers, and professionals interested in control of electrical and electronic systems.

The conference programme featured a rich set of keynote session topics and tutorials that extend beyond the papers contained in this proceedings. There were six high-profile keynotes by eminent researchers: Prof. Yazami Rachid (*KVI Pte Ltd., Singapore*), Prof. Hachimi Hanaa (*Sultan Moulay Slimane University, Morocco*), Prof. Pierluigi Siano (*University of Salerno, Italy*), Prof. Michael Schmidt (*Offenburg University, Germany*), and Prof. Yousfi Driss (*Mohammed I University, Morocco*).

The editors express their gratitude to Springer Nature authority for publishing this volume in the Springer Conference Proceedings Series.

The editors also express sincere thanks to the reviewers for their dedication in reviewing the articles. Also, thanks to the authors for submitting their articles to this volume.

It is hoped that this volume will be a good reference manual for researchers and budding engineers.

Khouribga, Morocco — Mohamed Bendaoud
Sankt Augustin, Germany — Borutzky Wolfgang
Khouribga, Morocco — Khalid Chikh

Contents

About the Editors

Prof. Mohamed Bendaoud received the M.Sc. and Ph.D. degrees in Electrical Engineering from Cadi Ayyad University, Marrakech, Morocco, in 2012 and 2019, respectively. He is currently Assistant Professor at National School of Applied Sciences (ENSA) of Khouribga, Sultan Moulay Slimane University, Morocco.

He is Founder and General Chair of the International Conference on Electrical Systems & Automation. He has served and continues to serve on the technical programme committees and as reviewer of numerous international conferences and journals such as Journal of The Franklin Institute, Mechatronic Systems and Control. He is Editor-in-chief of the new ambitious *Journal of Electrical Systems & Automation* (JESA). He is Deputy Director of the science and technology laboratory for engineers.

His research interests include:

- Modelling and control of grid connection for photovoltaic and wind energy.
- Modelling and simulation methodologies for multidisciplinary systems, in particular bond graph-based.
- Control of power converters.

Prof. Borutzky Wolfgang is a retired professor for Modelling and Simulation of Engineering Systems at Bonn-Rhein-Sieg University of Applied Sciences, Germany. He obtained his University Diploma Degree in Mathematics in 1979 and his Doctoral Degree in Mechanical Engineering in 1985, both from the Technical University of Braunschweig, Germany.

He was Visiting Professor at universities in the Netherlands, the USA, France, and Argentina. Since 2008, he holds an honorary position as Associate Professor of Electrical Engineering and Information Technology at the University of Dubrovnik, Croatia.

His main research interests include modelling and simulation methodologies for multidisciplinary systems, in particular bond graph-based as well as object-oriented modelling; modelling, analysis, control, and fault diagnosis of mechatronic

systems and hybrid failure prognostic methods; modelling languages; and scientific computing and numerical algorithms for continuous system simulation.

He has published in the proceedings of many peer-reviewed international conferences on modelling and simulation and in refereed scientific journals. In 2019, he received the best paper award of the 12th International Conference on Integrated Modelling and Analysis in Applied Control and Automation (IMAACA 2019) in Lisbon, Portugal, which is part of the annual International Multidisciplinary Modelling & Simulation Multiconference (I3M).

He is author of a 2010 Springer monograph on bond graph methodology and of a 2015 Springer book on bond graph model-based fault diagnosis in hybrid systems. He is also Editor and Co-author of a 2011 Springer compilation text on Bond Graph Modelling of Engineering Systems and of a 2016 compilation text entitled Bond Graphs for Modelling, Control and Fault Diagnosis with contributions from experts in various fields from all over the world. His latest book published with Springer is titled Bond Graph Modelling for Control, Fault Diagnosis and Failure Prognosis. Furthermore, he was Guest Editor of two special journal issues on bond graph modelling.

Since 1990, he has served in many international scientific conferences on modelling and simulation in various capacities. In 2005, he was Assistant General Chair of the European Conference on Modelling and Simulation (EMCS) in Riga, Latvia, in 2006 he was General Chair of the ECMS 2006 in Sankt Augustin, Germany, and in 2013 he was Conference Chair of the IASTED Conference on Modelling, Identification, and Control (MIC 2013) in Innsbruck, Austria. From 2005 to 2007, he served on the Board of the European Council for Modelling and Simulation.

In 2009, he was an invited tutorial speaker of the IASTED Conference on Modelling, Simulation and Identification (MSI 2009) in Beijing, China, and in 2010, he was one of the invited keynote speakers to the Conference on Power Control and Optimisation (PCO 2010) in Kuching, Malaysia.

In 2012, he was one of the invited keynote speakers of a workshop on bond graph modelling in Pune, India, and one of the invited keynote speakers of the SCS Summer Simulation Multiconference in Genoa, Italy.

In 2013, he was an invited tutorial speaker of the IASTED Conference on Control and Applications (CA 2103) in Honolulu, USA, and one of the invited keynote speakers of the International Conference on Smart Technologies for Mechanical Engineering at Delhi Technological University (DTU), Delhi, India.

In 2018, he was one of the invited keynote speakers of the 1st International Conference on New Frontiers in Engineering, Science & Technology (NFEST 2018), New Delhi, India, and of the 1st International Conference on Electronics, Control, Optimization and Computer Science (ICECOCS'18), Kenitra, Morocco.

He has also served as an invited external examiner and as Member of Ph.D. defense committees in France, in India, in the UK, and in Norway. Moreover, he has given invited lectures and short courses in industry on bond graph modelling.

During the 2004–2006 biennium, he served on the SCS Board of Directors. He was also active as Member of the Editorial Board of some major modelling and

simulation-related journals. Since 2009, he is again Associate Editor of the journal Simulation: Transactions of the Society for Modeling and Simulation International.

Prof. Khalid Chikh obtained Post-Doctoral Degree (HDR) in electrical engineering for renewable energy from the Sultan Moulay Slimane University, Beni Mellal, Morocco; Ph.D. degree in electrical engineering from the National School of Electricity and Mechanics (ENSEM), Hassan II University, Casablanca, Morocco; and Diploma of Advanced Higher Studies (DESA) in electrical engineering from the Faculty of Science Semlalia, Cadi Ayyad University, Marrakesh, Morocco.

He is currently Associate Professor at the National School of Applied Sciences (ENSA) of Khouribga, Sultan Moulay Slimane University. Previously, he was Professor of electrical engineering and Deputy Director of Engineering and Applied Technology Laboratory (LITA) at the Higher Institute of Technology (EST), Sultan Moulay Slimane University. Previously, he was Automation and Electrical Maintenance Manager in OCP Company, Jorf Lasfar, Morocco. He is Automation and Electrical Energy Consultant. He is Director of the Science and Technology Laboratory for Engineers (LaSTI). He is General Chair of the first edition of the International Conference on Electrical Systems & Automation (ICESA'21). He is Technical Programme Committee TPC Member and reviewer of numerous international conferences and journals in the electrical engineering field. Current research interests are: advanced control of electrical machines and power electronic converters and control of the renewable energy power systems, smart grid, energy storage systems, batteries fast charging, and energy efficiency.

Recent Advances in Machine Learning and Deep Learning in Vehicular Ad-hoc Networks: A Comparative Study

Taib Chaymae, Haimoudi Elkhatir, and Abdoun Otman

Abstract The expanding population necessitates the development of solutions to make human life easier. Smart transportation plays an important role in society by improving road security, lowering mishap rates, and making the travel experience more valuable for passengers. As a result, the vehicular ad hoc network (VANET) provides communication between vehicles for exchanging information in order to improve traffic flow and ensure driving safety. However, the Vanet network has faced several challenges that have compromised the driver's privacy; thus, Machine learning and Deep learning contribute to enhance. We offer a detailed assessment of Artificial intelligence approaches being investigated by diverse research initiatives in the field of VANETs. We examine the benefits and drawbacks of these suggested AI-based methods for the VANET environment, in addition, we make a comparative analysis of some ML and AI algorithms based on four essential criteria. Finally, we highlight future VANET research areas that may fully use AI's capability.

Keywords Deep learning · Machine learning · Vanet network · Ad-hoc · Smart transportation · Smart city · Security · Artificial intelligence

1 Introduction

The growth of the population number which's according to the united nation we had reached 7.9 billion, China in the leads, with 1.4 billion population exceeded, this problem urges us to search for a way to improve security and reliability and comfort of traditional cities by developing smart cities. Thus, urban transportation is considered a big part of the enhancement of smart cities [1].

T. Chaymae (✉) · H. Elkhatir
Advanced Science and Technology Laboratory, Polydisciplinary Faculty, Abdelmalek Essaadi University, Larache, Morocco
e-mail: taib.chaymae@etu.uae.ac.ma

A. Otman
Computer Science Department, Faculty of Science, Abdelmalek Essaadi University, Tetouan, Morocco

M. Bendaoud et al. (eds.), *The Proceedings of the International Conference on Electrical Systems & Automation*, https://doi.org/10.1007/978-981-19-0039-6_1

The increasing number of accidents in the cities leads to several human lost pushes to improve the quality of transportation and that by strengthening the security and communication between the vehicles for better driving and more safety [2].

A VANET network, or vehicular ad hoc network, is a self-organized network that allows smart cars to communicate with one another in order to improve traffic flow and assure driving safety [3]. Despite the benefits of this solution, it still faces a number of issues in terms of security and privacy; the information exchanged in the cloud might lead to a number of assaults, compromising the driver's security [4]. Machine learning algorithms are strong tools that may assist in dealing with assaults as well as predicting a safe route with fewer collisions [5].

The main contributions of this paper include:

- We explored various AI approaches and highlighted their effectiveness as well as limits in solving various VANET difficulties and requirements.
- We conducted a comparison study of machine learning and deep learning algorithms based on four important criteria.

In this study, we present a survey about Vanet Ad-hoc network, we examined numerous AI approaches and evaluated their applicability as well as limits in solving various VANET difficulties and needs, we also highlight future research areas that need to be investigated further in order to fully integrate AI with VANET.

The rest of this paper is organized as follows. Section 2 an overview of Vanet and the types of communication. In Sect. 3, background on machine learning and deep learning. Section 4 presents the issue of the challenge of Vanet. Section 5 the application of each algorithm in Vanet area with their limitation. Section 6 presents a comparative study. Section 7 conclusions and future works.

2 Vehicular Ad-hoc Network

A vehicular ad hoc network (VANET) was created based on the principle of a Mobile Ad Hoc network (MANET) that gives the possibility to communicate between vehicle and its environment (nearby vehicles, road devices) for an exchange of information about traffic state for improving road safety and avoid the congestion in addition to entertainment systems. As shown in Fig. 1. The network provides three main communication nodes: On-board Units and On-road Side and Application Unit [6]:

- On Board Unit (OBU): An On-Board Unit (OBU) is OBU is a device that was mounted in every vehicle for receiving and transmission of information with other OBUs or RSUs.
- Application Unit (AU): An AU is a device installed inside the vehicle for the ability to transmit and receive information with OBU and it can be linked via a wireless medium or wired, in addition, AU could operate via normal devices.
- Road Side Unit (RSU): RSU is a wave device being placed all along the roadside or in an intersection or parking. It can help to prevent accidents and that with the

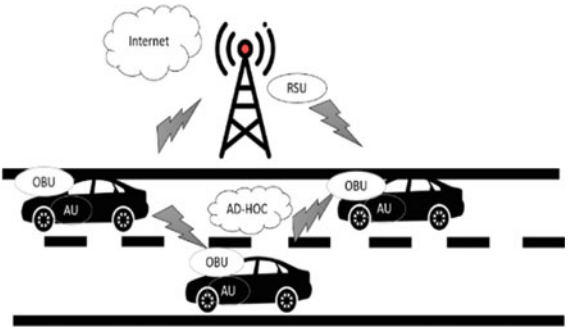

Fig. 1 The three communication nodes

fact the device connected to the internet will provide to the users the information in addition to their security.

2.1 Type of Communication System

The Vanet network allows vehicles to communicate with each other for safer and more comfortable driving. As a result of the exchange of information regarding road conditions, the Vanet has seven forms of communication, which we will unveil in the following paragraph:

- Vehicle to vehicle (V2V): it's a communication between vehicles to transmit and receive information about the road, for example, if there is an accident or jam or an ambulance.
- Vehicle to Infrastructure (V2I): The vehicle connected to RSU to be able to communicate with the infrastructure network like the internet.
- Vehicle to broadband cloud (V2B): technology of Vanet can't handle a large amount of data with different types (audios, videos, text), therefore Vanet uses Edge Cloud Computing for beneficial communication that can interconnect through 4G or 5G (wireless broadband mechanisms).
- Vehicle to everything (V2X): vehicle to everything is communication that enables to transmit and receive information between a vehicle with other vehicles, pedestrians, road infrastructure, and the Internet, to get a safer exchange, more coordinated, and smarter use of transportation networks.
- Intra-Infrastructure communication (I2I): Is a communication, gathering V2V and V2I. A vehicle may either exchange information with the roadside infrastructure in two ways: a single hop or multi-hop fashion.
- Vehicle-to-Sensor communication (V2S): vehicle to sensor connection provides communication between vehicles and miscellaneous sensors which are installed inside or out vehicles.

- Vehicle-to-Personal Device communication (V2PD): this connection allows the passenger to exchange information such as music and video between vehicle and portable devices

3 VANET and ML and DL: Background

3.1 Machine Learning Algorithms

Machine learning is the combination of statistics and algorithms models that teaches the machine how to benefit from data to produce a prediction or a decision. In this section we will present some of machine learning algorithms:

- Support vector machine learning: support vector machine is a supervised algorithm, SVM is a distinct of linear classifiers built on the principle of margin maximization that provides an improvement in the case of complexity, therefore, reach a better performance. The main task of SVM is to find the finer hyperplane that splits the data into two classes.
- Decision Tree: is a supervised machine learning, the goal of this method is to create a model that extracts features from data and makes a prediction for the value of a target variable of learning simple decision rules, DT is used in both classification and regression problems.
- Random forest: the random forest is based on a collection of plenty decision trees in the training and for the classification phase by the majority vote, the RF is simple to implement and fast and has proven its success in many fields.
- Principal component analysis: PCA is utilized in exploratory data analysis and predictive model development. It's the process of calculating the primary components and using them to change the basis of the data, sometimes simply using the first few and ignoring the rest. It's usually used to reduce dimensionality.
- K-Nearest Neighbor: KNN is a simple supervised learning technique that can be used in both classification and regression issues. It's also straightforward to comprehend and use, requiring no additional assumptions or tuning of multiple parameters. However, it becomes extremely slow when dealing with huge datasets. If the problem is a classification or regression, it works by calculating the distance between a query and all the data and selecting the one that is closest to the query, and then voting for the most frequent or averages label dependent.
- Reinforcement Learning (RL) is a type of machine learning issue in which the aim is to learn what to do based on previous experiences in order to discover the optimal answer. Reinforcement learning differs fundamentally from supervised and unsupervised learning in terms of the interactive and iterative aspects: the algorithm attempts many solutions (exploration), observes the reaction of the environment, and changes its behavior (the variables) to discover the optimal approach.

3.2 Deep Learning Algorithms

Deep Learning is a branch of machine learning, this subfield is inspired by the structure and function of the human brain in order to generate predictions using neural networks. In this section we will present some of the deep learning algorithms:

- Artificial Neural Networks: ANN Are multi-layer, fully connected neural nets that consist of an input layer, multiple hidden layers, and an output layer. Every node in one layer is linked to every other node in the next layer. We reinforce the network by increasing the number of hidden layers.
- Convolutional Neural Network: CNN is a type of feed-forward neural network in AI, it is commonly used in image recognition and feature extraction. CNN consists of five layers: the input layer, pooling layer, full-connection layers, and output layer.
- Recurrent Neural Network: RNN Is a sort of neural network containing loops that allow data to be stored inside the network. Recurrent Neural Networks employ reasoning from prior experiences to predict future events. Recurrent models are useful because they can chain vectors which enable the API to execute more complex tasks.
- Long Short-Term Memory: The control flow of an LSTM is much like that of a recurrent neural network. It processes data and forwards information as it propagates. The processes within the cells of the LSTM vary. The cell state and its numerous gates are at the heart of LSTMs. The cell state serves as a conduit for relative information to be sent all the way down the sequence chain.
- Deep Belief Network: Were developed as a solution to the issues faced when utilizing standard neural networks for deeply layered network training, such as sluggish learning, becoming trapped in local minima owing to poor parameter selection, and requiring a large number of training data sets.

4 Vehicular Ad-hoc Network Challenges

4.1 Security

The most serious issue for VANET is safety. Security capabilities include access protection, data management, traceability, and security, as well as revocability, availability, trustworthiness, transparency, repudiation, privacy, and confidentiality. The study [7] describes a methodology that raises vehicle driver's awareness of sidewalks near to crossings.

The suggested system connects roadside units (RSUs) to vehicles in order to transfer information concerning pedestrian presence through traffic. To avoid the transmission of misleading information, before sending out alert messages, RSUs sign them, and all cars may validate the signature. This imposes stringent safety requirements, such as not replicating warnings and the rigorous requirement for

real-time contact., such as with a minimum message confirmation period for cars entering a crosswalk of interest. To handle signed notifications, we suggest nimble asymmetric cryptography (NAC), which authenticates communications transmitted indirectly. NAC lowers the need for asymmetric coffers, which are necessary for ensuring non-productive usage but raise efficiency costs. Nandy et al. [8] proposed a two-factor authentication system based on device biometrics and passwords that would work in a minimal to no VANET network environment.

4.2 Privacy

The location of the driver should not be revealed due to privacy concerns. The VANET's privacy must be protected while the Transitions are part of the journey. The article proposes a dynamically adjustable k-anonymous (DAK) method and a null position (DLP) technique. Zheng et al. [9], Both of these are supported by the PP-OSGI. The DAK and DLP algorithms dynamically detect the locational degree of privacy protection in various settings, then select an anonymous group of adjacent cars to construct a fake location for the vehicle of the service application. According to the study, the verification of messages between automobiles and floor units is crucial for safety [10]. Before trusting the vehicle's nodes, it is necessary to encrypt and check messages between the vehicles, and only authorized parties can track down and reveal the identity of the original nodes. Authentication between vehicles, on the other hand, does not ensure an accurate rate of message authentication.

4.3 Routing Issue

In VANET, there are three major routing algorithms: opportunistic forwarding, trajectory-based forwarding, and geographic forwarding. In [11] the authors developed a notion for a zoom-out broadcast routing system to provide safety information to drivers on VANET networks. In Zebra, a technique for identifying messages for neighbors is suggested, which employs a very simple strategy of employing one-hop extremely intelligently depending on vehicle speed and distance to distinguish a front, a vehicle, and a rear vehicle.

4.4 Data Dissemination

In circumstances where the network or VANET system is unavailable, two delivery options should be considered: relaying and flooding. The flooding strategy usually leads to high communication traffic. As a result, avoiding the transmission storm problem is a major challenge for this method [12]. Several studies have been carried

out on VANET to highlight the need for privacy and protection. The focus was on verification, identification, and prevention of misbehavior, as well as location privacy and certificate withdrawal. In [13], The two-tier VANET/p2p technique is essentially the integration of two different systems used for information sharing in vehicles ad hoc (VANET) to maintain a small-scale delay. The quest's success rate can be increased due to high peer-to-peer (p2p) communication.

The proposed approach makes use of accessibility from a distance. Accessibility maintains the success rate at a low level and reduces the search latency. Another study [14] offered a unique data distribution strategy centered on clustering and probabilistic broadcasting (CPB), In which a clustering method is offered for the first time based on vehicle directions, and vehicles swap their data in clustered form with appropriate connection time.

4.5 Real Time System

The emergence of real-time gadgets is being stifled by the mobility sector. As a result, it is difficult to transmit alerts to other devices at the proper time before the time limit [15]. The researcher introduced (MRS) secure data aggregation on real-time traffic Vehicle cloud approach at VANETs employing the data recovery property in the message recovery signature in [16].

5 The Application of ML and DL Algorithms in VANET Areas

5.1 The Application of Machine Learning Algorithms:

Machine learning assists the Vanet network with a variety of challenges that might be dangerous and difficult for drivers, including the identification of threats using the support machine learning (SVM) and random forest (RF) algorithms. And that provides security to drivers and protects their transmission from attackers. Also aids with traffic flow and prevent a traffic jam by detecting the accident traffic and that can help the drivers to make an early decision for a better path. Reinforcement learning is also used to aid with routing choice issues. in addition to enhancing network slicing the V2X communication. Machine learning has improved the performance of the Vanet network and that is shown in Table 1, which describes the use of each method in the Vanet area as well as its limitations.

Table 1 The application of machine learning on Vanet area and their limitation

Machine learning algorithm	Their application	Limitation
Support vector machine learning	• Predicting a road safety • Improve the performance of Vanets • Achieved a secure transmission of big data through Vanets • Detect DDOS attacks	• Less suitable for highway areas • SVM-based models are difficult to understand and perceive
Decision trees	• Predicting a road safety • Detect malware traffic	• Require private information • Drop in the storage requirement • Difficult when a large number of Dts are necessary
Random forest	• Detect known network intrusions • Traffic accident detection • Identifying attacks • Control channel placement	• Took a lot of time when there is a large amount of data • Security challenge
Reinforcement learning	• Routing decision problems • Enhance network slicing for V2X communications • Effective for difficult vehicle mobility • Improves dynamic and equitable spectrum allocation for multiple access via vehicular channels • Driving prediction	• Reinforcement learning necessitates a huge quantity of data as well as extensive processing • Furthermore, when applied in actual physical systems, the huge quantity of characteristics might be a major challenge for reinforcement learning
K-means clustering	• This algorithm is the most used to divide the vehicles into a clusters • Solve data congestion problem • Decrease packet loss and end-to-end delay	• The number of clusters is fixed • Inefficient for stability and cluster lifetime because of the initial centroids are set on first come first serve basis • Security issue
KNN	• Predicting a road safety • Identifying attacks • Mentioning how many successful internal interferences attempts appear and when protects privacy • Can aid in the maintenance of stable clusters for vanet cluster-based methods • Detection of vehicles and incidents	• The optimal value of k changes from one dataset to the next; consequently, determining the optimal value of k may be a complex and time-consuming task

(continued)

Table 1 (continued)

Machine learning algorithm	Their application	Limitation
PCA	• Identify driving dangers and forecast denial of service (dos) attacks • Optimization of vehicular multimedia data caching in vehicle-to-everything communications	• In order to create a high-performance approach, the feature-pruning strategy must be used with other machine learning techniques

5.2 The Application of Deep Learning Algorithms

In this part, we will discuss some of the applications of DL in the Vanet field, as we noted Deep Learning (DL) has gained a lot of attention, especially with the considerable benefits that it provided, and it is commonly used in many sectors to enhance the performance of earlier techniques. Because DL-based approaches automatically extract and choose features from raw data, they can avoid the time-consuming effort of selecting features and gathering private information. In several studies, we found that they used CNN for the feature extraction and also combined it with other algorithms to achieve better performance. As we can see in Table 2, which highlights the benefits of applying each deep learning approach in the Vanet field, some of their restrictions are also stated.

There are other algorithms besides those mentioned in the preceding tables that help Vanet network to make intelligent decisions and behave wisely in the event of a car collision or accident in addition to Find the shortest path (SP) from the source to the destination in a reasonable amount of time, such as Bat Algorithm, Simulated Annealing, Genetic Algorithm that is an excellent method for dealing with complicated optimization problems with tough restrictions and network topologies. [17, 18] in addition to solving the routing issue in an Ad Hoc network large map is to determine the shortest feasible distance between a transmitter head (cluster, node, intermediate, or advanced) and the base station [19].

6 Comparative Study

Recently, the world relied on smart transportation that provides comfortable, easy, and safe driving and avoids accidents and human losses. The communication between vehicles offers information about traffic jams, accidents, emergency vehicles, therefore, this exchange can be threatening to the driver's private especially that the information be uploaded to the cloud and every user can access this information and use it to attack the vehicle for stealing goal or for another.

Table 2 The application of deep learning on Vanet area and their limitation

Deep learning algorithm	Their application	Limitation
ANN	• Predicting a road safety • Improve the communication reliability • Increasing the throughput and decreasing the packet dropping rate • Improve the performance • Used and deployed on the vehicles for the detection of dos attack, detection of black hole attack	• It should be used with other machine learning techniques for improved performance
CNN	• Feature extraction spatial and temporal • Estimate network traffic precisely • Traffic congestion prediction • The processed of the multimedia data gathered from roadside devices or the vehicle's control camera	• Execution time • Size of inputs • Insufficient in on-line anomaly detection • Difficult to deploy
RNN	• Detection of obstacles • Enhances mobility forecasting • Intelligence sharing via collaborative edge, fog, and cloud computing	• The primary disadvantage of RNN is the problem of gradients expanding or bursting which occurs during the training phase
LSTM	• Efficient anomaly detection solution for dos, XSS, SQL attacks • Traffic congestion prediction	• The slowest • Overfitting problem • Complexity when more feature added
Deep belief network	• Feature extraction • Predicting driver emotions • Preventing attacks • Estimating the trip duration	• Because of the huge number of variables, dbns have a lengthy startup stage

The researchers look for solutions to the vulnerabilities of the security in the Vanet network and for ensuring the changing of information without the threat of the attackers; thus, machine learning techniques can be the tool to enhance the performance of prediction threats and restrict it.

In this section, we compare machine learning and deep learning algorithms based on four criteria: fastest, a large amount of data because this exchange gathers a lot of different types of data in a short period of time, number of nodes, which refers to the number of vehicles that can be connected, and finally the performance of each algorithm. The outcome of the comparison is provided in Table 3.

k-Nearest Neighbor is one of the most basic classification approaches, needing no prior knowledge of data distribution. Since KNN is ideal for minor problems, the

Table 3 Numerical result of the comparative study

Algorithms	Large amount of data	Numbers of nodes	Fastest	Performance	Accuracy (%)
KNN	–	–	+	+	94.25
RF	+	+	–	+	95.02
DT	–		–		
LSTM				+	81
RNN	–			+	99.35
CNN + GRU	+			+	
SVM	+		–	+	99.95
LR				+	

training data must be retained in memory [20]. Yi Zeng et al. use KNN to detect the performance on real-life malware traffic using dataset ISCX2012 is achieved a good performance but met a drop in the storage requirement, and has a limited node, the IDS size limited too [21]. Prinkle Sharma et al. proposed an approach to target CAV by deceiving its ML model used on training data time-series K-Nearest Neighbor (KNN) and Random Forest was close to perfect by achieving AUC = 94.25 and 95.02 [22]. Usman Ahmad et al. in their work shows the training speed and prediction speed respectively, thus 1 and 2 ms, for KNN [23].

The Support Vector Machine is a method that uses a named training set to learn to categorize data points. The SVM is the ideal choice for binary classification, is capable of processing data sets with very large dimensions, and is memory efficient. However, it might be difficult to comprehend its parameters [24]. Menaka Pushpa Create a lightweight, adaptable, and efficient intrusion detection system for known and unknown UAV threats using a deep learning method with a multiclass SVM, it achieved better performance than multiclass SVM [25]. Usman Ahmad et al. examined the decision tree, SVM, and KNN methods to evaluate the machine learning model the result shows a reduced training speed and prediction speed respectively, namely 9 and 1 ms, for SVM [23]. Joe Diether Cabelin et al. used Support Vector Machines to categorize the packet as either safe or dangerous and it achieved high accuracy under two conditions: no traffic jam and jam. Ability to minimize the RMSE of the average distance between cars [26].

In addition, the IDS's attack detection time is sufficient for truck platooning. LSTM recurrent neural network is the best algorithm for sequential data. Ahmad et al. [23] provide in their research that LSTM recurrent neural network can identify authentic drivers using three driving characteristics, it achieved an accuracy of 81% ± 7.5%. Ying Gao et al. proposed an etude on attack prediction using random forest reached the accuracy rate of 99.95% and 98.75% in two data sets and compare it to SVM and logistic regression, the random forest was the best performing [27].

Hiroki Suda et al. employed a recurrent neural network to extract time-series features capable of recognizing typical intrusion assault methods such as data manipulation and injection attempts. If the data is small, it achieves a decent performance

[28]. In the investigation of urRehman et al. [29], RNN obtained 99.35 percent accuracy in NTP attacks. Abdul Rehman Javed et al. employed the CNN algorithm to identify attacks, and it outperformed the gated recurrent unit (GRU) on a dataset containing 2,369,868 Attack-free state messages [30].

7 Conclusion

In this study, we provided a global view of the Vanet network and the most significant challenges that it faced, as well as described various machine learning and deep learning techniques and their application in the Vanet area; and the enhancements that these solutions offered to the Vanet network for better driving and security. In addition, we discuss some of the algorithm's drawbacks. Based on four important criteria, we conduct a comparative analysis of several ML and AI algorithms, for future work, we may use this study to address the limitations of these algorithms and aim to employ a big data framework to avoid resource saturation, as well as to speed up the training and prediction stages, which would assist the drivers to have a safe and enjoyable driving experience.

References

1. Feizi, A., Joo, S., Kwigizile, V., Oh, J.S.: A pervasive framework toward sustainability and smart-growth: assessing multifaceted transportation performance measures for smart cities. J. Transp. Health **19**, 100956 (2020)
2. Goyal, S.B., Bedi, P., Kumar, J.: Realtime accident detection and alarm generation system over IoT. In: Multimedia Technologies in the Internet of Things Environment, vol. 2, pp. 105–126. Springer, Singapore (2022)
3. Engoulou, R.G., Bellaïche, M., Pierre, S., Quintero, A.: VANET security surveys. Comput. Commun. **44**, 1–13 (2014)
4. Hamdi, M.M., Audah, L., Rashid, S.A., Mohammed, A.H., Alani, S., Mustafa, A.S.: A review of applications, characteristics and challenges in vehicular ad hoc networks (VANETs). In: 2020 International Congress on Human-Computer Interaction, Optimization and Robotic Applications (HORA), pp. 1–7. IEEE (2020, June)
5. Mchergui, A., Moulahi, T., Zeadally, S.: Survey on Artificial Intelligence (AI) techniques for Vehicular Ad-Hoc Networks (VANETs). In: Vehicular Communications, 100403 (2021)
6. Goyal, A.K., Tripathi, A.K., Agarwal, G.: Security attacks, requirements and authentication schemes in VANET. In: 2019 International Conference on Issues and Challenges in Intelligent Computing Techniques (ICICT), vol. 1, pp. 1–5. IEEE (2019, September)
7. Branquinho, J., Senna, C., Zúquete, A.: An efficient and secure alert system for vanets to improve crosswalks' security in smart cities. Sensors (Switzerland) **20**(9), 1–26 (2020). https://doi.org/10.3390/s20092473
8. Nandy, T., Bin Idris, M.Y.I., Noor R.M., Ahmedy, I., Bhattacharyya, S.: An enhanced two-factor authentication protocol for V2V communication in VANETs, pp. 171–176 (2020). https://doi.org/10.1145/3388176.3388185
9. Zheng, Y., Luo, J., Zhong, T.: Service recommendation middleware based on location privacy protection in VANET. IEEE Access **8**, 12768–12783 (2020). https://doi.org/10.1109/ACCESS.2020.2964422

10. Rengarajan, A., Thaha, M.M.: SPCACF: secured privacy-conserving authentication scheme using cuckoo filter in VANET. Scalable Comput.: Pract. Experience **21**(1), 101–105 (2020)
11. LeBrun, J., Chuah, C.N., Ghosal, D., Zhang, M.: Knowledge-based opportunistic forwarding in vehicular wireless ad hoc networks. IEEE Veh. Technol. Conf. **61**(4), 2289–2293 (2005)
12. Rashid, S.A., Audah, L., Hamdi, M.M., Alani, S.: Prediction based efficient multi-hop clustering approach with adaptive relay node selection for VANET. J. Commun. **15**(4), 332–344 (2020). https://doi.org/10.12720/jcm.15.4.332-344
13. Verma, A., Pal, R., Prakash, A., Tripathi, R.: Information retrieval in two-tier VANET/P2P using RSU as a superpeer. Wirel. Commun. Technol. **2**(1), 1–9 (2018). https://doi.org/10.18063/wct.v2i1.456
14. Liu, L., Chen, C., Qiu, T., Zhang, M., Li, S., Zhou, B.: A data dissemination scheme based on clustering and probabilistic broadcasting in VANETs. Veh. Commun. **13**, 78–88 (2018). https://doi.org/10.1016/j.vehcom.2018.05.002
15. Samara, G., Al-Salihy, W.A.H., Sures, R.: Security issues and challenges of vehicular ad hoc networks (VANET). In: NISS2010—4th International Conference New Trends Information Science Service Science, pp. 393–398 (2010)
16. Shen, J., Liu, D., Chen, X., Li, J., Kumar, N., Vijayakumar, P.: Secure real-time traffic data aggregation with batch verification for vehicular cloud in VANETs. IEEE Trans. Veh. Technol. **69**(1), 807–817 (2020). https://doi.org/10.1109/TVT.2019.2946935
17. Khankhour, H., Abouchabaka, J., Abdoun, O.: Genetic algorithm for shortest path in ad hoc networks. In: Ezziyyani, M. (eds.) Advanced Intelligent Systems for Sustainable Development (AI2SD'2019). AI2SD 2019. Lecture Notes in Networks and Systems, vol. 92. Springer, Heidelberg (2020)
18. Khankhour, H., Abouchabaka, J., Abdoun, O.: Parallel genetic approach for routing optimization in large Ad hoc networks. Int. J. Electr. Comput. Eng. (IJECE) **12**(1), 748–755 (2022). https://doi.org/10.11591/ijece.v12i1.pp748-755
19. Khankhour, H., Abdoun, O., Abouchabaka, J.: Optimization of the ad hoc network by using hybridization of genetic algorithm with a two-optimization algorithm. In: Motahhir, S., Bossoufi, B. (eds.) Digital Technologies and Applications. ICDTA 2021. Lecture Notes in Networks and Systems, vol. 211. Springer, Heidelberg (2021)
20. Wiyono, S., Abidin, T.: Comparative study of machine learning KNN, SVM, and decision tree algorithm to predict student's performance. Int. J. Res.-Granthaalayah **7**(1), 190–196 (2019)
21. Zeng, Y., Qiu, M., Zhu, D., Xue, Z., Xiong, J., Liu, M.: Deepvcm: a deep learning-based intrusion detection method in vanet. In: 2019 IEEE 5th International Conference on Big Data Security on Cloud (BigDataSecurity), IEEE Intl Conference on High Performance and Smart Computing, (HPSC) and IEEE Intl Conference on Intelligent Data and Security (IDS), pp. 288–293. IEEE (2019, May)
22. Sharma, P., Austin, D., Liu, H.: Attacks on machine learning: adversarial examples in connected and autonomous vehicles. In: 2019 IEEE International Symposium on Technologies for Homeland Security (HST), pp. 1–7. IEEE (2019, November)
23. Ahmad, U., Song, H., Bilal, A., Alazab, M., Jolfaei, A.: Securing smart vehicles from relay attacks using machine learning. J. Supercomput. **76**(4), 2665–2682 (2020)
24. Tuttle, J.F., Blackburn, L.D., Powell, K.M.: On-line classification of coal combustion quality using nonlinear SVM for improved neural network NOx emission rate prediction. Comput. Chem. Eng. **141**, 106990 (2020)
25. Arthur, M.P.: Detecting signal spoofing and jamming attacks in UAV networks using a lightweight IDS. In: 2019 International Conference on Computer, Information and Telecommunication Systems (CITS), pp. 1–5. IEEE (2019, August)
26. Cabelin, J.D., Alpano, P.V., Pedrasa, J.R.: SVM-based detection of false data injection in intelligent transportation system. In: 2021 International Conference on Information Networking (ICOIN), pp. 279–284. IEEE (2021, January)
27. Gao, Y., Wu, H., Song, B., Jin, Y., Luo, X., Zeng, X.: A distributed network intrusion detection system for distributed denial of service attacks in vehicular ad hoc network. IEEE Access **7**, 154560–154571 (2019)

28. Suda, H., Natsui, M., Hanyu, T.: Systematic intrusion detection technique for an in-vehicle network based on time-series feature extraction. In: 2018 IEEE 48th International Symposium on Multiple-Valued Logic (ISMVL), pp. 56–61. IEEE (2018, May)
29. Rehman, S., Khaliq, M., Imtiaz, S.I., Rasool, A., Shafiq, M., Javed, A.R., Bashir, A.K.: DIDDOS: an approach for detection and identification of Distributed Denial of Service (DDoS) cyberattacks using Gated Recurrent Units (GRU). Futur. Gener. Comput. Syst. **118**, 453–466 (2021)
30. Rehman, A., Rehman, S.U., Khan, M., Alazab, M., Reddy, T.: CANintelliIDS: detecting in-vehicle intrusion attacks on a controller area network using CNN and attention-based GRU. IEEE Trans. Netw. Sci. Eng. (2021)

Prediction of Electricity Consumption by Using Long Short-Term Memory Neural Networks

Mohammed Bouafia, Azeddine El-Hammouchi, Amine El Fathi, and Nabil El Akchioui

Abstract In order to control the evolution of electrical power and satisfy the needs in the future, taking into account the economic and environmental conditions, with an aim of carrying out a sustainable development, the forecast of electricity consumption is obvious. The main objective of this work is to forecast the electricity consumption of two potable water stations. The first one is a pumping station with a low-voltage meter and the second one is a treatment station with a medium-voltage meter. In this context, a medium-term prediction model based on LSTM neural networks, programmed by python language is developed. In fact, we built several models in order to find the optimal one for all types of electrical consumption. Initially, we compared different architectures of neural networks by modifying the number of transition layers and numbers of neurons by each layer. The architecture with 4 intermediary layers and 50 neurons per layer gives the weakest indicator of variation. For the forecast of the pumping station consumption, we built 3 models, a mono-variable model and two multi-variable modes, using the mentioned architecture above. The multi-variable model based on 5 variables (history of consumption, days, seasons, temperature, and precipitation) is the most accurate. For the treatment's station consumption, 8 models in total were built. We forecast the total energy in the day and the energy in some specific times (Night energy, Day energy, Peak energy). The multi-variable models are considered as the optimal model to use.

Keywords Artificial intelligence · Electricity consumption prediction · Long Short-Term Memory (LSTM) · Medium term prediction model

1 Introduction

It appears very difficult to live today without electricity, which is present in all daily activities of life. Its consumption goes hand in hand with the improvement of the

M. Bouafia (✉) · A. El-Hammouchi · A. El Fathi · N. El Akchioui
LRSDI Laboratory Faculty of Sciences and Technology Al Hoceima, University Abdelmalek Essaadi, Tetouan, Morocco
e-mail: mohammed.bouafia@etu.uae.ac.ma

M. Bendaoud et al. (eds.), *The Proceedings of the International Conference on Electrical Systems & Automation*, https://doi.org/10.1007/978-981-19-0039-6_2

quality of inhabitant's life, the creation of the richness and the development of leisure, etc.

The electricity consumption in the world reached 22,848 TWh in 2019 with an increase of 1.7% compared to 2018 [1]. This evolution is due to the economic and industrial development, with the demographic growth, also the propagation of the electrical supply networks [2].

In Morocco, the electric power consumed in 2019, by the administrative sector knew an increase of 5.4%. In the industrial sector, the electricity demand decreased by −13.1% compared to the year 2018. The consumption of the residential sector in 2019 reached 5751 GWh, which represents an increase from 4.9% compared to the previous year [3].

The increase in electric consumption in the whole world requires the introduction of reliable methods to forecast electric consumption, to control its evolution, and to satisfy the needs for the future while holding into account the economic and environmental conditions with an aim of carrying out a sustainable development [4]. This forecast can be classified into 4 categories according to a horizon of time [2].

- Very short term: lower than one hour.
- Short term: between one hour and two weeks.
- Medium term: between two weeks and 1 year.
- Long term: superior to one year.

Indeed, the forecast of electricity consumption is the simulation of the evolution of this variable. In order to be close to the actual values, this simulation must take several inputs into consideration such as: the history of given consumption, the calendar and weather data [5].

In the intent to create the optimal model, the researchers do not cease improving forecast methods of electric consumption. Among the 128 methods used to forecast electricity consumption, it is often found that they are conventional or based on artificial intelligence. The latter is the most used with a percentage of 48% [6].

For the conventional models, we find the analysis of time series models, the models of regression, and the Gray models. The models based on artificial intelligence are often models of machine learning and the majority are models of neural networks or vector support machine. Figure 1 summarizes the distribution of the 128 forecasting models of electric consumption [6].

The methods of forecast based on machines learning gave great accuracy compared to other methods due to their capacity of processing big data. In this framework, the neural networks, occupy their place as much as one of the most adequate for time series analysis and forecasting. Long Short-Term Memory (LSTM) gave reliable and accurate models for the forecast of electric consumption [7].

The recurrent neural networks (RNN) suffer from the problem of vanishing gradients. In fact, the gradient decreases with time. LSTM is used to overcome this problem [8]. Also, it gives best results than Gated Recurrent Units (GRU) [9].

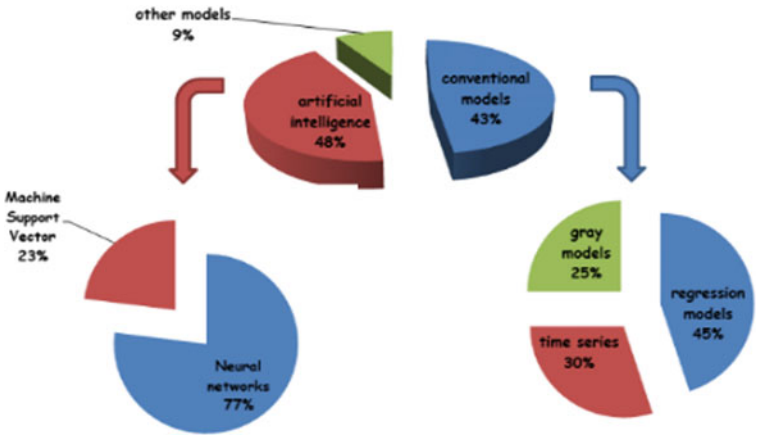

Fig. 1 Distribution of electricity consumption forecast models

2 Methodology

2.1 Introduction

In order to be able to build deep learning models with Python, it is necessary to create an environment in Anaconda and install TensorFlow and Keras library as well as Spyder IDE which is free and open-source scientific environment written in Python. TensorFlow is an end-to-end platform that makes it easy to create and deploy automatic learning models. Keras is a Deep learning application programming interface (API) [10].

2.2 LSTM Architectures

In LSTM there are several architectures either by the number of intermediate layers, or the number of neurons per layer, or by the number of inputs and outputs, or by the time step model takes to give us the first prediction value (single step or multi-step).

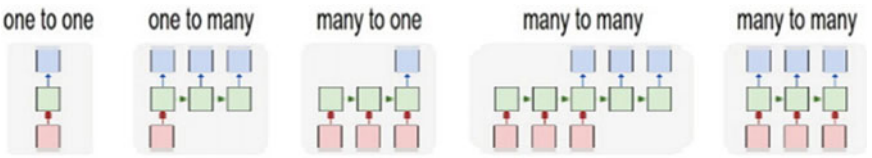

Fig. 2 LSTM network architectures

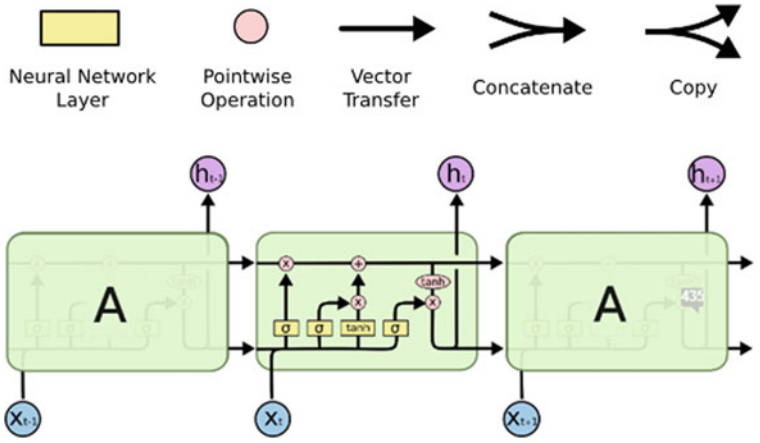

Fig. 3 Structure of an LSTM neural network

Figure 2 summarizes all possible architectures: one-to-one, one-to-many, many-to-one, many-to-many [11].

2.3 LSTM Neural Networks

LSTMs also have the same flow structure, but the repetitive module has a different structure (as shown in Fig. 2). Instead of having a single layer of the neural network, there are four, interacting in a very special way, which gives the ability to remove or add information about the cell state [10, 11].

Each line carries an entire vector from the output of one node to the inputs of the others. The pink circles represent point operations, such as vector addition, while the yellow boxes are learned neural network layers. The merging of lines indicates concatenation, while a fork in a line indicates that its contents are copied and the copies go to different locations (Fig. 3) [12].

2.4 Input Data

Data to Compare Architectures. The data that is used for the neural network training is collected from 20 households in the UK in the Loughborough area during the period between 2013–2014 from Wednesday 9 October 2013 13:06:17 to Saturday 4 January 2014 02:26:46 [9, 13]. The collection script is interrogated every 6–8 s based on the sensors installed in each house. We used the data from a single household to compare different architectures.

Low Voltage and Medium Voltage Meter Data. The data of two drinking water stations located in Morocco are used. The first one is a pumping station supplied with electrical energy by a low voltage meter, while the second is a treatment station supplied with electrical energy by a medium voltage meter. For the prediction of the consumed energy by each station, we built several models (mono-variable and multi-variable).

Guenfouda pumping station. The village of Guenfouda is located east of the city of Oujda at about 27 km. It is supplied with drinking water from a borehole that is operated by the National Office of Electricity and Drinking Water Branch (ONEE-BO), in order to fill a reservoir with a storage capacity of 300 m^3 with a flow rate of 7 l/, to meet the water needs of about 1000 subscribers as well as a small industrial zone.

We have collected the daily power consumption from 1/03/2019 to 30/04/2020. The data of month 5 is used as a test data to compare the predicted and actual values.

Beni Bouayach Treatment Plant. The Beni Bouayach treatment plant was built in 1985 and it is one of ONEE-BO's main sources of drinking water with a treatment flow rate of 400 l/s. It supplies the inhabitants of the province of Al-Hoceima.

The measured values (total energy, daytime energy, peak energy and nighttime energy) are taken every day at 10 AM from the voltage meter. The readings from 01/01/2018 to 31/02/2019 are used to forecast the daily energy consumption and energies for each time during month 3.

2.5 Forecasting Organigram

The implementation of an LSTM model for power consumption forecasting can be translated into the following flowchart (Fig. 4).

3 Results

3.1 Choice of Architecture

We have tried to build LSTM models with different random architectures. The comparison of these latters allows us to know the optimal architecture for power consumption prediction.

In the first stage, the number of intermediate layers is fixed and the number of neurons in each layer is varied. In the second stage, the number of intermediate layers is varied.

Comparison of architectures with a fixed number of intermediate layers. All the models are based on the consumption history recorded by the sensors and they are composed of 4 intermediate layers. The prediction consists in training the LSTM

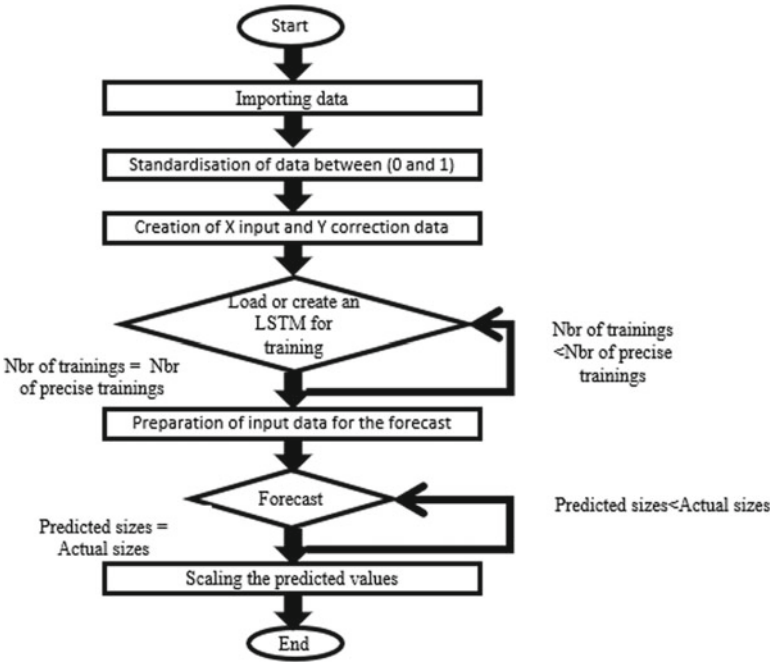

Fig. 4 Forecasting organigram

with 90% of the data and using the rest for testing. The results of these models are presented in Fig. 5. The green graph represents the real consumption, and the red graphs represent the predicted consumption.

- Model 1: for this model, each layer of neurons consists of 30 neurons.
- Model 2: for this model, each layer of neurons consists of 50 neurons.
- Model 3: for this model, each layer of neurons consists of 70 neurons.

We notice that all the predicted values are close to the real values since the training values are very large (90,000 values). Model 2 has the lowest root mean square error (RMSE) as shown in Fig. 6. This indicates that the architecture composed of 50 neurons per layer is the optimal one.

Comparison of Architectures with Fixed Number of Neurons per Layer. The architectures of these models have the same number of neurons per layer which will be 50 neurons. We have subsequently modified the number of layers, each model having its number of intermediate layers. From the graphs shown in Fig. 7, it can be seen that graph (d) is the closest to the actual case green graph.

Based on the RMSE values shown in Fig. 8, model 3 represents the lowest RMSE value. Therefore, the most optimal architecture has 4 intermediate layers and 50 neurons in each layer.

We have used this architecture in all the power consumption forecasts that are made hereafter.

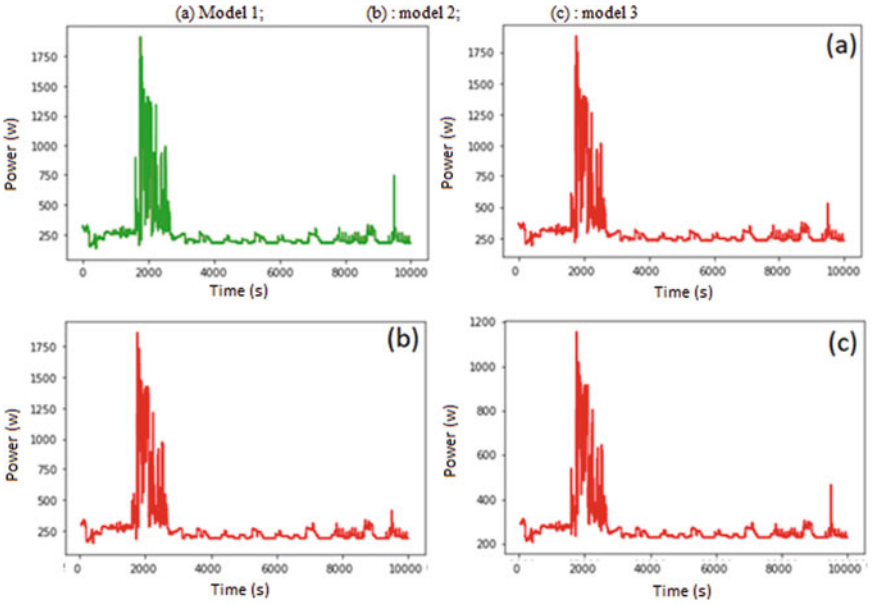

Fig. 5 Graphs of actual and predicted consumption

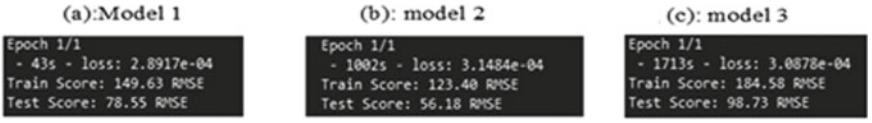

Fig. 6 The loss values and the square root of the error means

3.2 Pumping Station Consumption Forecasting

3 models were built for the power consumption forecast of this station:

- Model 1: Forecast based on consumption history
- Model 2: Forecast based on 3 variables (consumption history; days; seasons)
- Model 3: Forecast based on 5 variables (consumption history; days; seasons; average temperature; precipitation).

The models have been trained more than 1000 times before saving them so that we have a small loss value.

In order to allow this model to have a vision on the consumption during each day and each season since the consumption differs between days and seasons, and since the neural network only knows numbers, we coded the days from 1 to 7 (Monday: 1, Tuesday: 2, Wednesday: 3, Thursday: 4, Friday: 5, Saturday: 6, Sunday: 7) and the seasons from 1 to 4 (Winter: 1, Spring: 2, Summer: 3, Autumn: 4).

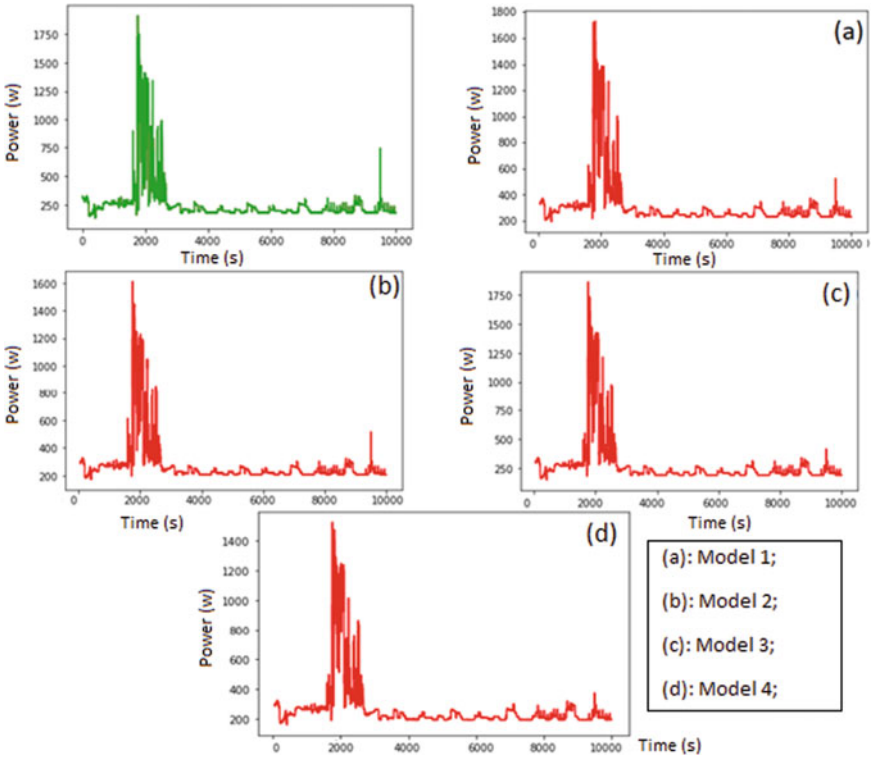

Fig. 7 Graphs of actual and predicted consumption

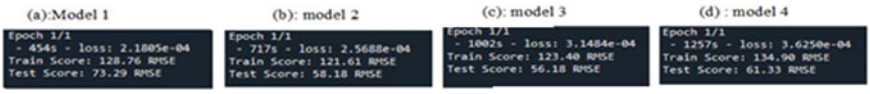

Fig. 8 The loss values and the RMSE for each model

The graphs of the actual and predicted consumption for pumping station are shown in Fig. 9.

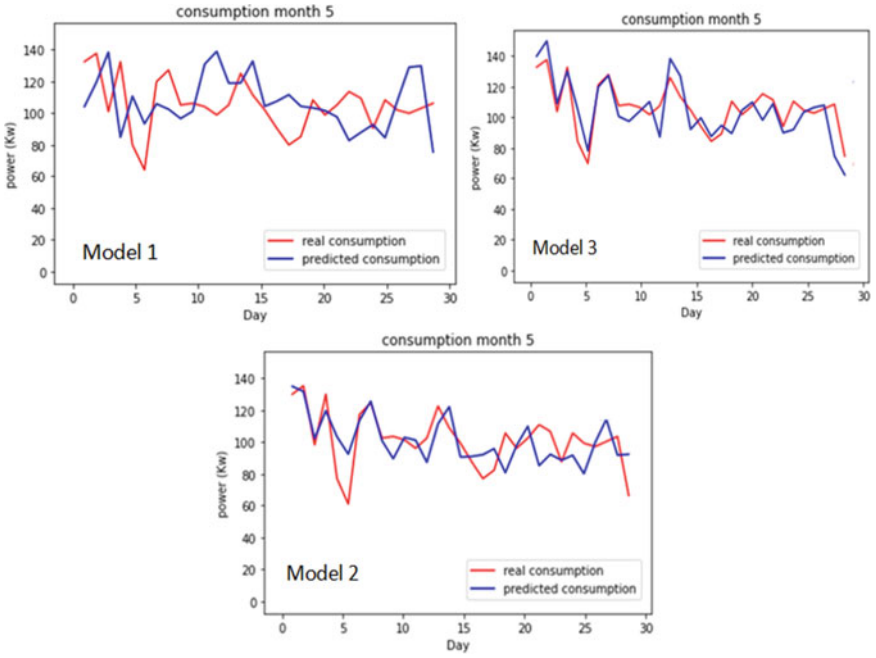

Fig. 9 Actual and forecasted consumption graphs for the pumping station

3.3 Forecast of the Consumption for Bni Bouayach Treatment Plant

Forecast of the total daily consumption of the treatment plant. In order to avoid exceeding the subscribed power, the forecast of the total daily consumption is necessary. We built 2 models (mono-variable and multi-variable) in order to choose the one which gives results close to the real case.

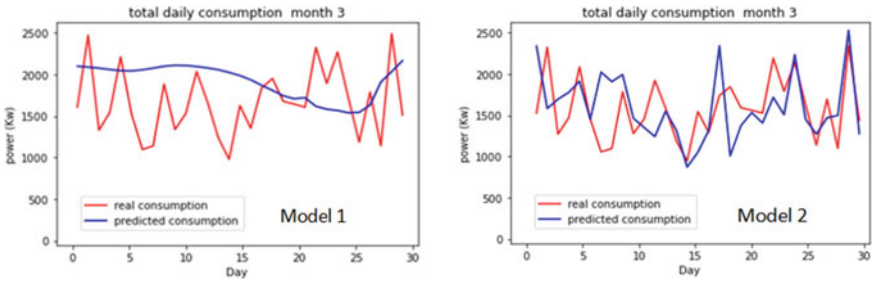

Fig. 10 Total daily consumption month 5

Figure 10 shows the forecast results of the daily consumption of the models that are built.

- Model 1: a single-variable model based only on the consumption history of the total daily consumed power.
- Model 2: a multi-variable model based on the consumption history of total consumption, days and seasons.

Forecast of Daily Consumption for each Hourly Periods. The forecast of the electricity consumption for each station is necessary in order to reduce the consumption fees. In fact, the price of electricity depends mainly on the time band for medium voltage customers (Price for peak hours 1.4157 dh, the price for daytime 1.0101 dh, and the price for off-peak hours 0.7398 dh). A good management of consumption schedules will therefore allow us to better control the electricity costs. Five models have been constructed with the intention of obtaining better results for each substation.

The first three models are mono-variable models based on the consumption history of each time band. The others are multivariate models based on: daytime energy, peak energy, night time energy, days, seasons and total energy.

- Model 1: three mono-variable models based on the consumption history of each time band.
- Model 2: a multi-variable model based on (night energy, day energy, peak energy).
- Model 3: a multi-variable model based on (night energy, day energy, peak energy, days, and seasons).
- Model 4: a multi-variable model based on (night energy, day energy, peak energy, days, seasons, total daily energy).

Predicted daytime electricity consumption. The electrical energy consumed during the day is called daytime energy. The graphs of the actual and predicted consumption are shown in Fig. 11.

Predicted off-peak electricity consumption. The night energy represents the electricity consumption during off-peak hours. Figure 12 shows the forecast results of the night energy.

Forecast of electricity consumption during peak hours. Many models are built for the purpose of forecasting electricity consumption during peak hours, also called peak energy. It is the most critical period for electricity distributors. Graphs obtained by these models are shown in Fig. 13.

4 Discussion

It is remarkable that the multi-variable models give results closer to the real ones than the mono-variable one, but it is necessary to take into consideration only the variables that have an important influence on the variable to be predicted, which in

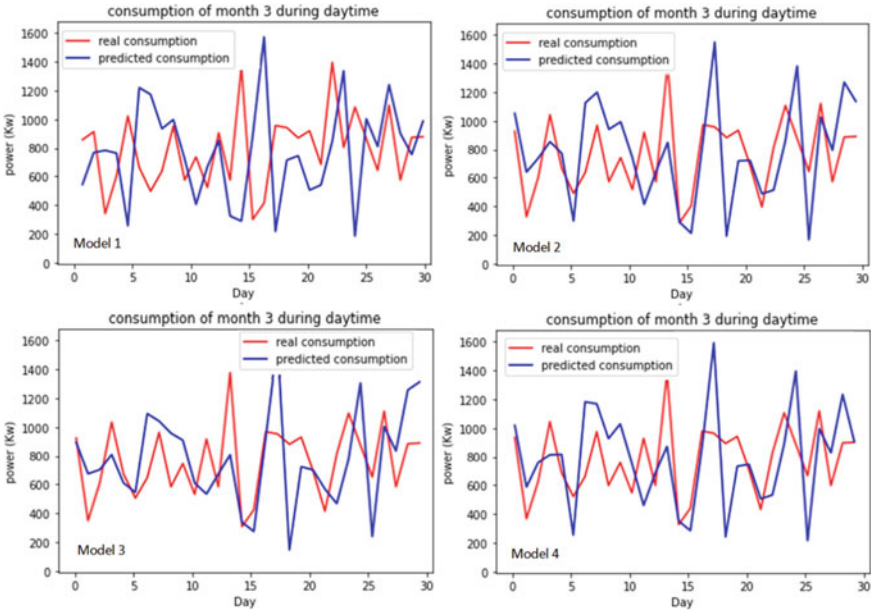

Fig. 11 Consumption of month 3 during peak *daytime*

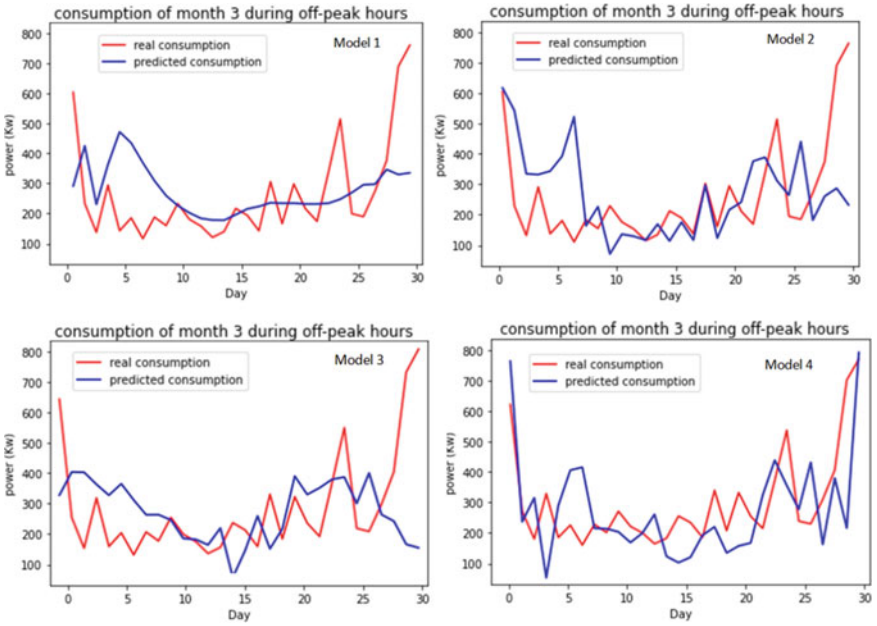

Fig. 12 Consumption *of* month 3 during off-peak hours

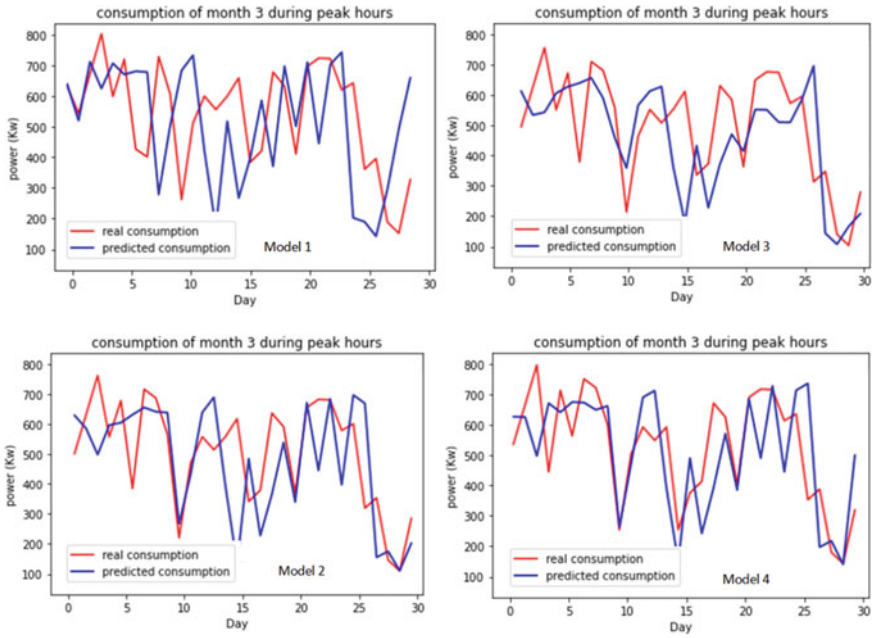

Fig. 13 Consumption *of* month 3 *during* peak *hours*

our case is the electric energy. The optimal model obtained for each electrical energy is discussed in the following.

4.1 Pumping Station Consumption Forecasting

The deviation indicators for the multivariate models are respectively: 178.30 for the model with 3 inputs (history, day and season) and 159.51 for the model based on 5 variables (history, day, season, temperature and precipitation).

It is remarkable that the indicators of the said models are close to each other, and this is due to the inputs sharing and the temperature and precipitation. These latter are taken from the geographical area and not from the site itself. Adding temperature and precipitation variables to the input of model 3, gives us improved results compared to other models, even if these data are not collected locally (Table 1).

Table 1 Comparison of total daily energy forecast models for the pumping station

	Model 1	Model 2	Model 3
Predicted variable	Daily power consumption	Daily power consumption	Daily power consumption
Number of variables	1	3	5
Types of input variables	Consumption history	Consumption history, days, seasons	Consumption history, days, seasons, average daily temperature and precipitation
Model types	Single-variable, multi-steps	Multi-variables, multi-steps	Multi-variables, multi-steps
Loss values	0.0068	0.0022	$4.0148e^{-4}$
Root mean square error	491.98	178.30	159.51

4.2 Forecast of the Consumption of the Bni Bouayach Treatment Plant

Total daily consumption forecast. It can be seen that the model based on historical total daily consumption, day and season was able to approximate the large variations in actual daily consumption with an RMSE = 481. It performed better than the single-variable model with an RMSE = 565.64. Its indicator for all models remains quite better. Given the known variation in this variable and the need for large data sets for its history or on-site meteorological data (Table 2).

Electricity consumption forecast for each hourly station. For the energy forecasting models for each hourly station, it is found that the 6-variable model gives night and peak energy forecasts closer to the real cases when compared to the other models, but it is noted that this is not the case for the daytime energy forecast. These results are close to reality using the 5-variable model (Table 3).

Table 2 Comparison between the total daily energy forecast models

	Model 1	Model 2
Predicted variable	Total daily energy	Total daily energy
Number of variables	1	3
Types of input variables	Total daily energy	Days, seasons, Total daily energy
Types of models	Single-variable, multi-step	Multi-variables, multi-step
Loss values	0.0025	$4.4258e^{-4}$
RMSE	565.644	481.014

Table 3 Comparison between the energy forecasting models of each hourly station

	Model 1	Model 2	Model 3	Model 4	Model 5	Model 6
Predicted variable	Night energy	Day energy	Peak energy	Night energy, Day energy, Peak energy	Night energy, Day energy, Peak energy	Night energy, Day energy, Peak energy
Nbr of variables	1	1	1	3	5	6
Types of input variables	Night energy	Day energy	Peak energy	Night energy, day energy, peak energy	Night energy, day energy, peak energy, days, seasons	Night energy, day energy, peak energy, days, seasons, total daily energy
Model types	Mono-variable	Mono-variable	Mono-variable	Multi-variables	Multi-variables	Multi-variables
Loss values	0.0017	$2.987e^{-4}$	$4.4848e^{-4}$	$5.323e^{-4}$	0.0019	$3.5397e^{-4}$
Root mean square error	191.97	521.052	252.386	Day = 388.78 Night = 209.43 Peak = 209.43	Day = 340.890 Night = 222.375 Peak = 174.79	Day = 388.088 Night = 183.232 Peak = 163.055

5 Conclusion

In order to control the evolution of electrical energy and to satisfy the needs of the future, taking into account the economic and environmental conditions, with the aim of achieving sustainable development, the forecasting of electrical consumption is obvious.

We focused on the medium-term forecasting of electricity consumption for a low voltage and medium voltage connection, using the neural network LSTM written with python using the Tensorflow environment and the KERAS library.

On the part of building an optimal model, we created and compared different architectures, changing the number of intermediate layers and the number of neurons per layer. Subsequently, we used the architecture that gives the smallest deviation indicator for the comparison between single and multi-variable models.

For low voltage branching, the multi-variable models are reliable compared to the single-variable model. The RMSE deviation indicator of the 5-variable model is close to that of the 3-variable model, because the weather data is taken from the geographical area and not locally.

For the medium voltage connections, it is found that the total daily energy, as well as the energy for each hourly substation, should be forecasted, the multi-variable models gave better results than the mono-variable models.

In conclusion, the forecasting results should be used to create management plans and energy limits that should not be exceeded by the operator. The improvement of the forecasting results goes hand in hand with the amount of data, such as the consumption history, not to mention the weather data which require the construction of a small weather station locally.

References

1. "Electricity consumption." https://www.iea.org/reports/electricity-information-overview/electricity-consumption
2. Ahmad, T., Chen, H., Shah, W.A.: Effective bulk energy consumption control and management for power utilities using artificial intelligence techniques under conventional and renewable energy resources. Int. J. Electr. Power Energy Syst. **109**, 242–258 (2019). https://doi.org/10.1016/j.ijepes.2019.02.023
3. "répartition de l'électricité vendue en 2019," 2019. http://www.one.org.ma/
4. Ahmad, T., Zhang, H., Yan, B.: A review on renewable energy and electricity requirement forecasting models for smart grid and buildings. Sustain. Cities Soc. **55**, 102052 (2020). https://doi.org/10.1016/j.scs.2020.102052
5. Hermiyanty, D.S.: Wandira Ayu Bertin, "MODÉLISATION ET PRÉVISION DE LA DEMANDE D'ÉLECTRICITÉ RÉSIDENTIELLE." J. Chem. Inf. Model. **8**(9), 1–58 (2017). https://doi.org/10.1017/CBO9781107415324.004
6. Wei, N., Li, C., Peng, X., Zeng, F., Lu, X.: Conventional models and artificial intelligence-based models for energy consumption forecasting: a review. J. Pet. Sci. Eng. **181**(March), 106187. https://doi.org/10.1016/j.petrol.2019.106187

7. Rathor, S.: Simple RNN vs GRU vs LSTM :- Difference lies in More Flexible control. https://medium.com/@saurabh.rathor092/simple-rnn-vs-gru-vs-lstm-difference-lies-in-more-flexible-control-5f33e07b1e57
8. Arbel, N.: How LSTM networks solve the problem of vanishing gradients, 2018. https://medium.datadriveninvestor.com/how-do-lstm-networks-solve-the-problem-of-vanishing-gradients-a6784971a577 (accessed Dec. 21, 1BC)
9. Wang, J.Q., Du, Y., Wang, J.: LSTM based long-term energy consumption prediction with periodicity. Energy, **197** (2020). https://doi.org/10.1016/j.energy.2020.117197
10. Goyena, R., Fallis, A.: "keras," J. Chem. Inf. Model. (2019) https://keras.io/about/
11. Karpathy, A. : Recurrent Neural Networks. http://karpathy.github.io/2015/05/21/rnn-effectiveness/
12. "Understanding-LSTMs." https://colah.github.io/posts/2015-08-Understanding-LSTMs/
13. "maisons intelligent," [Online]. Available: www.refitsmarthomes.org

Identification of Potatoes Harvested from the Treated Field with NPK Fertilizers with an Electronic System

Ali Amkor and Noureddine El Barbri

Abstract The multi-sensor systems are currently emerging as another cheaper and efficient alternative for measurement and quality control by evaluating volatile compounds in food. In this paper, an electronic system consisting of an array of commercial metal oxide gas sensors is used with machine learning algorithms to distinguish between potato samples grown from an untreated field and those grown from a field treated with Nitrogen, Phosphorus, and Potassium (NPK) fertilizer. The principal component analysis method (PCA) was appliqued on extracted features from the data generated by sensors for the different samples, and it turned out that about 98% of sample variance could be explained by the first two principal components (PC1 and PC2). The support vector machines (SVM) method was used to classify the data and it achieved the best performance with an accuracy of 92.5%. The experimental results attained confirm that a multi-sensor system coupled to the SVM can discriminate between potato products according to the nature of their cultivation field.

Keywords Metal oxide gas sensor · Multi-sensors system · Data analysis · Machine learning · Principal component analysis (PCA) · Support vector machines (SVM)

1 Introduction

After wheat, rice and maize, potatoes (*Solanum tuberosum* L.) are the fourth most important crop in the world and are cultivated in most climatic zones occupied by humans [1]. This vegetable product original from South America is widely consumed due to its nutritional value, it is very rich in its composition by starch which is a complex carbohydrate, crude protein, a variety of essential vitamins and minerals including vitamins C and B6, and the mineral potassium, magnesium, and iron, in addition to dietary fiber [2] …

A. Amkor (✉) · N. El Barbri
Laboratory of Science and Technology for the Engineer, LaSTI-ENSA, Sultan Moulay Slimane University, Khouribga, Morocco

M. Bendaoud et al. (eds.), *The Proceedings of the International Conference on Electrical Systems & Automation*, https://doi.org/10.1007/978-981-19-0039-6_3

The growing demand, as well as the large consumption of potatoes, push farmers to use biological or chemical fertilizers to improve soil yield and meet consumer expectations. In its growth, potatoes need large amounts of nutrients, especially N (nitrogen), P (phosphorus), and K (potassium) [3], and this justifies the use of these materials by farmers in fertilizing their soil. These fertilizers improve the agricultural product at the quantitative level, but unfortunately at the qualitative level, the potatoes undergo changes in their vegetative physiological properties [4–6]. Several studies conducted on potatoes have confirmed a large difference between organic potatoes and potatoes produced from soils treated with NPK fertilizer in their nutritional content. Organic potatoes which are healthier have a high content of protein and amino acids, vitamin C, and dry matter while low in nitrogen, nitrate, and reducing sugars. Without forgetting the impact of the fertilizer's excessive use on the environment, whether on their production level that leads to air pollution or on their user level that leads to the groundwater pollution [7].

On the other hand, potato tubercules have been the subject of several studies and analyses related to gases and volatile organic compounds (VOC) where we find the use of expensive and heavy equipment such as gas chromatography (GC), gas chromatography-mass spectrometry (GC-MS), these methods were used to determinate the pesticide residues presence in potato tuber [8], to analyze the potato tubers inoculated with *Phytophthora infestans* or *Fusarium coeruleum* [9], to identify volatiles generated by potato tubers infected by *Erwinia carotovora*, *Bacillus polymyxa* and Arthrobacter sp. [10], to monitor the change in concentration of pesticide residues in potatoes during washing and home preparation [11] … etc. Other chemical methods have also been used to study potatoes in their various states, where we find the use of near-infrared reflectance spectroscopy and chemometrics for discrimination of pure, powdered, purple sweet potatoes and their samples adulterated with the white sweet potato flour [12], the use of a solid-phase microextraction (SPME) fiber and gas chromatography with the flame ionization detector (GC-FID) to fingerprint volatiles to detect and discriminate diseases of potato tubers [13]. Another electronic alternative that has also been used for different studies of potatoes, it's the systems based on gas sensors: electronic nose or multisensory system, these easy-to-use electronic systems have a very low cost compared to the equipment already mentioned and are portable with the generation of the result in real-time were used to monitor potato soft rot infection in store [14], in the detection of potato brown rot and ring rot [15], in the detection of bacterial infection potato tuber soft rot disease [16], in the assessment of shelf-life of fried potato wedges [17], to early identification of potato storage disease [18].

This study aims to discriminate the potato produced from untreated soil from those produced from the treated soil with NPK fertilizer produced in our laboratory and used previously in the study of mint [19]. The signals of a sensor array composed of 5 sensors were studied using the first principal component analysis (PCA) method which is a statistical analysis to search for a possible difference between the samples, then a machine learning method such as support vector machines (SVM).

2 Material and Methods

2.1 Sample Preparation

In these experiments, potato tubers of the genus *Solanum tuberosum* L. were used because of their wide use around the world. Potatoes were taken from two types of soil, samples taken from untreated soil and samples from treated soil with NPK fertilizers. For the treated potato field, 4 fertilization applications were made, 30 days after planting, the first application was 0.2 tons of 20–20–20 per ha. The second, third, and fourth applications after successively 50, 70, and 90 days of planting were 0.5 tons each with a rate of 14–7–21 + 2MgO per ha.

The samples were carefully chosen, they were first inspected visually and the samples that showed signs of infections or green spots of chlorophyll were discriminated against.

The potatoes were previously washed and dried before being cut into fries a 100 g samples were placed in sealed (with a rubber stopper) labeled 1 L glass Erlenmeyer flasks and kept in a place at an ambient temperature of 25 ± 2 °C for one week (7 days) before being used in experiments.

2.2 Experimental Setup

In this study, a multi-sensor system was used. In general, multi-sensor instruments or electronic noses are instruments capable of mimicking the working principle of the human olfactory system. Wilkens and Hatman reported the first electronic noses in 1964, while the concept of an electronic nose as an intelligent system for classifying odors did not really emerge until 1982 through the work of Persaud and Dodd [20].

In our case, the measuring instrument was designed and constructed in a laboratory (Fig. 2), it was composed of a ventilator, a sample chamber which is the same chamber in which the sample to be studied was kept, a sensor chamber, a conversion and protection circuit, a data acquisition card, and a portable computer. Figure 1 represents schematically the measurement system produced.

The sensor chamber contains the sensor array, the latter was constructed with five commercially available metal oxide gas sensors listed in Table 1 purchased from two different companies: Figaro Engineering from Japan and MQ from China.

The sensitive element of the gas sensors used is a semiconductor of tin dioxide (SnO_2) where the presence of an oxidizing or reducing gas will cause modulation of the p–n junction, and this is mirrored directly on the signal of the heterojunction material sensor, which actually happens is the increase in conductivity during the presence of reducing gas or the decrease in conductivity during the presence of oxidizing gas thanks to exchanges of electrons inside a semiconductor [21].

Knowing that the maximum voltage that can be tolerated by analog inputs of the acquisition card is limited to 10 V and that these are protected by a big resistance, a

Fig. 1 Examples of the samples used

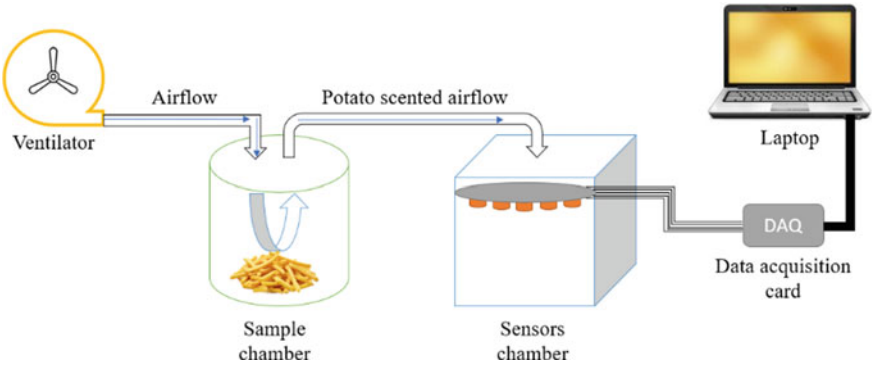

Fig. 2 Schematic representation of the measuring system

Table 1 A list of sensors used in this study

Sensor	Target gas
MQ 7	Carbon monoxide
MQ 136	Hydrogen sulfide, ammonia, air and carbon monoxide
TGS 821	Hydrogen
TGS 822	Vapors of organic solvents such as ethanol
TGS 2620	Volatile organic vapors

conversion and protection circuit is designed to protect the acquisition card against overvoltage and to prevent over voltages.

2.3 Experimental Measurement Protocol

Thanks to the ventilator, the mixture of air and emissions of each potato sample were introduced into the sensor chamber and with the help of the data acquisition card, the data collection was done.

Two series of experiments were carried out, twenty experiments per samples type to build solid information. A first series relating to potatoes harvested from the untreated field and a second series relating to those harvested from the field treated with NPK fertilizers. Data for each type of sample was taken for 8 min with a start injection of 30 s while giving the sensors an interval of 10 min to rest to allow them to return to their initial states at the end of each experiment.

2.4 Data Analysis

In the beginning, the data acquisition was done using the DAQ 1901 acquisition card and the LABVIEW software version 2017. As for the data analysis algorithms, they were performed using MATLAB software version 2019a. The responses signals from the sensors will undergo a pre-processing to extract the relevant properties from, then they will be normalized, now the data is ready for multivariate analysis. The method chosen for normalization is column normalization by dividing them by the maximum value:

$$X\mathrm{ij} = \frac{X\mathrm{ij}}{\mathrm{Max}(X\mathrm{i})} \tag{1}$$

Xij is the i-th sample of the j-th sensor, Xi contains all the p responses for the sensors of the i-th sample.

In the first stage, Principal Component Analysis (PCA) was exploited for statistical analysis of the data using a covariance matrix to construct the PCA plot.

In the second, for the evaluation of the model, the support vector machines (SVM) used with fivefold cross-validation.

3 Results and Discussion

3.1 Sensors Responses Analysis to Volatile Organic Compounds in Potato

Samples of healthy potato harvested from an untreated field and potato harvested from a field treated by NPK fertilizers were underwent an airflow to transport the headspaces to the sensor chamber. The sensor responses curves are shown in Fig. 3

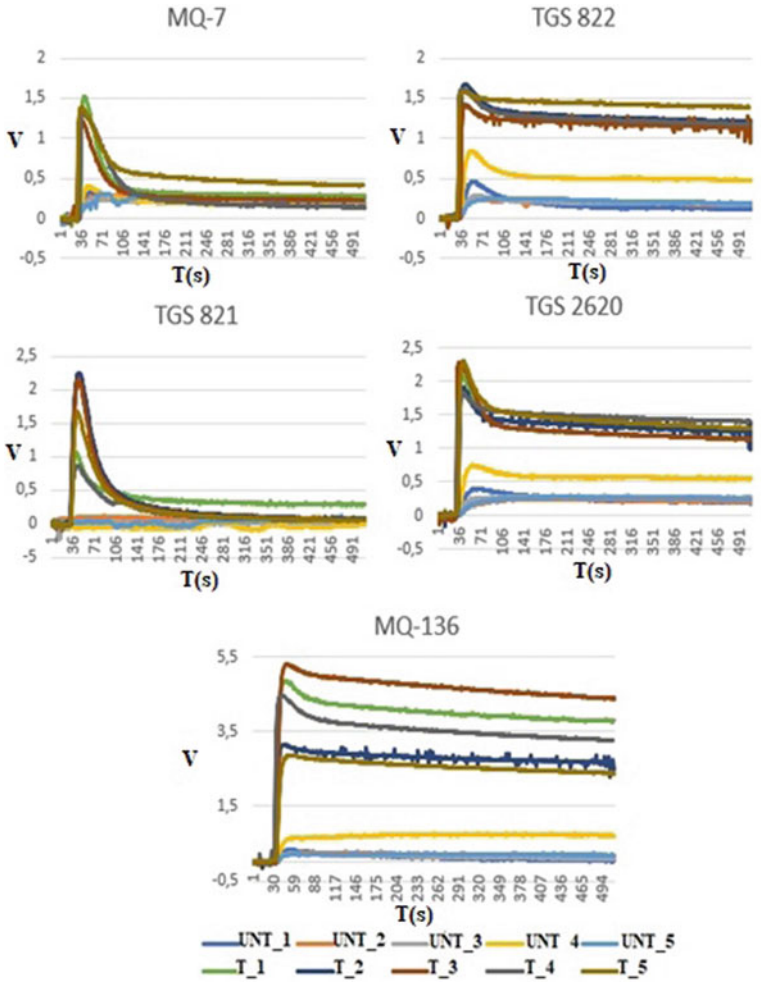

Fig. 3 Responses recorded from the five sensors to 5 potato samples taken from the untreated field (UNT_1, UNT_2, UNT_3, UNT_4, UNT_5) and to 5 other samples taken from the field treated by NPK fertilizer (T_1, T_2, T_3, T_4, T_5)

where we chose to project just five samples of each potato kinds. The horizontal axis shows the time in seconds, the vertical axis shows the value of the sensors output voltage in volts. It should be noted that to linearize the relationship between the voltage delivered by the sensors and the odor concentrations, the fractional difference method was used:

$$V_r = \frac{V_m - V_0}{V_0} \tag{2}$$

where V_r is the resulting relative voltage, V_m is the measured voltage and V_0 is the voltage at the starting point.

From Fig. 3, it can be seen initially that five sensors detect the presence of potato samples. The voltage of the sensors increases once the airflow enriched by the smell of potatoes is injected into the sensor chamber. What is remarkable, is the way the sensors respond to the origin of the samples, the sensors respond with a very high output voltage to samples of potatoes harvested from a treated field, on the contrary to those harvested from an untreated field. This difference indicates that the multisensory system can distinguish between samples based on their responses.

3.2 Features Extraction

In order to obtain an optimal recognition result, feature extraction from the original response curves of the sensor output is used, it consists in observing the curves to take a certain number of signal features for the robust identification of the potatoes according to their sources. In our case, 3 characteristics were extracted namely the maximum value, the air occupied by the signal, and the stabilized value enter 450 s and 500 s of the latter.

Therefore, our data matrix will be composed of 15 columns relating to 3 characteristics by every one of the five sensors and 40 rows relating to 40 experiments, 20 experiments by each sample type.

3.3 PCA Results

The principal component analysis (PCA) is a method usually utilized with the multisensor system [22], its goal is to diminish the dimension of multidimensional data to three or two dimensions (principal components). In the present case, this method is used to diminish our fifteen-dimensional data space to a two-dimensional (PC1, and PC2). The objective is to visualize the data in a graph without losing a lot of information and to build an idea on a possible distinction between samples. The result of the PCA method is shown in Fig. 4.

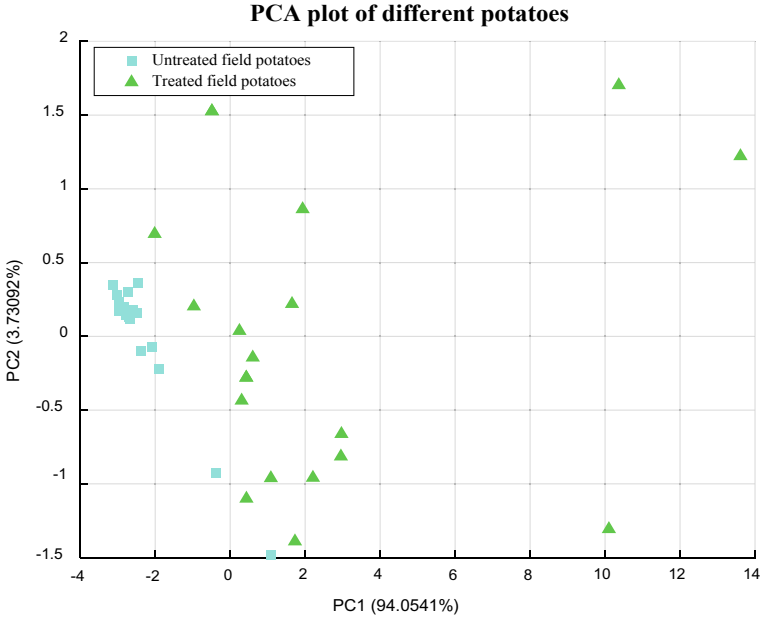

Fig. 4 The PCA scatter plot of potato samples according to their sources, untreated or treated with NPK fertilizers

The three-dimensional scatter plot shows that the samples point clouds of potatoes relating to the untreated field are well grouped and the distance between them and those relating to the treated field is relatively large and overlapped slightly at two points.

The cumulative contribution rate of the first two principal components was about 98%. The contribution rate of the first principal component (PC1) was 94.05% where the second principal component (PC2) contributed with 3.73%.

This encouraging result proves that it is possible to distinguish between potato samples according to their source (untreated or treated with NPK fertilizers), but the problem with the principal component analysis method lies in the lack of decision rule permitting the recognition of the unknown samples. Therefore, to solve this problem, the SVM method will be used to do the test and the prediction.

3.4 SVM Results

Support vector machines (SVM) is one of the most useful pattern recognition techniques [22], this supervised classification method, where training data sets are predetermined at the start, consists to predict the class of unknown samples. The main idea of SVM is based on the separation of classes with a particular hyperplane maximizing

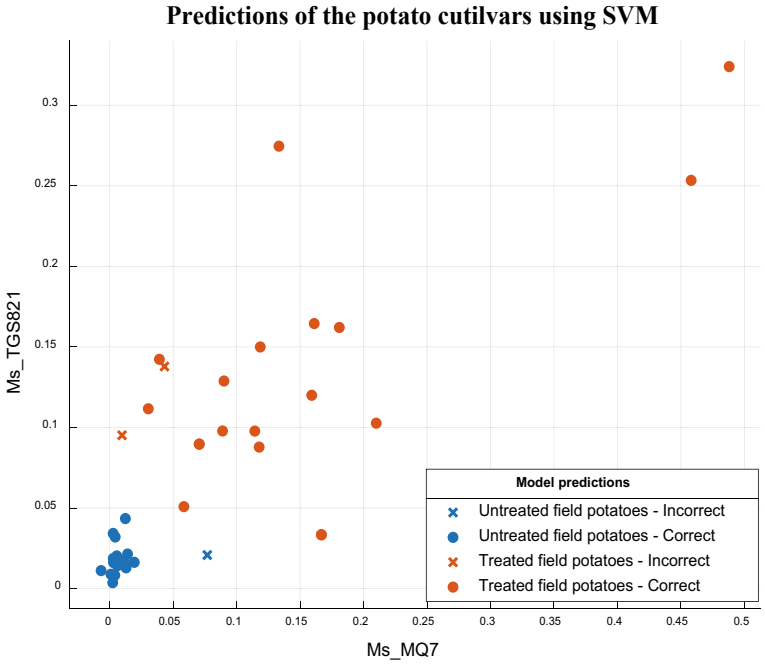

Fig. 5 The SVM classification result for potato samples according to their sources, untreated or treated with NPK fertilizers

the distance between classes of data named marge. In our case, the SVM classification was made using SVM classifier one-vs-one using a Gaussian kernel function with a five-fold cross-validation, 80% for learning and 20% for the test.

The result of the SVM method is shown in Fig. 5 where we have chosen the MQ7 sensor stabilized mean (Ms_MQ7) and that of the TGS821 sensor (Ms_TGS821) to visualize the results in a two-dimensional plane.

Viewing the result, a very good success rate was achieved of 92.5%, reflected in the correct assignment of the test samples to their data classes, except for two samples from the untreated group and one from the treated group.

This promising result, such as the one we performed in our first studies on mint using the same device [20, 23, 24], enhances the usefulness of our proposed approach that is simple and inexpensive, whether it is to distinguish insecticide-treated mints from untreated ones or to predict potato sources, does it come from an untreated field or from a field treated by NPK fertilizers.

4 Conclusion

In this study, an electronic system composed of a multi-sensor system coupled with a machine learning algorithm was applied as an alternative detection method to assess the origin of potatoes according to the nature of the soil. Potato samples were taken from an untreated field and other samples from a field treated with NPK fertilizers. The support vector machine (SVM) method was exploited to classify the data and it achieved the best performance with an accuracy of 92.5%. This work showed that the application of a multi-sensor system based on commercial metal oxide gas sensors with the support vector machine algorithm succeeded with a very encouraging success rate in distinguishing untreated potatoes from those treated with NPK fertilizers, which provides an alternative method to verify organic potatoes.

References

1. Zhang, H., Xu, F., Wu, Y., Hu, H., Dai, X.: Progress of potato staple food research and industry development in China. J. Integr. Agric. **16**(12), 2924–2932 (2017). https://doi.org/10.1016/s2095-3119(17)61736-2
2. Beals, K.A.: Potatoes, nutrition and health. Am. J. Potato Res. **96**(2), 102–110 (2018). https://doi.org/10.1007/s12230-018-09705-4
3. Bansal, S.K., Trehan, S.P.: Effect of potassium on yield and processing quality attributes of potato. Karnataka J. Agric. Sci. **24**(1), 48–54 (2011)
4. Abd El-Azeim, M.M., Sherif, M.A., Hussien, M.S., Tantawy, I.A.A., Bashandy, S.O.: Impacts of nano- and non-nanofertilizers on potato quality and productivity. Acta Ecol. Sin. (2020). https://doi.org/10.1016/j.chnaes.2019.12.007
5. Petropoulos, S.A., Fernandes, Â., Polyzos, N., Antoniadis, V., Barros, L., Ferreira, I.C.F.R.: The impact of fertilization regime on the crop performance and chemical composition of potato (*Solanum tuberosum* L.) cultivated in Central Greece. Agronomy **10**(4), 474 (2020). https://doi.org/10.3390/agronomy10040474
6. Mokrani, K., Hamdi, K., Tarchoun, N.: Potato (*Solanum tuberosum* L.) response to nitrogen, phosphorus and potassium fertilization rates. Commun. Soil Sci. Plant Anal. **49**(11), 1314–1330 (2018). https://doi.org/10.1080/00103624.2018.1457159
7. Savci, S.: Investigation of effect of chemical fertilizers on environment. APCBEE Procedia **1**, 287–292 (2012). https://doi.org/10.1016/j.apcbee.2012.03.047
8. Ahmed, M.A.I., Khalil, N.S., Abd El Rahman, T.A.: Determination of pesticide residues in potato tuber samples using QuEChERS extraction method with gas chromatography. Aust. J. Basic Appl. Sci. **8**(3), 349–353 (2014)
9. De Lacy Costello, B.P.J., Evans, P., Ewen, R.J., Gunson, H.E., Jones, P.R.H., Ratcliffe, N.M., Spencer-Phillips, P.T.N.: Gas chromatography-mass spectrometry analyses of volatile organic compounds from potato tubers inoculated with *Phytophthora infestans* or *Fusarium coeruleum*. Plant Pathol. **50**(4), 489–496 (2001). https://doi.org/10.1046/j.1365-3059.2001.00594.x
10. De Lacy Costello, B., Evans, P., Ewen, R., Gunson, H., Ratcliffe, N.M., Spencer-Phillips, P.T.: Identification of volatiles generated by potato tubers (*Solanum tuberosum* CV: Maris Piper) infected by *Erwinia carotovora*, *Bacillus polymyxa* and Arthrobacter sp. Plant. Pathol. **48**(3), 345–351 (1999)
11. Soliman, K.: Changes in concentration of pesticide residues in potatoes during washing and home preparation. Food Chem. Toxicol. **39**(8), 887–891 (2001). https://doi.org/10.1016/s0278-6915(00)00177-0

12. Ding, X., Ni, Y., Kokot, S.: NIR spectroscopy and chemometrics for the discrimination of pure, powdered, purple sweet potatoes and their samples adulterated with the white sweet potato flour. Chemometr. Intell. Lab. Syst. **144**, 17–23 (2015). https://doi.org/10.1016/j.chemolab.2015.03.004
13. Kushalappa, A.C., Lui, L.H., Chen, C.R., Lee, B.: Volatile fingerprinting (SPME-GC-FID) to detect and discriminate diseases of potato tubers. Plant Dis. **86**(2), 131–137 (2002). https://doi.org/10.1094/pdis.2002.86.2.131
14. Rutolo, M.F., Clarkson, J.P., Covington, J.A.: The use of an electronic nose to detect early signs of soft-rot infection in potatoes. Biosyst. Eng. **167**, 137–143 (2018). https://doi.org/10.1016/j.biosystemseng.2018.01.001
15. Biondi, E., Blasioli, S., Galeone, A., Spinelli, F., Cellini, A., Lucchese, C., Braschi, I.: Detection of potato brown rot and ring rot by electronic nose: from laboratory to real scale. Talanta **129**, 422–430 (2014). https://doi.org/10.1016/j.talanta.2014.04.057
16. Chang, Z., Lv, J., Qi, H., Ma, Y., Chen, D., Xie, J., Sun, Y.: Bacterial infection potato tuber soft rot disease detection based on electronic nose. Open Life Sci. **12**(1) (2017). https://doi.org/10.1515/biol-2017-0044
17. Chatterjee, D., Bhattacharjee, P., Bhattacharyya, N.: Development of methodology for assessment of shelf-life of fried potato wedges using electronic noses: sensor screening by fuzzy logic analysis. J. Food Eng. **133**, 23–29 (2014). https://doi.org/10.1016/j.jfoodeng.2014.02.009
18. Rutolo, M.F., Iliescu, D., Clarkson, J.P., Covington, J.A.: Early identification of potato storage disease using an array of metal-oxide based gas sensors. Postharvest Biol. Technol. **116**, 50–58 (2016). https://doi.org/10.1016/j.postharvbio.2015.12.028
19. Amkor, A., El Barbri, N.: A measurement prototype based on gas sensors for detection of pesticide residues in edible mint. J. Food Meas. Charact. (2020). https://doi.org/10.1007/s11694-020-00617-8
20. Gardner, J.W., Bartlett, P.N.: A brief history of electronic noses. Sens. Actuators B Chem. **18**(1–3), 210–211 (1994). https://doi.org/10.1016/0925-4005(94)87085-3
21. Nikolic, M.V., Milovanovic, V., Vasiljevic, Z.Z., Stamenkovic, Z.: Semiconductor gas sensors: materials, technology, design, and application. Sensors **20**(22), 6694 (2020). https://doi.org/10.3390/s20226694
22. El Barbri, N., Llobet, E., El Bari, N., Correig, X., Bouchikhi, B.: Electronic nose based on metal oxide semiconductor sensors as an alternative technique for the spoilage classification of red meat. Sensors **8**(1), 142–156 (2008). https://doi.org/10.3390/s8010142
23. Amkor, A., Maaider, K., El Barbri, N.: Mint treatment day prediction using a multi-sensors system and machine learning algorithms. Sens. Actuator A Phys. **328**, 112787 (2021). https://doi.org/10.1016/j.sna.2021.112787
24. Amkor, A., Barbri, N.E., Maaider, K.: A comparison between PLSR, SVMR and NARX network for the mint treatment day prediction based on multisensor system. In: 2021 7th International Conference on Optimization and Applications (ICOA) (2021). https://doi.org/10.1109/icoa51614.2021.9442652

Object Detection and Distance Estimation via Lidar and Camera Fusion for Autonomous Driving

Salma Ariche, Zakaria Boulghasoul, Abdelilah Haijoub, Abdelouahed Tajer, Hafid Griguer, and Abdelhafid El Ouardi

Abstract One of the most main perception challenges for autonomous vehicles is cars detection. Classic vision-based cars identification approaches are insufficiently accurate, particularly for small objects, whereas sensors such as Lidars help in detecting objects in all shapes and sizes but still limited in classifying and recognizing detected obstacles. To fully exploit the benefits of Lidar's depth information and vision's obstacle classification capabilities, this paper presents an object detection and distance estimation via Lidar and camera fusion. Both sensors have varied different characteristics and must be aligned by performing a geometrical transformation and projection to fuse the sensor's data. The main purpose of the conducted research is to fuse sensor data to estimate the distance of objects detected using Tiny YOLOv4. Finally, the results of the evaluations on the KITTI datasets show that the proposed approach enables both object detection and distance estimation.

Keywords Autonomous driving · Vehicle perception · Sensor fusion · Distance estimation · Object detection

1 Introduction

Improving the safety of road users has been a significant challenge for societies for many decades. Researchers and engineers are undertaking several efforts to propose innovative solutions for intelligent transportation systems, which will allow, through control and optimization strategies, to improve the traffic safety.

Interest in self-driving vehicles has grown in recent years because they provide comfort and safety for drivers by relying on three major technological components:

S. Ariche (✉) · Z. Boulghasoul · A. Tajer
System Engineering and Applications Laboratory, Cadi Ayyad University, Marrakech, Morocco
e-mail: salma.ariche@edu.uca.ma

A. Haijoub · H. Griguer
Innovation Laboratory for Operation, Mohammed VI Polytechnic University, Benguerir, Morocco

A. El Ouardi
SATIE, ENS, Paris-Saclay University, 91190 Gif-sur-Yvette, France

M. Bendaoud et al. (eds.), *The Proceedings of the International Conference on Electrical Systems & Automation*, https://doi.org/10.1007/978-981-19-0039-6_4

sensing and perception—a system that collects information and understands the surrounding environment—localization and mapping—allowing the vehicle to map its environment and locate itself at any given time—and finally, a control system—which is primarily responsible for decision making in various situations.

A key aspect of driving autonomous vehicles is the detection of obstacles and other cars through data fusion of several sensors. Cameras, light detection and ranging (LiDAR), and radar sensors are mainly developed for environment perception allowing an excellent geometric and semantic modeling of the vehicle's environment. Each sensor modality observes the environment in its way but is confined to detecting object attribute information.

LiDAR sensor readings, for example, can generate a three-dimensional frame of the surrounding environment. However, they are frequently impacted by severe weather conditions and are limited in their object classification capacity, whereas image sensing technologies are generally used for object detection and recognition but unreliable when it comes to estimating distance or velocity.

Although many research works outline a highly accurate object recognition system based on camera sensors only, there are still substantial challenges to overcome in the context of autonomous driving. Most research work has provided many approaches and algorithms for road object identification and recognition depending on the modality of each sensor, but only a few have addressed the issue of estimating the object distance [1, 2].

In this paper, we present a method for object detection with Tiny YOLOv4 and distance estimation relying on Lidar and camera data provided by the KITTI datasets.

The rest of this paper is structured as follows: Sect. 2 presents an overview of related work of object distance estimation; Sect. 3 describes our suggested approach for fusing data from a self-driving vehicle's camera and LiDAR. Section 4 presents evaluation results and discussions. Finally, in Sect. 5, a conclusion with some suggestions for further research and perspectives.

2 Related Work

Nowadays, sensors are essential devices that are embedded in vehicles, equipped with driver assistance technologies. For self-driving cars primarily, to observe their surroundings, numerous cameras, radar sensors, LiDAR sensors, and ultrasonic sensors are employed [3, 4]. As stated in [5] image processing is a critical component of vision sensing technology since it makes use of an automatic system to comprehend complicated environmental scenes. While a laser radar sensor is used to detect, track the target, a Lidar sensor can be classified based on function, line number, and laser emission waveform. Finally, conventional ultrasonic radars are classified into two types:

1. short-range ultrasonography, which helps detect impediments in the front and back.

2. long-distance ultrasonography, that measures the distance between the side barrier and the vehicle.

Autonomous driving researchers employ various sensor combinations to compensate the limits of each sensor as already indicated. Authors in [6] describe Sensor data fusion as the process of manipulating data and information from heterogeneous sensors to improve particular criteria and data elements for decision tasks. A normal camera's resolution, for example, is far greater than that of a detection and ranging sensor, but the camera has a restricted field of view and cannot give correct or precise distance and velocity information of detected objects in contrast to LiDAR, which is also limited by its inability to recognize color and classify items. Therefore sensor fusion approaches are unavoidably required for the safety and reliability of an autonomous vehicle. Authors in [6] list the 3 most used schemes of sensor fusion as illustrated in Fig. 1. Early fusion or raw data level, feature fusion (feature extraction then halfway fusion across the network), and finally decision fusion or late fusion which involves making final decisions. An overview of sensors and sensor fusion technologies in self-driving cars is provided by [5–7].

The fusion approach makes a correspondence between the 3D points from LiDAR and the RGB images of a camera. Authors in [8] reviewed environment perception algorithms for intelligent vehicles, with emphasis on lane and road, traffic sign detection, recognition, and scene comprehension. Multi-sensor approaches and a single fusion algorithm were conducted by [9, 10]. Paper [11] employed several fully convolutional neural networks and three different fusion techniques to detect roads using camera pictures and LiDAR point clouds. For advanced driver assistance systems (ADAS), authors in [12] propose a high-level sensor data fusion architecture. Reference [13] provides a hybrid multi-sensor fusion architecture that performs

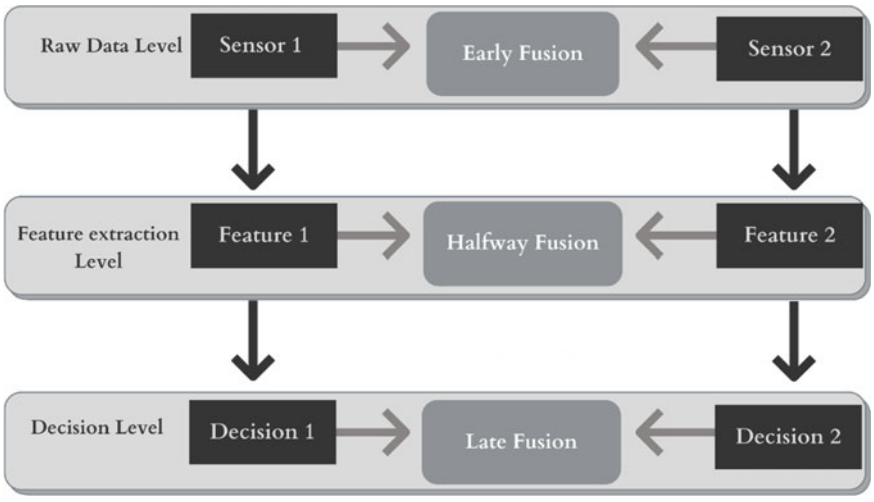

Fig. 1 Three known levels of sensor data fusion [5]

environment perception tasks such as road segmentation, obstacle identification, and tracking. In [14] a fusion method is presented based on fuzzy logic to calculate the object's distance by separately parsing image and point cloud data.

Lidar and camera fusion should be seen as an extrinsic calibration process to achieve low-level sensor fusion. This means that the geometrical properties of each sensor, such as its location and orientation, should be taken into consideration [15]. Usually, an external object is used like a trihedral rig [16], a circle [17], or a checkerboard pattern that serves as a target to align the characteristics of the two sensors [18, 19]. In [20], a black circular plane board is employed, to eliminate the checkerboard pattern's numerous inaccuracies. Automatic calibration methods also exist as described in reference [21]. Although many researchers have tried to conduct great calibration and data fusion work with high accuracy detecting objects forms, by putting sensors next to each other. Yet these methods are unsuitable for practical vehicle experiments where the vehicle has to detect recognize and estimate object distance in real-time. However, the authors in [1] make use of a 3D marker to fuse data of a Lidar and Camera with high precision and detect remote regardless of their position on the self-driving vehicle, with further work on distance estimation for object detection by data fusion on real road.

In this paper, we propose a method of fusing data from Lidar and camera to measure the distance of the detected object, relying on a robust and accurate detection algorithm like Tiny YOLOv4. Finally with the provided data from the KITTI datasets we evaluate our algorithm on real-life driving scenarios.

3 Sensor Fusion for Autonomous Driving

3.1 Perception Sensors

We focus on two key sensors in this paper: camera and LiDAR. As previously stated, both sensors have many limitations and shortcomings, combining the data provided by these two sensors with the appropriate fusion approach enhances detection robustness and performance.

- **Camera:** Equipping two lenses next to each other enables 3D vision, much like in humans. This sort of sensor may give 3D information at a cheap cost, in a small size, and with little power usage. Technologies (CCD, CMOS), resolutions (HD, etc.), and frame rates (up to 100 frames/s) are being continually developed. Furthermore, cameras enable the accurate extraction of geometric and photometric information, paving the way for higher level approaches of scene analysis and interpretation. Obstacle detection, parking assistance, road detection, traffic light and sign detection and identification are some examples.

  Before using camera information, an intrinsic and extrinsic calibration should be performed. Intrinsic parameters are concerned with the camera's intrinsic features (focal length, distortion, and picture center), they reflect a projective

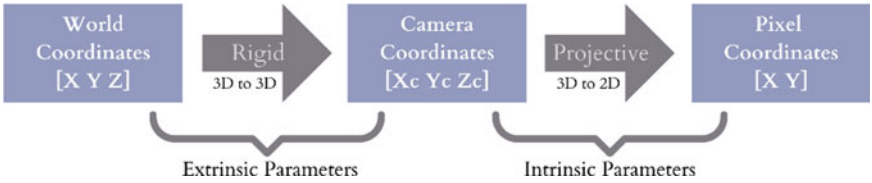

Fig. 2 Calibration with intrinsic and extrinsic parameters [22]

Table 1 Lidar parameters

Parameter	Value
Range length	40–100 m
Resolution accuracy	1.5–10 cm
Vertical angular resolution	0.35°–2°
Horizontal angular resolution	0.2°
Operating frequency	10–20 Hz

translation from the coordinates of the 3-D camera to the coordinates of the 2-D image. While extrinsic parameters refer to a rigid transformation from 3-D world coordinate system to the 3-D camera's coordinate system. Figure 2 highlights the calibration process.

- **Lidar:** Light (or Laser Imaging) Detection and Ranging is an abbreviation for the detection and measuring of distance by light. It is a time-of-flight (ToF) technology that analyzes the properties of an infrared laser (IR) returned by the target to its transmitter. Knowing the speed of light, the Lidar sensor can determine the distance to each object from the time between the laser pulse's emission and return pulse and provides angular resolution (horizontal and vertical). Every second, the Lidar sensor collects millions of accurate distance measurement points, which may be used to generate a 3D matrix of its surroundings. This detailed mapping can offer information on an object's position, shape, and behavior (Table 1).

3.2 The Proposed Sensor Fusion System Overview

This section describes the suggested raw sensor fusion approach for self-driving automobiles. The approach observes its surroundings by employing LiDAR and camera sensors to capture the many physical aspects of the environment (Fig. 3). Our main contributions in this paper are explained as follows:

(a) The first step of the process involves performing a calibration of both sensors using extrinsic and intrinsic matrices. Given the camera intrinsic matrices: only projection matrix if the camera images are rectified, otherwise matrices like S (1*2 size of the image before rectification), K-×× (3*3 calibration of the camera before rectification), and D-×× (1 × 5 distortion coefficients

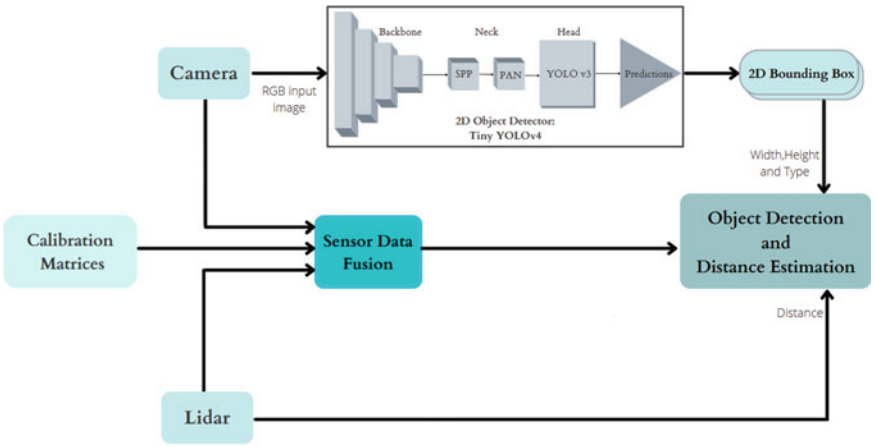

Fig. 3 Flow of the proposed method's process

of camera ×× before rectification) will be needed. Extrinsic parameters like rotation (R: 3 × 3), translation (T: 3 × 1) to convert Velodyne coordinates to camera coordinates. We can then project each 3D LiDAR point onto the camera image plane.

(b) A compressed version of YOLOv4 called Tiny YOLOv4 is utilized in our model to detect existing objects on RGB camera images that are provided as input. The detection algorithms consist of CSPDarknet53 as a backbone, spatial pyramid pooling additional module, PANet path-aggregation neck, and YOLOv3 head. In our study, we use tiny YOLOv4 for faster training and real-time object detection [23, 24].

(c) After calibrating both sensors and performing object detection, the LiDAR points are then projected onto the 2D bounding box. Each detected object is represented with bounding box coordinates (x, y, w, h) and 2D projected LiDAR points [Lidar]_2D(x, y, id), every Lidar point with 2D coordinates is presented as P_{2D}. Retrieved indices of 2D Lidar points that exist inside the 2D bounding Box, are calculated using Eq. (1):

$$\begin{aligned} &\text{Extracted id} \\ &= \left\{ \text{index}_i \in [\text{Lidar}]_{\_2D}(x, y, \text{id}), \right. \\ &\left. \text{if } P_{2D,i}[\text{Lidar}]_{\_2D}(x, y, \text{id}) \text{inside box}(x, y, w, h) \right\} \end{aligned} \tag{1}$$

(d) Finally, we measure the distance separating the self-driving vehicle and other obstacles relying on the fusion of two perception sensors: camera and LiDAR. We calculate the distance based on the minimum value of each 3D Lidar point which index corresponds to the extracted id calculated in the previous section.

Table 2 Tiny YOLOv4 parameters

Parameter	Value
Batch size	64
Learning rate	0.001
Channels	3
Number of epochs	100

4 Experimental Results and Discussion

4.1 KITTI Datasets and Processing

In this work, a dataset derived from KITTI driving sequences is utilized to verify the validity of our proposed fusion approach, highlighting the benefits of merging LIDAR data with camera pictures for object recognition and distance calculation [25].

For computer vision applications in an autonomous driving context such as perception and localization, the KITTI open-Source dataset provides a collected data by a 1.4 Megapixel color camera synced with a Velodyne Lidar HDL-64E from different scenarios that include eight categories of obstacles: vehicles, vans, trucks, standing and seated people, bicycles, trams, and others.

We generated the training and testing sets by relying on a random selection approach to divide all 7481 photos into the training and testing sets in a 7:3 ratio.

The experiments were carried out using an Intel (R) Core (TM) i7-4600U 2.7 GHz processor, NVIDIA-GPU Tesla K80 and 12G RAM. The size of input images is 416 $\times$ 416. Table 2 presents the training parameters of Tiny YOLOv4.

4.2 Results and Discussion

The KITTI supplied test set was used in the test section. Figures 4, 5 and 6 illustrate some of the evaluation's situations: 1-Object detection via Tiny YOLO v4 (Fig. 4a–c), 2-Lidar point cloud projection onto the 2D Bounding Boxes (Fig. 5a–c), 3-estimating the distance separating the self-driving vehicle and detected Objects (Fig. 6a–c). We chose three random scenarios containing obstacles such as vehicles, pedestrians, cyclists.

Based on the results observed in each figure, it is clear that using the Tiny YOLOv4 algorithm aided in the detection of obstacles surrounding the autonomous vehicle. However, due to the extreme occlusion, notably in scenes 4(a) and 4(b), the model was unable to recognize most of the existing obstacles. Because the Lidar points will only be projected onto the detected 2D bounding boxes, the model will only estimate the distance of identifiable objects within the visual field (Table 3).

Fig. 4 Results of vehicle detection using the Tiny YOLOv4 algorithm for 3 different scenarios **a**, **b** and **c**

As previously indicated, the model allows us to obtain distance information for only detected objects inside the 2D bounding box. Although the Deep Learning algorithm is much faster than YOLO's other versions, it still has many limitations. It is then necessary to upgrade to a higher version, such as Scaled YOLOv4, Embedded YOLOv4, or even YOLOv5, for better and more accurate results in object detection and recognition, resulting in a robust sensor fusion model capable of detecting, recognizing, and estimating distance for all existing obstacles in the surrounding environment.

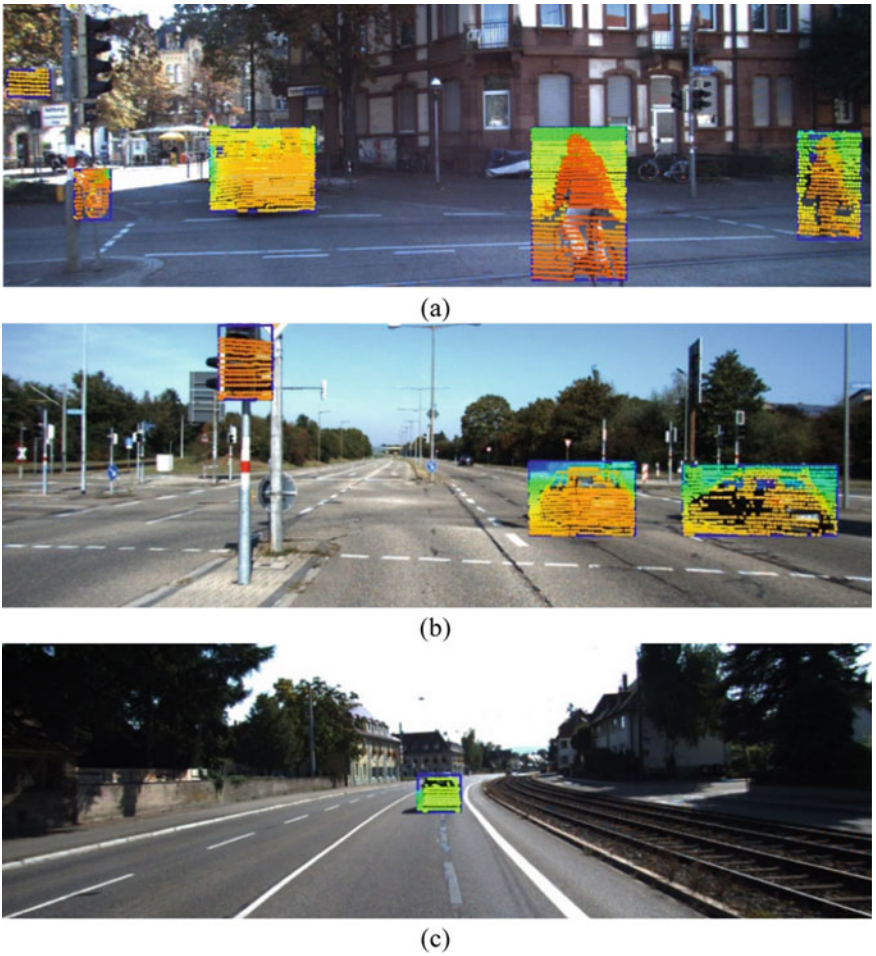

Fig. 5 Lidar points projection onto the 2D bounding box for 3 different scenarios **a**, **b** and **c**

5 Conclusions

This research work presents an object detection and distance estimation approach for self-driving vehicles. A low level real- time data fusion of 2 main perception sensors which are Lidar and Camera was conducted. First, we calibrate the LiDAR and camera sensors, relying on the extrinsic intrinsic characteristics to map the point cloud information onto the camera images. Next, Tiny YOLOv4 algorithm is implemented to detect objects and obstacles in the region of interest. Finally, we evaluate our proposed method by using different scenarios that are provided by KITTI datasets. However, the proposed algorithm has certain flaws that must be fixed. For example, Tiny YOLOv4 is unable to detect all the surrounding objects within a long or near

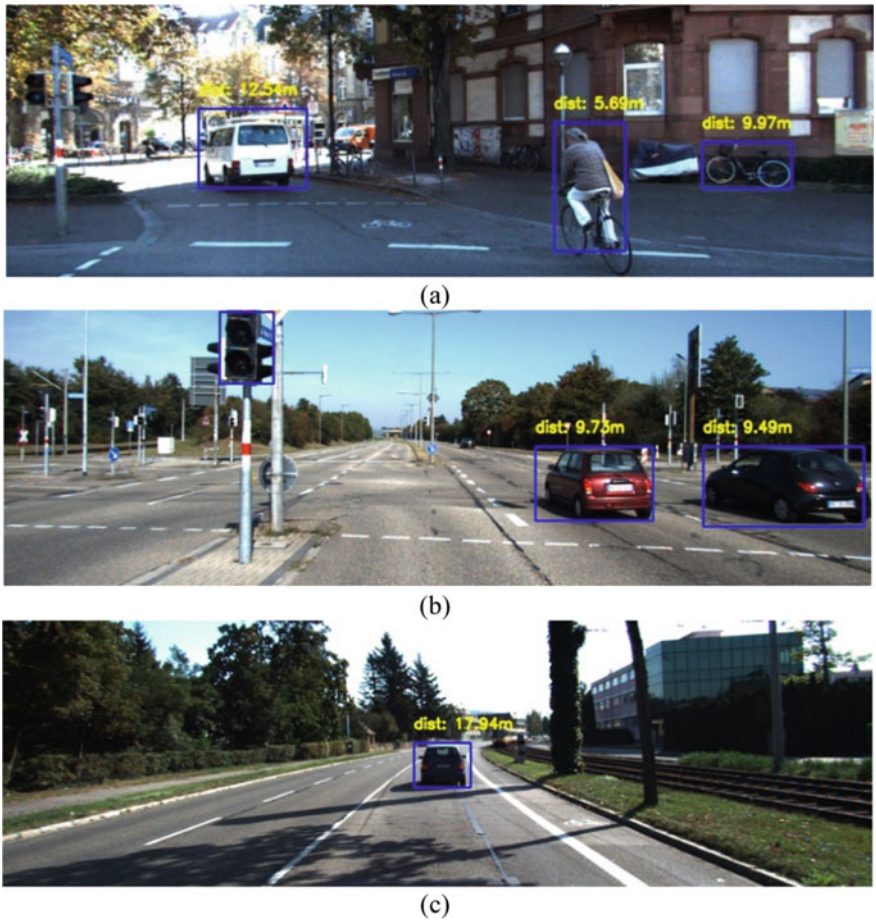

Fig. 6 Output of data fusion for distance estimation

Table 3 Results of Tiny YOLOv4

Scene	Vehicles (%)	Cyclists/pedestrians (%)	Traffic signs (%)
(a)	42	50	–
(b)	80	–	12.5
(c)	100	100	–

distance, thus the algorithm can only estimate the distance of fewer obstacles, which is still insufficient for practical tests.

In our future work, to enhance the robustness of our sensor fusion approach we will try to improve the YOLO algorithm or utilize more specialized Deep Learning models to obtain higher detection accuracy for real-time execution.

References

1. De Silva, V., Roche, J., Kondoz, A.: Fusion of Lidar and camera sensor data for environment sensing in driverless vehicles (2019)
2. Kumar, G.A., Lee, J.H., Hwang, J., et al.: LiDAR and camera fusion approach for object distance estimation in self-driving vehicles. Symmetry **12**, 324 (2020). https://doi.org/10.3390/sym12020324
3. Wang, Z., Wu, Y., Niu, Q.: Multi-sensor fusion in automated driving: a survey. IEEE Access **8**, 2847–2868 (2019). https://doi.org/10.1109/ACCESS.2962554
4. Yeong, D.J., Velasco-Hernandez, G., Barry, J., Walsh, J.: Sensor and sensor fusion technology in autonomous vehicles: a review. Sensors **21**, 2140 (2021). https://doi.org/10.3390/s21062140
5. Chen, Q., Xie, Y., Guo, S., Bai, J., Shu, Q.: Sensing system of environmental perception technologies for driverless vehicle: a review of state of the art and challenges. Sens. Actuators A Phys. **319**, 112566 (2021). https://doi.org/10.1016/j.sna.2021.112566
6. Fayyad, J., Jaradat, M.A., Gruyer, D., Najjaran, H.: Deep learning sensor fusion for autonomous vehicle perception and localization: a review. Sensors **20**, 4220 (2020). https://doi.org/10.3390/s20154220
7. Kocić, J., Jovičić, N., Drndarević, V.: Sensors and sensor fusion in autonomous vehicles. In: 2018 26th Telecommunications Forum (TELFOR), pp. 420–425 (2018). https://doi.org/10.1109/TELFOR.2018.8612054
8. Hu, H., Yuen, K.-V, Mihaylova, L. orcid.org/0000-0001-5856-2223 et al.: Overview of environment perception for intelligent vehicles. IEEE Trans. Intell. Transp. Syst. (2017). https://doi.org/10.1109/TITS.2017.2658662
9. Xiao, L., Dai, B., Liu, D., Hu, T., Wu, T.: CRF based road detection with multi-sensor fusion. In: IEEE Intelligent Vehicles Symposium (IV), pp. 192–198 (2015). https://doi.org/10.1109/IVS.2015.7225685
10. Xiao, L., Wang, R., Dai, B., Fang, Y., Liu, D., Wu, T.: Hybrid conditional random field-based camera-LIDAR fusion for road detection. Inform. Sci. **432**, 543–558 (2018). https://doi.org/10.1016/j.ins.2017.04.048
11. Caltagirone, L., Bellone, M., Svensson, L., Wahde, M.: LIDAR-camera fusion for road detection using fully convolutional neural networks. Rob. Auton. Syst. **111**, 125–131 (2019)
12. Aeberhard, M., Kaempchen, N.: High-level sensor data fusion architecture for vehicle surround environment perception. In: Proceedings of the 8th International Workshop on Intelligent Transportation (WIT 2011), Hamburg, Germany, pp. 22–23 (2011)
13. Shahian Jahromi, B., Tulabandhula, T., Cetin, S.: Real-time hybrid multi-sensor fusion framework for perception in autonomous vehicles. Sensors **19**, 4357 (2019). https://doi.org/10.3390/s19204357
14. Shi, J., Wang, W., Wang, X., Sun, H., Lan, X., Xin, J., Zheng, N.: Leveraging spatio-temporal evidence and independent vision channel to improve multi-sensor fusion for vehicle environmental perception. In: Proceedings of the IEEE Intelligent Vehicles Symposium (IV), Changshu, China, pp. 591–596 (2018)
15. Gong, X., Lin, Y., Liu, J.: Extrinsic calibration of a 3D LIDAR and a camera using a trihedron. Opt. Lasers Eng. **51**, 394–401 (2013). https://doi.org/10.1016/j.optlaseng.2012.11.015
16. Alismail, H., Baker, D.L., Browning, B.: Automatic calibration of a range sensor and camera system. In: Proceedings of the 3DiMPVT, Seattle, WA, USA, 29 June–1 July 2013
17. Alismail, H., Baker, D.L., Browning, B.: Automatic calibration of a range sensor and camera system. In: 3DIMPVT (2012)
18. Lipu, Z.: A new minimal solution for the extrinsic calibration of a 2D LIDAR and a camera using three plane-line correspondences. IEEE Sens. J. **14**(2), 442–454 (2014)
19. Lipu, Z., Deng, Z.: A new algorithm for the extrinsic calibration of a 2D LIDAR and a camera. Meas. Sci. Technol. **25**(6) (2014)
20. Zhang, Q., Pless, R.: Extrinsic calibration of a camera and laser range finder (improves camera calibration). In: 2004 IEEE/RSJ International Conference on Intelligent Robots and Systems (IROS), vol. 3, pp. 2301–2306 (2004)

21. Geiger, A., Moosmann, F., Car, Ö., Schuster, B.: Automatic camera and range sensor calibration using a single shot. In: IEEE International Conference on Robotics and Automation, pp. 3936–3943 (2012).https://doi.org/10.1109/ICRA.2012.6224570
22. Camera Calibration. https://www.mathworks.com/help/vision/ug/camera-calibration.html. Accessed on March 2021
23. Bochkovskiy, A., Wang, C.-Y., Mark Liao, H.-Y.: YOLOv4: optimal speed and accuracy of object detection (2020)
24. Wang, H., Lou, X., Cai, Y., Li Y., Chen, L.: Real-time vehicle detection algorithm based on vision and Lidar point cloud fusion. J. Sens. **2019** (2019). Article ID 8473980. https://doi.org/10.1155/2019/8473980
25. Geiger, A., Lenz, P., Stiller, C., Urtasun, R.: Vision meets robotics: the KITTI dataset. Int. J. Rob. Res. **32**(11), 1231–1237 (2013)

Toward a Prescriptive Analysis in Machine Learning: Use Case of Employability in Morocco

Mohamed Saouabi and Abdellah Ezzati

Abstract We live now in a time, where data is generated on a large scale and very fast. Analyzing this data in order to make decisions is necessary. Machine learning is capable to extract knowledge and valuable data from a large source of data and complex information without human intervention and fully driven by the data. Due to machine learning and data analytics, we can take advantage of this data to take pro-active decisions to improve organizations and solve problems. Researchers now are focusing their researches on just descriptive and predictive analysis. We propose in this paper a prescriptive analysis, it is considered as the next step after descriptive and predictive analysis, it is a technique using math programming models in order to optimize decision making and recommend specific decisions that should be considered to solve an existing problem. In this experiment, we are experimenting employability data using a decision tree model. And based on this model in the prescriptive analysis, we presented the best profile graduate who is the most likely to find a job.

Keywords Machine learning · Data analytics · Prescriptive analysis · Decision making · Employability

1 Introduction

Data now allows machine learning to take a holistic approach to data processing according to Madhavi Vaidya [1], the technology is now being advanced enough to access and analyze colossal amounts of information. Analytics is a very broad and evolving field that helps companies answer business questions about what occurred in the past, what will most likely occur in the future, and what decisions they can make to take advantage of these likely future developments. Reflecting the importance and growth of analytics, more and more universities are adding analytics degree programs, and many companies around the world are creating analytics departments.

M. Saouabi (✉) · A. Ezzati
Laboratory: LAVETE, Faculty of Science and Technology, Hassan First University of Settat, Settat, Morocco

M. Bendaoud et al. (eds.), *The Proceedings of the International Conference on Electrical Systems & Automation*, https://doi.org/10.1007/978-981-19-0039-6_5

Prescriptive analytics is the most sophisticated type of analytics and can bring valuable knowledge and helps optimize decisions according to Shubharthi Barua [2]. The objective is to suggest or prescribe the best case scenario, which means the best decision options, and take advantage of the predicted future using huge sources of data. In our experiment, we used a decision tree model on employability data. And based on this model in the prescriptive analysis, we presented the best profile graduate who is the most likely to find a job. We will first go over some prior research that is pertinent to this topic, and then we will go through the distinctions between descriptive predictive and prescriptive analytics.

2 Literature Review

Here presented below underneath some of the few works and tests utilizing prescriptive analysis.

Maya Sappelli [3] conducted a poll on predictive analytics. Prescriptive algorithms, they found, can provide actionable insights, but descriptive and predictive algorithms still require you to perform the thinking. They also concluded that while creating such algorithms is simple, monitoring them and keeping them free of biases is challenging. In some of those domains, privacy, ethics, and regulation are also essential considerations that should not be overlooked. Machines that write prescriptions aren't all that different from autonomous systems, thus they should be treated equally.

Jangwon Gim [4] presented a C-KAN cloud-based prescriptive assessment system based on a 5W1H approach. Internet of things sensor data stored in individual CKANs may be connected based on common ideas using the C-KAN cloud environment. As a consequence, it is possible to create a coordinate's information chart based on information interoperability, with the basic data serving as the foundation for prescriptive analysis. They also created a framework based on prescriptive analysis that can diagnose users' issues by studying user environment data and assisting users in making decisions by suggesting various actions based on the users' forthcoming scenarios.

Poornima [5] discussed the importance of predictive and prescriptive analytics for any type of application, which is incredibly advantageous for people to arrive at a conclusion at various phases, when they need to make the optimal option. They concluded that anyone with access to big data can do descriptive, predictive, and prescriptive analytics, which can assist enhance any sort of business application. This article delves into all aspects of predictive, descriptive, and prescriptive analytics, as well as its applications in a variety of fields.

João Lopes [6] proposed an experiment that aims to identify the advances that have been made in the area of healthcare, dedicated to the advancement of health-related prediction and optimization approaches, as well as how they may benefit management, doctors, and patients. They came to the conclusion that incorporating predictive analysis into a health organization may be highly beneficial in a variety

of areas, from the clinical support that may be provided in the discovery of how illnesses spread as well as in the anticipation of an occurrence so that the patient receives better and more accurate healthcare. The prescriptive analysis became a supplement to make predictive analysis, serving as the last line of defense for a larger intelligent system that is predictable enough to avoid failure in situations and offer the best course of action.

3 Material and Methods

In this experiment, we used RapidMiner Studio Educational Version 8.1.000 in Hadoop, it is used to implement machine learning algorithms, and it includes also Weka extension to implement algorithms designed for Weka mining tool. In our previous work done by Mohamed Saouabi and Abdellah Ezzati [7], we made a predictive analysis on employability data and based on this predictive analysis, we will optimize the decision taken by using a prescriptive analysis (Fig. 1).

We use predictive analytics—as presented in detail by Vaibhav Kumar [8] in order to have perspectives on the future and be capable of predicting what will happen. It uses previous data and tries to apply statistical techniques often using machine learning, and for the only objective to provide a vision into the future and avoid potential problems. On the other hand, prescriptive analysis, as presented by Katerina Lepenioti [9], can be considered like the next step of this process, so it is based on predictive analysis. The primary goal of this prescriptive analysis is to optimize the decisions we want to make by using math programming models. It is considered as the most valuable phase of the process, because it recommends the best case scenario of a situation and offers specific decisions. It reduces also the decision making risk; and gain time to focus on higher-value efforts such as performing scenario analysis or considering larger strategic questions.

Fig. 1 Predictive to prescriptive analysis

4 Results and Discussion

We present below the results of the predictive analysis using a decision tree, and then we will apply the prescriptive analysis.

4.1 Results

See Tables 1 and 2.

Table 1 Performance of the decision tree model

Metrics	Algorithm
	Decision tree
Accuracy	81.70
Precision	77.06
Classification error	18.30
Kappa statistics	0.631
F measure	0.84
Recall	92.92
Sensitivity	92.92
Time to build the model (ms)	390

Table 2 Confusion matrix of decision tree model

Confusion matrix	True working	True not working	Class precision
Pred. working	**409**	44	90.29%
Pred. not working	177	**578**	76.56%
Class recall (%)	69.80	92.93	

4.2 Model Developed by Decision Tree

```
University = ENCG: Working {Working=143, NotWorking=5}
University = ENSA
| | Grade = Good: Working {Working=2, NotWorking=1}
| | Grade = Passable: NotWorking {Working=0, NotWorking=8}
| Gender = Male: Working {Working=20, NotWorking=0}
University = ESTB
| EnglishLevel = High
| | TrainingPeriod = No: NotWorking {Working=0, NotWorking=11}
| | TrainingPeriod = Yes
| | | FrenchLevel = Low: NotWorking {Working=0, NotWorking=3}
| | | FrenchLevel = Medium: Working {Working=2, NotWorking=0}
| | | FrenchLevel = Vey Low
| | | | InformaticLevel = Very Good: Working {Working=13, NotWorking=1}
| | | | InformaticLevel = Medium: Working {Working=7, NotWorking=0}
| | | | InformaticLevel = Excellent: Working {Working=7, NotWorking=0}
| EnglishLevel = Excellent: Working {Working=5, NotWorking=0}
| EnglishLevel = Low: NotWorking {Working=0, NotWorking=3}
| EnglishLevel = Medium: Working {Working=3, NotWorking=0}
University = FPK: NotWorking {Working=100, NotWorking=212}
University = FSJES: Working {Working=161, NotWorking=105}
University = FST
| Grade = Pretty Good
| | Diploma = Diplôme d'ingénieur: Working {Working=10, NotWorking=0}
| | Diploma = Doctorat: Working {Working=2, NotWorking=0}
| | Diploma = Licence professionnelle: NotWorking {Working=5, NotWorking=13}
| | Diploma = Licence sciences et techniques
| | | FrenchLevel = Medium: Working {Working=10, NotWorking= 3}
| | | FrenchLevel = Low: NotWorking {Working=0, NotWorking=13}
| | | FrenchLevel = Excellent: Working {Working=6, NotWorking=0}
| | | FrenchLevel = Vey Low
| | | | EnglishLevel = High
| | | | | PracticeLevel = Low: NotWorking {Working=0, NotWorking=10}
| | | | | PracticeLevel = Very Good
| | | | | | Gender = Female: Working {Working=12, NotWorking=0}
| | | | | | Gender = Male: Working {Working=4, NotWorking=0}
| | | | | PracticeLevel = Medium
| | | | | | InformaticLevel = Medium: Working {Working=6, NotWorking=1}
| | | | | | InformaticLevel = Very Good: Working {Working=7, NotWorking=0}
| | | | | PracticeLevel = Excellent
| | | | | | BaccalaureateSerie = SVT: Working {Working=7, NotWorking=0}
| | | | | | | BaccalaureateSerie = Sciences et technologie électrique: Working
{Working=2, NotWorking=0}
| | | | EnglishLevel = Excellent
| | | | | Field = Gestion: NotWorking {Working=0, NotWorking=12}
| | | | | Field = Génie Electrique: Working {Working=4, NotWorking=0}
| | | | | Field = Génie Mécanique: NotWorking {Working=0, NotWorking=4}
| | | | | Field = Management Logistique et Transport: Working {Working=2,
NotWorking=0}
| | | | | Field = Protection de l'environnement: Working {Working=2, NotWork-
ing=0}
| | | | | Field = Techniques d'Analyse et Contrôle de Qualité: NotWorking
{Working=0, NotWorking=5}
| | | | EnglishLevel = Medium: Working {Working=10, NotWorking=1}
| | Diploma = Master recherche
| | | PracticeLevel = Very Good: Working {Working=14, NotWorking=7}
| | | PracticeLevel = Low: NotWorking {Working=0, NotWorking=12}
| | | PracticeLevel = Medium: Working {Working=11, NotWorking=6}
| | | PracticeLevel = Excellent: Working {Working=4, NotWorking=0}
| | Diploma = Master spécialisé: Working {Working=6, NotWorking=1}
| Grade = Good: Working {Working=43, NotWorking=24}
| Grade = Passable: NotWorking {Working=21, NotWorking=94}
| Grade = Excellent: Working {Working=2, NotWorking=0}
```

Descriptive Explains what happened

Diagnostic Explains why it happened

Predictive Forecasts what might happen

Prescriptive Recommends an action based on the forecast

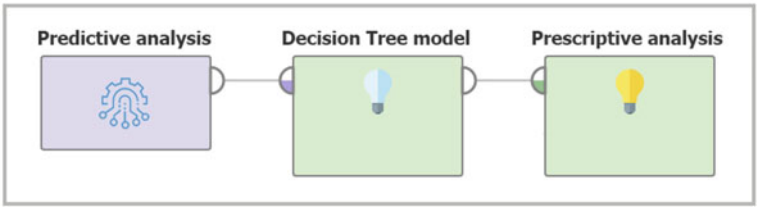

Fig. 2 Prescriptive analysis based on the decision tree model

4.3 Prescriptive Analysis Results

After applying the prescriptive analysis, we describe below the results of this experiment (Fig. 2).

In predictive modeling, we use a model to predict a result, based on an input. This operator reversed this procedure, obtaining by a model and the desired output, and prescribing an optimized input to achieve the desired result, above a figure describing the process of prescriptive analysis. This process results in a model of decision Tree on employability data. We used Prescriptive Analytics to find the optimal attribute values that optimize the chances of finding a job.

4.4 Prescriptive Analysis Parameters

4.4.1 Classification

This parameter indicates if the model is a classification model or a regression model.

4.4.2 Class Name

Indicates the class for which the confidence should be optimized.

4.4.3 Optimization Direction

Minimize, maximize, or specify a value as the optimization approach. For regression and forecasting issues, a particular value might be beneficial.

4.4.4 Value to Reach

Set a confidence or regression value that needs to be met. Only if "optimization direction" is set to "particular value" is this option accessible.

4.4.5 Stay Around Average (Numerical)

This option specifies whether numerical values should remain within a defined range around the average value, preventing extreme numbers from being used as inputs.

4.4.6 Standard Deviations Around Average

The number of SVs that values can deviate from the numerical average is defined here.

4.4.7 Stay Above Global Minimum (Numerical)

This option specifies whether numerical values shall remain above the associated attribute's minimum value.

4.4.8 Stay Below Global Maximum (Numerical)

This option specifies whether numerical values should be kept below the attribute's maximum value.

4.4.9 Stay Above Value (Numerical)

This option specifies whether numerical values shall remain over a certain threshold.

4.4.10 Minimum Value

During optimization, attribute values should remain above this value.

4.4.11 Stay Below Value (Numerical)

This option specifies whether numerical values shall remain below a certain threshold.

4.4.12 Maximum Value

Attribute values during optimization should stay below this value.

4.4.13 Constant Attribute Values

Represent a set of characteristics that should all have the same value. We can use the attribute name on the left and the required constant value on the right to construct the value of the name to define when the optimization ends for the constraint type.

4.4.14 Limit Type

Defines when the optimization ends. To find the best solution, No-Limit employs a heuristic. After the stated amount of time has passed, the time restriction will end. When the required number of generations is reached, the generation process is stopped.

4.4.15 Maximum Generations

Represent the evolutionary optimization algorithm's maximum generations number. Only if the limit is "generations and population size" is it available.

4.4.16 Population Size

Represent the number of people in the evolutionary optimization algorithm's population. Only if the limit is "generations and population size" is it available.

Table 3 Results of the prescriptive analysis

Results: best profile	
Prediction	Working
Confidence (working)	1
Computer science knowledge	Medium
Diploma	Diploma of engineering
Institution	ENSA
Faculty	Mathematics applications
Bac grade	Very good
English level	Medium
French level	Excellent
Practice competences	Good
Bac serie	Mathematic sciences
Gender	Man
Training period	Yes
Theoretical competences	Medium

4.4.17 Time Limit (in Seconds)

The maximum amount of time the optimization will take to complete. Only available if the limit is "time limit" (Table 3).

Based on the model, we applied an evolutionary optimization approach. We have the choice to use one of the following targets:

- Minimize a class's trust;
- Maximize the confidence of a class;
- Get closer to the confidence of a selected class;
- Minimize the regression prediction;
- Maximize the regression prediction;
- Get as close as possible to a specific regression prediction.

We have maximized the confidence of the "Working" class, in order to be able to find the optimal values based on the model of decision tree developed. We used the operator Prescriptive Analytics to find the optimal attribute values that optimize the chances of finding a job. Default parameter values will provide reasonable results without going to extremes. But we have made important adjustments. We defined that it was a classification problem and that we wanted to maximize the prediction of "Yes", which corresponds to "Working", which means that we will look for the best performing profile that has the most chance to find a job.

5 Conclusion

Valuable information and knowledge are hidden in databases today. Due to the increasing use of technologies and smart devices, data is generated almost all the time, but this data needs to be managed and analyzed in order to take valuable information from it. Machine learning extracts useful information from it with the use of complex algorithms. It's about using data analysis tools to uncover new, unknown knowledge, hidden relationships between large datasets, these hidden models can be used to predict future behavior. These tools can handle mathematical algorithms and statistical models. In this paper, we proposed a prescriptive analysis. The objective is to suggest or prescribe the best case scenario, which means the best decision options, and take advantage of the predicted future using huge sources of data. We used a prescriptive analysis process based on a decision tree model applied to employability data. We then used the operator Prescriptive Analytics to find the optimal attribute values that optimize the chances of finding a job.

References

1. Gim, J., Lee, S.: A study of prescriptive analysis framework for human care services based on CKAN cloud. Hindawi J. Sens. 1–10 (2018)
2. Lopes, J., Guimarães, T.: Predictive and prescriptive analytics in healthcare: a survey. Procedia Comput. Sci. 1029–1034 (2019)
3. Lepenioti, K., Bousdekis, A.: Prescriptive analytics: literature review and research challenges. Int. J. Inf. Manage. **50**, 57–70 (2020)
4. Vaidya, M., Deshpande, S.: Design and analysis of large data processing techniques. Int. J. Comput. Appl. **100**(8), 24–28 (2014)
5. Sappelli, M., Smit, S.K.: A vision on prescriptive analytics. In: ALLDATA 2017: The Third International Conference on Big Data, Small Data, Linked Data and Open Data, pp. 45–50 (2017)
6. Mohamed, S., Abdellah, E.: Prediction model for employability in Morocco using data mining techniques. J. Eng. Appl. Sci. **14**(5), 1690–1694 (2019)
7. Poornima, S., Pushpalatha, M.: A journey from big data towards prescriptive analytics. ARPN J. Eng. Appl. Sci. **11**(19), 11465–11474 (2016)
8. Barua, S., Gao, X.: Comparison of prescriptive and performance-based regulatory regimes in the U.S.A and the U.K. J. Loss Prev. Process Ind. 764–769 (2016)
9. Vaibhav Kumar, M.L.: Predictive analytics: a review of trends and techniques. Int. J. Comput. Appl. **182**(1), 31–37 (2018)
10. Prescriptive analytics system for improving research power.In: IEEE 16th International Conference on Computational Science and Engineering (CSE), pp. 1144–1145 (2013)
11. Ting, K.M.: Confusion matrix. In: Sammut, C., Webb, G.I. (eds.) Encyclopedia of Machine Learning and Data Mining. Springer (2017)
12. Yao, J.T.: Sensitivity analysis for data mining. In: IEEE EXPLORE Fuzzy Information Processing Society, 2003. NAFIPS 2003. 22nd International Conference of the North American, pp. 1–6 (2013)
13. Jain, J., Pal, P.R.: Detecting worms based on data mining classification technique. Int. J. Eng. Sci. Comput. **7**(5), 11388–11391 (2017)

14. Zhang, S., Tjortjis, C., Zeng, X., Qiao, H., Buchan, I., Keane, J.: Comparing data mining methods with logistic regression in childhood obesity prediction. Inf. Syst. Front. **11**(4), 449–460 (2009)
15. Shadroo, S., Rahmani, A.M.: Systematic survey of big data and data mining in internet of things. Comput. Netw. **139**, 19–47 (2018)
16. Drigas, A.S., Leliopoulos, P.: The use of big data in education. IJCSI Int. J. Comput. Sci. **11**(5), 58–63 (2014)
17. Vidgen, R., Shaw, S., Grant, D.B.: Management challenges in creating value from business analytics. Euro. J. Oper. Res. 626–639 (2017)
18. Ayhan, S., Costas, P., Samet, H.: Prescriptive analytics system for long-range aircraft conflict detection and resolution. In: Proceedings of the 26th ACM SIGSPATIAL International Conference on Advances in Geographic Information Systems, pp. 239–248 (2018)
19. Gröger, C., Schwarz, H., Mitschang, B.: Prescriptive analytics for recommendation-based business process optimization. In: International Conference on Business Information Systems, pp. 25–37 (2014)
20. Šikšnys, L., Pedersen, T.B.: Prescriptive analytics. In: Liu, L., Özsu, M. (eds.) Encyclopedia of Database Systems. Springer, New York (2016)
21. Srinivas, S., Ravindran, A.R.: Optimizing outpatient appointment system using machine learning algorithms and scheduling rules: a prescriptive analytics framework. 245–261 (2018)
22. Hu, Q., et al.: A review of data analytic applications in road traffic safety. Part 2: prescriptive modeling. **20**(4) (2020)
23. Saybania, M.R., Wah, T.Y.: Data mining and data gathering in a refinery

Modelling "Cognitive Households Digital Twins" in an Energy Community

Kankam O. Adu-Kankam and Luis M. Camarinha-Matos

Abstract Available literature suggests that households consume a considerable amount of energy in contemporary societies. Many techniques expected to help reduce the impact of households' energy consumption have been suggested in several studies. Cognitive Household Digital Twins (CHDT) is one of such ideas perceived to facilitate rational decision-making regarding energy consumption. A CHDT could be described as a digital replica/model of a household within the cyber-physical space. Such digital twins could possess some attributes such as cognitive capabilities, enabling them to make decisions based on some level of delegated authority from their physical twin. The outcomes of their decisions are expected to increase the sustainable energy consumption of the physical twin. In this study, we demonstrate how CHDTs can exhibit such cognitive and decision-making capabilities using software simulation. In our approach, we modelled a community of CHDTs who collaborate to jointly execute a common task, in this case, jointly minimize consumption, hoping to maximize the opportunity to sell energy to the grid. We adopted a multi-method simulation technique that involves multiple simulation paradigms integrated onto a single simulation platform. The adopted paradigms include System Dynamics, Agent-Based, and Discrete Event simulation techniques. The study's outcome suggests that CHDTs can be a valuable form of autonomous entity that can assist as complimentary decision-making agents in households.

Keywords Collaborative networks · Digital twins · Cognitive agents · Sustainable consumption · Decision-making

K. O. Adu-Kankam (✉) · L. M. Camarinha-Matos
School of Science and Technology and UNINOVA—CTS, Nova University of Lisbon, Campus de Caparica, 2829-516 Monte de Caparica, Portugal

L. M. Camarinha-Matos
e-mail: cam@uninova.pt

K. O. Adu-Kankam
School of Engineering, University of Energy and Natural Resources (UENR), 214, Sunyani, Ghana

M. Bendaoud et al. (eds.), *The Proceedings of the International Conference on Electrical Systems & Automation*, https://doi.org/10.1007/978-981-19-0039-6_6

1 Introduction

Reports from the European Commission suggests that buildings are responsible for approximately 40% of the EU's energy consumption and 36% of CO_2 emissions in Europe [1]. Consequently, buildings have been declared the single largest energy consumer in Europe. Globally, households are claimed to contribute nearly 72% of greenhouse gas (GHG) emissions [2]. These empirical data unveil the significant role households play towards the global emission of GHGs. Albeit this also suggests the potential contribution that households could make towards the mitigation of the problem.

Advancements in internet-based technologies, as well as emerging concepts and tools in machine learning, artificial intelligence, IoT, 3D visualisation, immersive environments, and big data analytics, are having a profound effect on the way the physical and cyber worlds interact. The effect of this complex synergy is a gradual convergence of the cyber and physical worlds in such a way that entities in the physical realms could have their replica in the cyber space, resulting in the notion of a "Digital Twin" (DT). A DT, according to [3], is a digital replica of a physical object or system. However, the application of DT concepts today is more extensive. It is applied in areas such as process management, behaviour modelling, system optimization, etc., and across a wide range of disciplines too.

In a previous study [4] the concept of Cognitive Household Digital Twin (CHDT) was proposed, where the authors envisioned that DT concepts could have a useful application in the domain of energy. It was claimed that CHDTs could be designed to possess some cognitive and autonomous attributes that could enable them to play complementary roles as decision-making agents in households. The authors further described a CHDT as a digital replica/model of a physical household that is equipped with some level of intelligence, so that it can receive some input from its Physical Twin (PT) and based on that input, make some basic energy use decisions on behalf of the PT. The input from the PT shall be referred to as "delegated authority".

In this study, we aimed at adopting software simulation to model the cognitive (intelligent) capabilities of these proposed CHDTs. The study was guided by the following research questions:

RQ-1. How can the cognitive capabilities of CHDTs be modelled?

RQ-2. How can CHDTs utilize these cognitive capabilities to make decisions that facilitate collaborations?

2 Related Works and Theoretical Framework

The Collaborative Virtual Power Plant Ecosystem is a concept that was derived from the merger of principles and concepts from the disciplines of Collaborative Networks (CNs) and Virtual Power Plants (VPP). Central to these concepts is the notion of collaboration, which happens to be fundamental to the discipline of CNs

[5, 6]. A VPP on the other hand is a virtual entity involving multiple stakeholders and comprising decentralized multi-site heterogeneous technologies, formed by aggregating deferrable and non-deferrable distributed energy sources [7]. The mix of these two concepts led to a hybrid concept called the Collaborative Virtual Power Plant Ecosystem (CVPP-E) introduced in [7] and [8]. A CVPP-E can be a replica of a renewable energy community such as described in [9]. The CVPP-E could also be described as a form of business ecosystem and a community of practice where members approach energy generation, consumption, and conservation from a collaborative point of view. The governing structure is polycentric and decentralized with a manager who plays a coordinating role and promotes collaborative behaviours.

Similar works found in the literature include [10], where the authors created a digital twin that accurately reflects the behaviour and characteristics of buildings. The building was reproduced using Autodesk REVIT. Another study discussed in [11] proposed the connection of a digital building twin with blockchain-based smart contracts to execute performance-based digital payments. Finally, a review presented with empirical evidence validated DT technologies as novel ways of implementing consumer-oriented demand-side management. The authors further identified some barriers that are associated with the adoption of energy services, particularly as they relate to the implementation and overall adoption of the digital-twins concept.

3 Modelling Framework

To help replicate the attributes or preferences of the PT in its equivalent DT, we adopted a multi-method simulation technique which enabled the integration of simulation paradigms such as System Dynamics, Agent-Based, and Discrete Event simulation methods as supported by the Analogic platform [12]. Using this approach, each CHDT was modelled as a software agent. All relevant attributes of the PT were modelled inside the CHDT as a logical sequence of internal states using state charts. State charts are one of the UML languages that are often used to model the dynamic behaviour of a system in response to time and changing external stimuli [13]. The various aspects of the prototype model are discussed below.

3.1 Modelling Households as CHDTs

The replica of all the PTs is modelled as autonomous software agents, referred to as CHDTs. In terms of behaviour and preferences, a CHDT is similar to its PT counterpart. Each PT is characterized by a unique set of attributes such as types and quantity of appliances, energy use preferences, the capacity of installed Photovoltaic (PV) systems, etc. In a similar manner, a CHDT is modelled to mimic its corresponding PT by replicating these unique attributes in them.

3.2 Modelling Appliances and Their Use-Behaviours

Each CHDT is modelled to possess some embedded household appliances which are equivalent to that, owned by the PT. The number of embedded appliances may vary from household to household. Parameters that are used to model each appliance include (a) Appliance power ratings, (b) Duration-of-use, (c) Time-of-use, and (d) Frequency-of-use. The behaviours of all embedded appliances are modelled to yield stochastic outcomes. The data for these parameters were obtained from [14]. These parameters are modelled using a probability distribution function expressed as a *triangular distribution (X,Y,Z)*, where X and Z are the possible minimum and maximum values of the parameters respectively and Y is the average value of the parameter.

3.3 Modeling a Community of CHDTs (i.e. CVPP-E)

In the model, CHDTs are placed in an environment called CVPP-E. The CVPP-E represent the community within which the CHDTs live. The CVPP-E is modelled as constituting a population of CHDTs. The population size and the ratio of different household sizes can be configured in the prototype. Within the CVPP-E environment, CHDTs can communicate among themselves via messages. The CVPP-E manager plays the role of the community manager and is responsible for the proposition of all vending opportunities to community members. The manager communicates such information through messages.

3.4 Modelling the Cognitive Capabilities of CHDTs

Community Status This item defines the long-term attributes that enable a CHDT to play specific roles in the community. A CHDT can assume the status of either a prosumer or a consumer. This status is determined at the model initialization stage. Once a status is assumed, the CHDT maintains it for the entire model run. A prosumer CHDT inherits a prosumer attribute (i.e., PV and a battery storage system) which enables it to play the roles of energy producer and consumer simultaneously.

A CHDT that inherits a consumer status fundamentally consumes energy and does not produce any. The ratio of prosumers to consumers population can also be configured. For instance, if there are a total population of 20 CHDTs in the community, a ratio of say: 90% prosumers to 10% consumers can be configured. Any combination or ratios between these two populations is possible.

Internal States. After a CHDT has assumed its community status, the attributes or preferences of the PT are modelled inside the CHDT as internal states. Having a

replica knowledge of the current attributes and preferences of the PT, and making basic decisions based on this knowledge is what gives the CHDT its cognitive capabilities. The internal states are modelled using state charts. State charts are used to represent the dynamic changes of behaviours in a system. State transitions are used to model changes in behaviour and these transitions can be triggered either by some internal or external event.

Degree of Delegation. This is also an internal state that is used to represent the level of delegated authority that the PT assigns to its counterpart CHDT. Two types of delegated authority are considered. These are:

*Full Delegation***.** This means that the CHDT has received delegated authority to defer or suspend the use of all deferrable loads embedded in it. For instance, a CHDT with four embedded deferrable loads may defer all four appliances.

Partial Delegation. A CHDT with this kind of delegated authority has limitations regarding the number of appliances that it can defer. In such instances, the PT may place some restrictions on the deferral of certain specific appliances.

Sizes of PV and Battery Systems. All prosumer CHDTs inherit a PV and battery storage system. A prosumer CHDT has cognisance of the capacities of installed PV and battery storage systems.

4 Scenario Selection and Demonstration of Modelling Technique

In this aspect of the study, we define some scenarios as well as parameters to be used in demonstrating the modelling technique as well as testing our developed prototype. To achieve this, we create a scenario that will enable the CHDTs to collaborate. Collaboration in this sense involves joint action by all the involved CHDTs to achieve a specific goal that is common to them all. The common goal, in this case, is termed "collaborative consumption" which involves a collective action taken by all CHDTs which is aimed at minimizing community consumption (within the proposed vending window) hoping to maximize the opportunity of vending renewable energy to the grid. The following parameters described below are used:

Communication for Collaboration. The community manager communicates via messages to the CHDTs in advance, giving them notice of an impending vending opportunity (VendOpp). The information that is communicated includes (i) Time for vending (V_T), and (ii) Vending window (V_W), which is the duration of vending. As an example, for this test scenario, $V_T = 24$ h after receiving notification and $V_W = 10$ h. The waiting time is the period between the time the CHDT received notification and the time vending begins.

Community Population. A population of 50 CHDTs were used in the simulation.

Table 1 Parameters for modelling the embedded household appliances [14]

Type of appliance	Annual power (kwh)			Peak periods		Number of wash cycles year
	Min	Average	Max	P1	P2	
Washing machine	15	178	700	5am–4 pm	5 pm–2am	284
Tumble dryer	64.25	497	1600	5am–12 pm	6 pm–11 pm	280
Dishwasher	33.32	315	608	5am–3am	6 pm–2am	270

Household Appliances. A total of three household appliances (deferrable loads) were considered. These are (a) Washing machine, (b) Dish washer, and (c) Tumble dryer. The parameters used to model each of these appliances are shown in Table 1. These parameters are data obtained from a survey conducted on domestic appliance usage in the UK in 2012 [14].

Installed PV System. For prosumers, four different types of installed PV systems are considered. A prosumer CHDT can inherit only one of these systems. The considered PV systems are: (a) BainSystem = 6.930 kW [15], (b) BrainSystem = 1.950 [15], (c) Helius = 3.99 kW [15], and (d) DaSS = 3.22 kW [15]. Data from these real-life systems are used to model the generation side of the model. These PV systems are not discussed in this study.

Degree of Delegation, The following delegated authority cases are considered:

- **Full Delegation**. A CHDT with this level of delegated authority can defer all three embedded appliances.
- **Partial Delegation, Double Appliance.** A CHDT with this level of delegated authority can defer any two of the embedded appliances.

Partial Delegation, Single Appliance This means the CHDT has delegated authority to defer any one of the embedded appliances. A flowchart showing the possible combination of the "degrees of delegation" is shown in Fig. 1. Furthermore, in Table 2, we have defined five different scenarios constituting different degrees of delegation in combination with different population sizes. The results and discussion section (Sect. 5) discusses the outcome of the model, considering these scenarios.

5 Results and Discussion

In RQ-1, we sought to find a way to model the cognitive capabilities of CHDTs. Figures 2a-c demonstrate the outcome of the model. As shown below, all active states of the model are depicted with dotted boundary lines, and inactive states are shown with continuous boundary lines. The active states are used to replicate the current attributes or preferences of the PT. In Fig. 2 the prosumer state of the

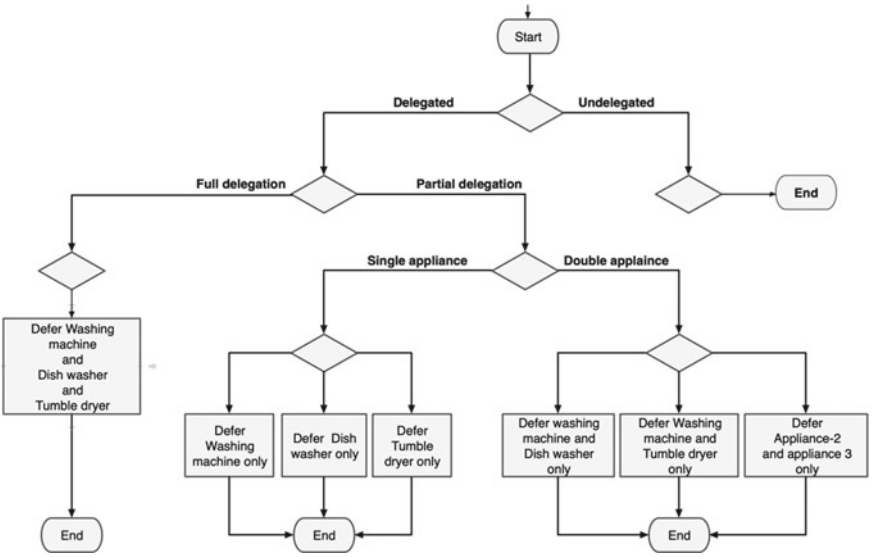

Fig. 1 Flow chart of the delegation process

Table 2 Scenario selection

Scenarios		Degree of delegation	Number of delegated appliances	Percentage of CHDT population (%)	
				Delegated	Undelegated
1	High population of delegated CHDTs	Full	3	100	0
2	Low population of delegated CHDTs	Full	3	10	90
3	High population of delegated CHDTs	Full	3	90	10
4	High population of delegated CHDTs	Partial	2	90	10
5	High population of delegated CHDTs	Partial	1	90	10

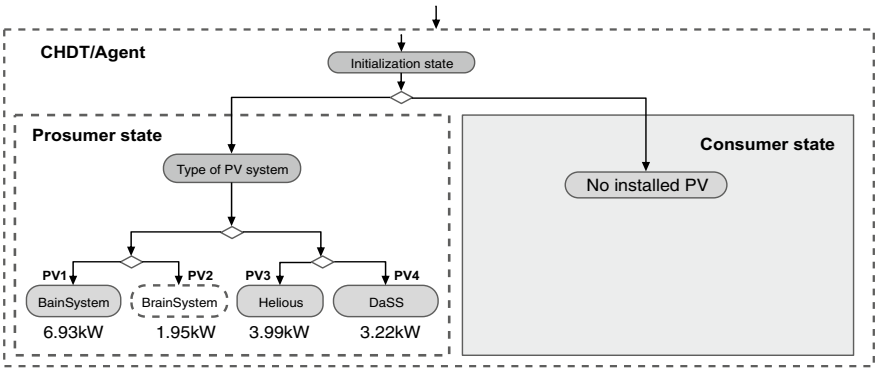

Fig. 2 Status as a prosumer with a 1.95 kW installed PV system (PV2-BrainSystem)

CHDT is active. Furthermore, an installed PV, named BrainSystem, with an installed capacity of 1.95 kW is also active. Similarly, Fig. 3 shows a CHDT with attributes of a consumer with no installed PV system. Finally, in Fig. 4, we illustrate a prosumer CHDT with full delegated authority.

In RQ-2, we sought to demonstrate how these CHDTs could use their cognitive capabilities to engage in some decision-making. In this instance, we seek to achieve collaborative consumption which requires the involved CHDTs to collectively adjust their energy consumption, aimed at achieving a common community goal.For the CHDTs to successfully make such collective decisions it is necessary that each one of them have cognisance of the flowing conditions: (a) The proposed vending time, (b) waiting time (c) vending window, and (d) degree of delegation. Using the scenario described in Table 1, the following global behavior is observed from the 50 CHDTs after they have made their respective decisions. Figure 5 represents scenario 1. In this scenario, we considered a high population of delegated CHDTs. The degree of the

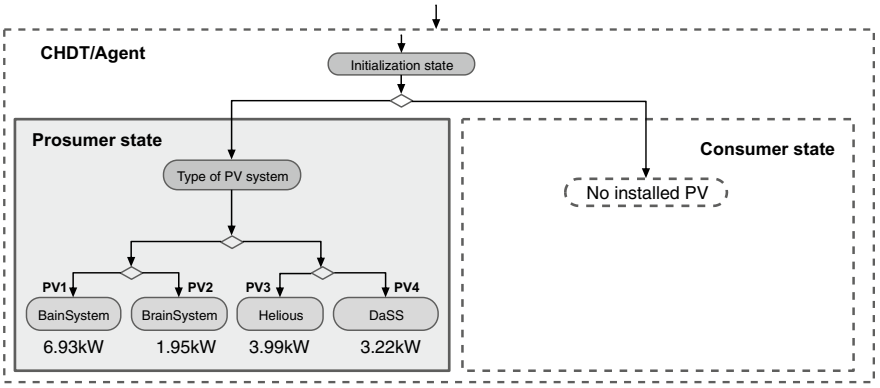

Fig. 3 Status as a consumer with no installed PV system

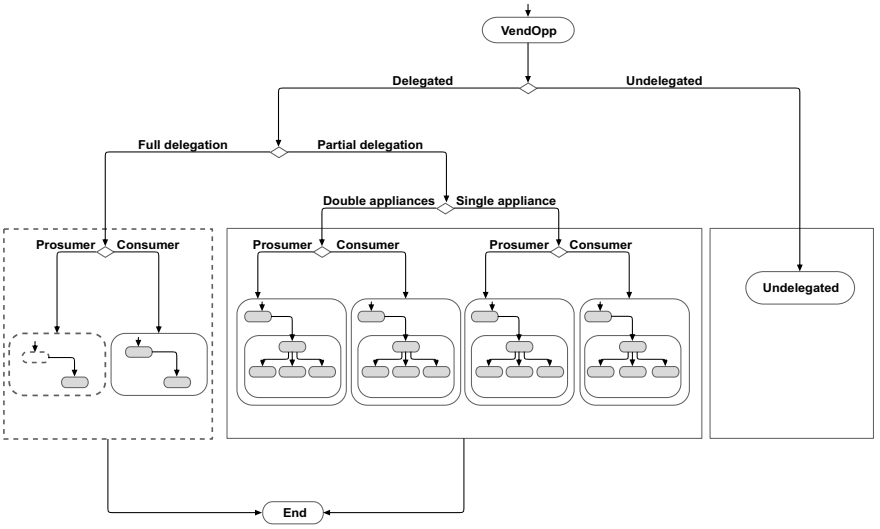

Fig. 4 Status as a prosumer with full delegation (All three appliances deferred)

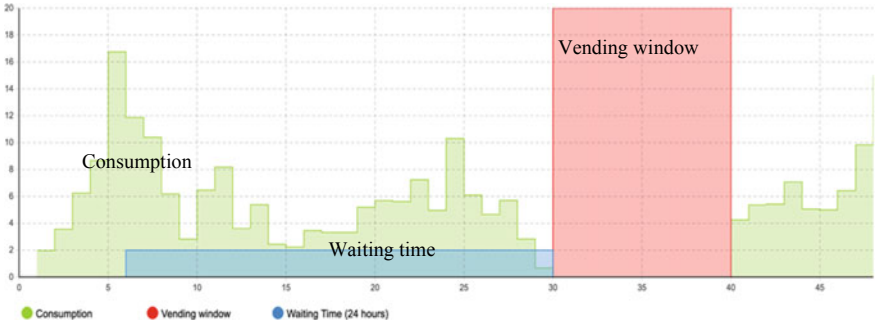

Fig. 5 Scenario of high population of delegated of CHDTs (100%) with full delegation

delegation was "full delegation". Furthermore, all CHDTs were delegated (100%). The results as shown in Fig. 5 suggests that all the CHDTs were cognisant of the waiting time. They were also cognisant of the vending window (10 h). It can also be observed that all the CHDTs implemented their delegated authority which was "full delegation". Evidence of the implementation of full delegation can be seen in the figure. It can be observed that during the vending window, consumption was zero. This is because they all suspended the use of all three embedded appliances when the waiting time was due, and the suspension lasted for the duration of the vending period. They all resumed consumption immediately after the vending period had elapsed. Figure 6 also represents the outcome of the model considering scenario 2. This scenario considered a low population of delegated CHDTs (10%). The degree of the delegation was full. It can be observed from the vending window that energy

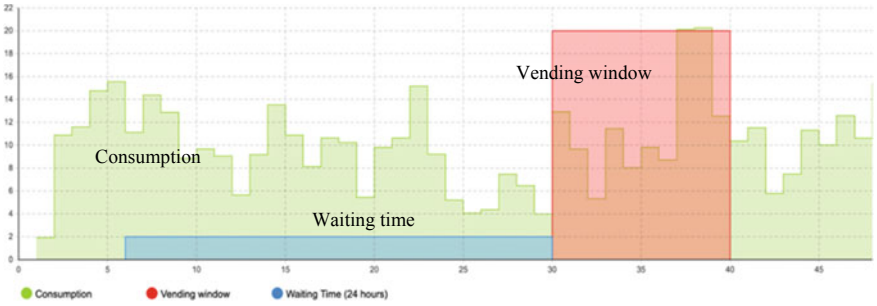

Fig. 6 Scenario of low population of delegated CHDTs (10%), high population of undelegated CHDTs (90%), full delegation

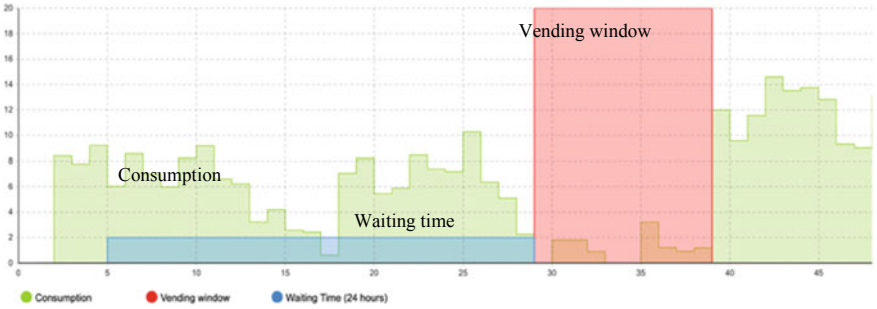

Fig. 7 High population of delegated of CHDTs (90%), low population of undelegated CHDTs (10%), full delegation

consumption was not affected as the number of CHDTs that deferred the use of their appliances were few (10%). The consumption observed within the vending widow was because of the 90% undelegated CHDTs. Furthermore, in Fig. 7, we considered scenario 3 which constitutes a high population of delegated CHDTs (90%) and a low population of undelegated CHDTs (10%). The degree of the delegation was full. It was observed that consumption was significantly reduced within the vending window. This was because the majority of the CHDTs (90%) delegated all three appliances during the period. The relatively small consumption that was recorded could be attributed to the 10% undelegated CHDTs.

The outcomes of scenarios 4 and 5 are captured in Figs. 8 and 9. In both scenarios, we considered partial delegation. In scenario 4 (Fig. 8) we considered partial delegation with double appliance. Subsequently, in scenario 5, (Fig. 9), we considered partial delegation with a single appliance. The results revealed that partial delegation with a double appliance yielded more energy savings as compared to the partial delegation with a single appliance. It can therefore be concluded that having a high population of delegated CHDTs, who have been given full delegated authority, could yield the most significant energy savings, that can facilitate the maximization of the

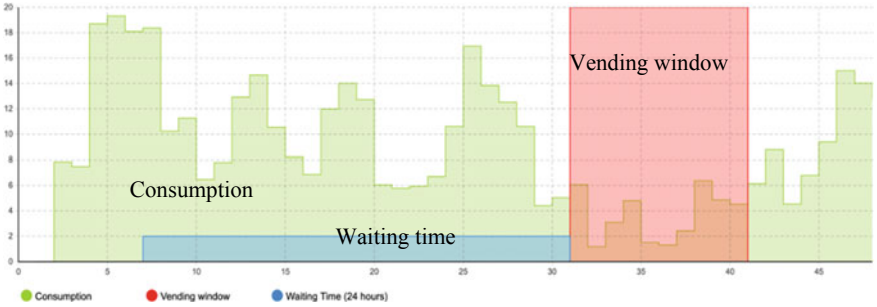

Fig. 8 High population of delegated CHDTs (90%), low population of undelegated CHDTs (10%), partial delegation, double appliances

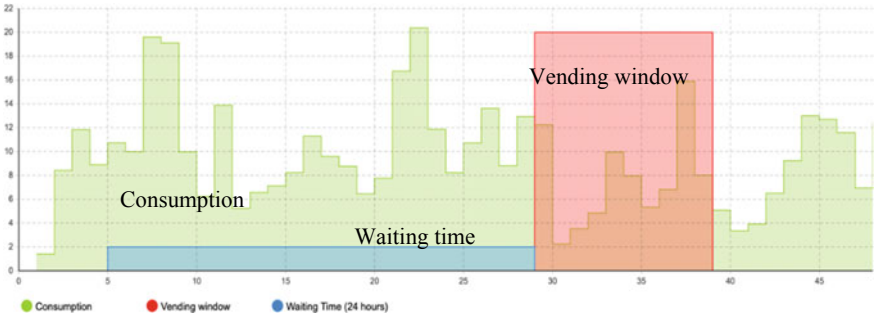

Fig. 9 High population of delegated CHDTs (90%) low population of undelegated CHDTs (10%), Partial delegation, single appliance

VendOpp. On the contrary, having a high population of undelegated CHDTs will adversely affect consumption within the vending window, which could minimize the VendOpp.

6 Conclusion and Future Works

The primary objective of this study was to demonstrate the feasibility of adopting CHDTs as autonomous entities that could assist as complimentary decision-making agents in households. To achieve this objective, a prototype model was developed using a multi-method approach. The prototype was tested using multiple scenarios. The outcome of the study has helped to establish the fact that CHDTs could act as complimentary decision-making agents as they can have cognisance of their status and states. The outcome further revealed that CHDTs could execute delegated instruction such as delegation of deferrable loads in accordance with the preferences of the physical household. Finally, CHDTs have been proven to be goal oriented such as

achieving some set goals like minimizing consumption and vending energy to the grid at some stipulated time. They can also take collective actions which are good bases for collaborations.

In future works, the decision-making capabilities, or behaviours of CHDTs will be explored further. Decision-making behaviors such as engaging in other collaborative behaviors will be investigated. Other behaviours such as having the capability to influence one another, particularly in the decision-making process will also be explored. Finally, the ability of CHDTs to adopt some form of social innovations will be studied. Delegation in the aspects of generation will also be investigated further.

Acknowledgements The authors acknowledge the Portuguese FCT program UIDB/00066/2020 for providing financial support for this work. The University of Energy and Natural Resources and UNINOVA CTS are hereby acknowledged for supporting this work with their research facilities and resources.

References

1. European Comission.: Energy performance of buildings directive (2019). [Online]. Available https://ec.europa.eu/energy/topics/energy-efficiency/energy-efficient-buildings/energy-performance-buildings-directive_en. Accessed 28 Mar2020
2. Hertwich, E.G., Peters, G.P.: Carbon footprint of nations: a global, trade-linked analysis. Environ. Sci. Technol. **43**(16), 6414–6420 (2009)
3. Nokia (2021) Where can CSPs use digital twins | Nokia. [Online] Available https://www.nokia.com/networks/insights/where-can-csps-use-digital-twins/?did=D000000005I9&gclid=CjwKCAjwq9mLBhB2EiwAuYdMtT5XcHe0BWC0rt89fK8E8Wu5MXy2FmXDFvlI2m7CeOSITI8xjedW9xoC5wkQAvD_BwE.Accessed 25 Oct 2021
4. Adu-Kankam, K.O., Camarinha-matos, L.: Towards a hybrid model for the diffusion of innovation in energy communities. In: Technological Innovation for Applied AI Systems . DoCEIS 2021 . IFIP Advances in Information and Communication, 2021, no. June, pp. 175–188
5. Ferrada, F., Camarinha-Matos, L.M.: A modelling framework for collaborative network emotions. Enterp. Inf. Syst. **13**(7–8), 1164–1194 (2019)
6. Graça, P., Camarinha-Matos, L.M., Filipa, F.: A model to assess collaboration performance in a collaborative business ecosystem. In: DoCEIS 2019, IFIP Advances in Information and Communication Technology, 2019, vol. 553, pp. 3–13
7. Adu-Kankam, K.O., Camarinha-Matos, L.M.: Towards collaborative virtual power plants: trends and convergence. Sustain. Energy, Grids Netw. **16**, 217–230 (2018)
8. Adu-Kankam, K.O., Camarinha-Matos, L.M.: Towards collaborative virtual power plants. Technol. Innov. Resilient Syst. DoCEIS **2018**, 28–39 (2018)
9. Adu-Kankam, K.O., Camarinha-Matos, L.M.: Emerging community energy ecosystems: analysis of organizational and governance structures of selected representative cases. Technol. Innov. Indus. Serv. **553**, 24–40 (2019)
10. Agouzoul, A., Tabaa, M., Chegari, B., Simeu, E., Dandache, A., Alami, K.: Towards a digital twin model for building energy management: case of Morocco. Procedia Comput. Sci. **184**, 404–410 (2021)
11. Hunhevicz, J.J., Motie, M., Hall, D.M.: Digital building twins and blockchain for performance-based (Smart) contracts. Autom. Constr. 133, 103981 (2021)

12. AnyLogic.: AnyLogic: simulation modeling software (2018) [Online] Available https://www.anylogic.com/. Accessed 13 Feb 2020
13. Unified Modeling Language (UML) | State Diagrams (2021) [Online]. Available https://www.geeksforgeeks.org/unified-modeling-language-uml-state-diagrams/. Accessed 26 Oct 2021
14. Zimmermann, J.-P. et al.: Household electricity survey: a study of domestic electrical product usage. Milton Keynes (2012)
15. PVOutput (2021) [Online] Available https://pvoutput.org/. Accessed 08 Oct 2021

Design and Simulation of High Input Power Factor AC/DC Converter Based on a Single-Phase PWM Rectifier

Mohammed Chaker, Amine El Houre, Driss Yousfi, Moussa Reddak, Mustapha Kourchi, Jamal Bouchnaif, and Ahmed Benlarabi

Abstract This article proposes a high efficiency power supply with a high input power factor and a low THD (Total Harmonic Distortion), which can be used in many applications to power different DC loads with great satisfaction from the distributor of electrical energy. It consists of a single-phase PWM rectifier that contains an internal regulation loop that compels the grid current to be sinusoidal, and in phase with the grid voltage, as well as an output voltage regulation loop. The effectiveness of this power converter is demonstrated through simulation results comparison between its performances and those of a conventional diode based rectifier.

Keywords AC-DC converter · Power supply · PWM rectifier · Power factor · THD · Harmonics · Electrical grid

1 Introduction

The discipline of power electronics has seen tremendous growth in recent years, particularly in the areas of energy regulation, conversion, and distribution. This is owing to the increased demand for electronic and electrical applications [1, 2].

M. Chaker (✉) · A. El Houre · D. Yousfi · M. Reddak
ESETI Laboratory, National School of Applied Sciences, Mohammed First University, Oujda, Morocco

M. Kourchi
ESEM Laboratory, Higher School of Technology, Ibn Zohr University, Agadir, Morocco
e-mail: m.kourchi@uiz.ac.ma

J. Bouchnaif
EEM Laboratory, Higher School of Technology, Mohammed First University, Oujda, Morocco
e-mail: j.bouchnaif@ump.ac.ma

A. Benlarabi
Research Institute of Solar Energy and New Energies "IRESEN", Green Energy Park station, Benguerir, Morocco
e-mail: benlarabi@iresen.org

M. Bendaoud et al. (eds.), *The Proceedings of the International Conference on Electrical Systems & Automation*, https://doi.org/10.1007/978-981-19-0039-6_7

For proper operation, many electrical and electronic devices require a DC voltage at their inputs. The use of rectifiers is necessary to obtain such voltage from the AC electrical grid [3, 4].

Previously, diode rectifiers were used to convert energy from AC to DC. These uncontrolled rectifiers can only produce a constant DC voltage as a function of grid voltage. Controlled rectifiers using SCRs (Silicon Controlled Rectifiers) have been developed as power electronic devices and control topologies have progressed. These SCR rectifiers can generate a variable DC output voltage that is dependent on line voltage and firing angle [3, 5].

Rectifiers based on diodes or SCRs are major pollutants of the electrical grid. For example, a diode bridge rectifier circuit with a large capacitor in parallel consumes line current in the form of thin pulses at line voltage peaks, which degrades the power quality and shortens the life of electronic equipment powered by these conventional rectifiers [6–8].

PWM (Pulse Width Modulation) rectifiers are characterized by a sinusoidal input current with low harmonics, an almost unitary power factor, and bi-directionality of the energy flow, in addition to the possibility of adjusting the output DC voltage as needed [9–11].

By altering the firing angle in an SCR rectifier, the output DC voltage can be modified from zero to the voltage achieved from a diode rectifier.

The above power converter works at a low switching frequency and induces a high harmonic distortion rate. These issues are fixed in the PWM rectifier. Furthermore, the output DC voltage can be kept above that obtained from a diode bridge or SCR rectifier. For this reason, the PWM rectifier is also known as a boost rectifier [12, 13].

2 Study of the Proposed AC/DC Power Supply

2.1 Proposed Power Supply Topology

Figure 1 shows the power circuit scheme of the designed power supply. A transformer is used to reduce the amplitude of the grid voltage and to benefit from the galvanic isolation between the electrical grid and the power converter, an inductor was inserted between the transformer and the PWM rectifier to ensure the control of the input current and to participate in the output voltage boosting process. The rectifier itself is a full-bridge circuit made of four power transistors with diodes connected in anti-parallel. At the output of this converter, a capacitor that ensures the filtering of the DC bus, and a resistor that constitutes the load, are connected in parallel.

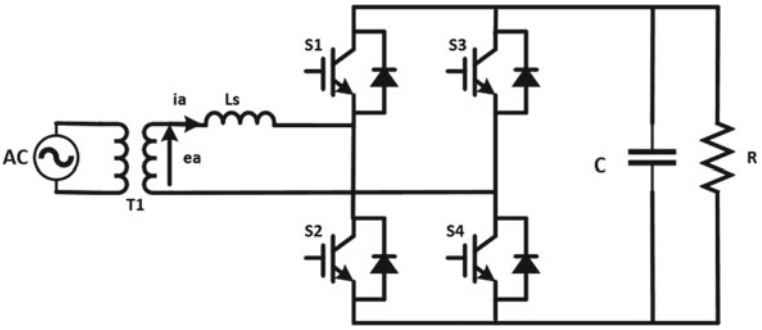

Fig. 1 The power circuit scheme of the proposed power supply

2.2 Modeling of the PWM Rectifier

The Objectives of the PWM rectifier are:

- Ensure a DC voltage through the load R with a few ripples as possible.
- Have a sinusoidal input current in phase with the input voltage.
- Have an almost unitary power factor.

In Fig. 1, the impedance on the AC side is modeled as an inductance Ls in series with an internal resistance Rs, which is neglected in our case. C is the capacitance of the capacitor on the DC side and R represents the load resistance. e_a and i_a represent the input voltage and current, respectively. The voltage and current of the DC bus are u_{dc} and i_{dc}.

In PWM rectifier control, it can be observed that there are two control loops; the inner loop for input current control and the outer loop for DC voltage control. Regarding the first one, the model is considered as a first-order RL circuit.

The mathematical model of the single-phase PWM rectifier can be given by Eq. (1).

$$\begin{cases} L_s \frac{di_a}{dt} + R_s i_a = e_a - u_{dc} \\ C \frac{du_{dc}}{dt} = i_a - \frac{u_{dc}}{R} \end{cases} \tag{1}$$

The diagram of the instantaneous active power is presented in Fig. 2.

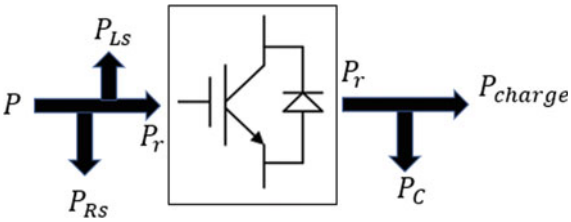

Fig. 2 The diagram of the instantaneous active power

When the converter functions in rectifier mode, Eq. (2) and Eq. (3) can be obtained according to the power flow.

$$e_d i_d + e_q i_q = R_s\left(i_d^2 + i_q^2\right) + \frac{1}{2}L_s\frac{d}{dt}\left(i_d^2 + i_q^2\right) + u_d i_d + u_q i_q \tag{2}$$

$$u_d i_d + u_q i_q = u_{dc} C\frac{du_{dc}}{dt} + \frac{u_{dc}^2}{R} \tag{3}$$

The d axis of dq-referential follows the line voltage of the power grid, meaning that e_d and e_q are equal to the maximum value of the grid voltage and zero, respectively. The power losses in R_s can be neglected and the grid is considered to have a pure sinusoidal voltage, so e_d and e_q can be considered as a constant.

The application of a marginal perturbation to the state variables (i_d, i_q, u_{dc}) as shown in Eq. (4) and the exploitation of Eqs. (2), (3), and (4), resulted in the Eq. (5) by separating the second derivative terms and the DC components. Since the rectifier functions with a unit power factor, I_q is neglected.

$$\begin{cases} i_d = I_d + \widehat{i_d} \\ i_q = I_q + \widehat{i_q} \\ u_{dc} = U_{dc} + \widehat{u_{dc}} \end{cases} \tag{4}$$

$$e_d i_d - L_s I_d\frac{d\widehat{i_d}}{dt} = C u_{dc}\frac{d\widehat{u_{dc}}}{dt} + 2u_{dc}\frac{\widehat{u_{dc}}}{R} \tag{5}$$

2.3 Control of the PWM Rectifier

By applying the Laplace transformation to Eq. (5), the transfer function of the output DC voltage over the active current is obtained as follow:

$$G(s) = \frac{\widehat{u_{dc}}}{\widehat{i_d}} = \frac{\frac{Re_d}{2U_{dc}}\left(1 - \frac{L_S I_d}{e_d}s\right)}{1 + 0.5RCs} \tag{6}$$

The output DC voltage control can be modeled as in Fig. 3.

Where K_{pv} and K_{iv} represent the proportional and integral coefficients of the PI external loop voltage regulator, respectively.

The PI controller can modify the transient regime of the system by adding zero to the closed-loop transfer function. The pole compensation method is better suited to solving this problem when calculating the parameters K_{pv} and K_{iv}. It entails setting the controller zero to one pole of the transfer function of the system to be controlled, as well as a time constant τ_{bf} that meets the objectives.

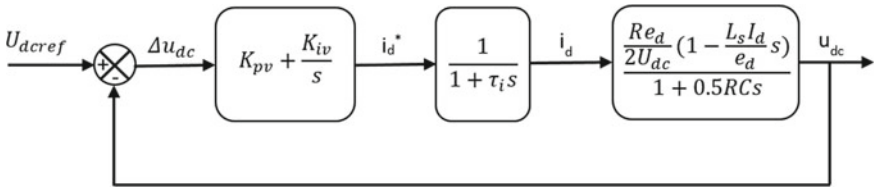

Fig. 3 The control block for the external voltage loop

As a result, Eqs. (7) and (8) give the gains of the controller of the output voltage regulation loop.

$$K_{pv} = \frac{U_{dc}C}{\tau_{bf} e_d} \tag{7}$$

$$K_{iv} = \frac{2U_{dc}}{\tau_{bf} Re_d} \tag{8}$$

3 Simulation Results

The proposed control of the power topology of the single-phase PWM rectifier is simulated under MATLAB-Simulink environment (Fig. 4). The switching frequency of the power transistors is equal to 5 kHz.

Figure 5 shows the DC voltage generated by the PWM rectifier with a voltage reference of 100 V, as well as the grid voltage and current. For the grid voltage, we have reduced it to 60 V RMS using the isolation transformer.

These results show that the mains current and voltage are almost sinusoidal and in phase. This means that the DC bus voltage regulation has been performed with an almost unitary power factor.

To corroborate these findings, we have measured the active and reactive power exchanged with the electrical grid; we found out that the power factor of this designed supply is nearly unitary (0.9863).

Following a spectral analysis of the absorbed current of the grid (Fig. 6), we can see that the THD of this current is equal to 2.48%, which is a much desired value by the electrical energy distributors. The weak harmonics that are observed around the fundamental are due to the numerical method taken during the simulation.

Figure 7 shows that the waveform of the absorbed line current by a diode rectifier is pulsed. Spectral analysis of this current is performed to compare the quality of this conventional rectifier to that of the PWM rectifier in terms of harmonics. This study (Fig. 8) indicates that this current has a THD of 89.19% and is packed with harmonics. With such current, the other equipment connected to the grid can be

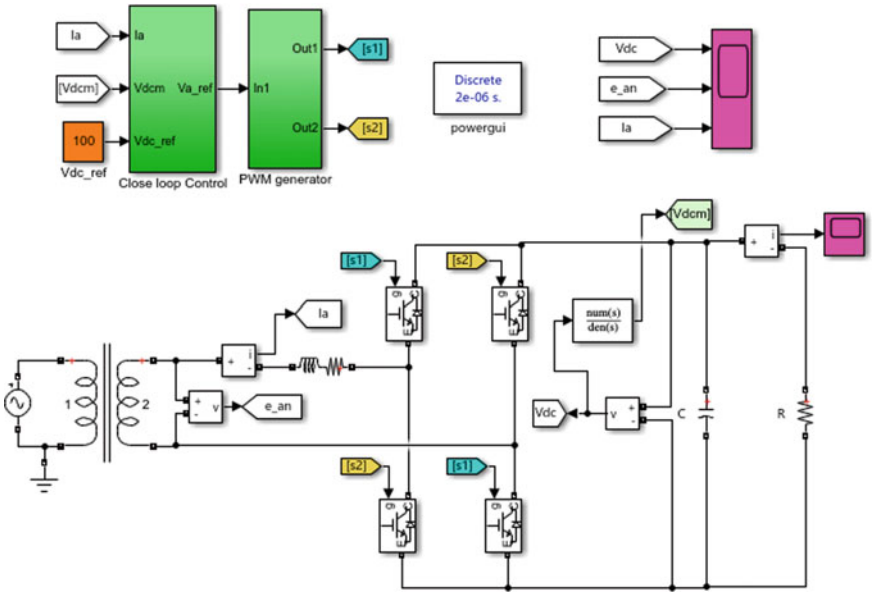

Fig. 4 The Simulink model of the designed power converter

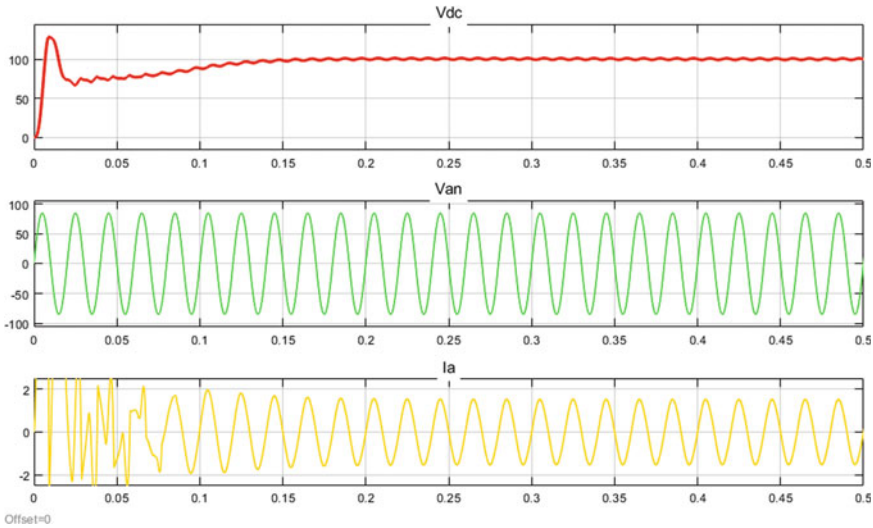

Fig. 5 The PWM rectifier waveforms obtained during the simulation

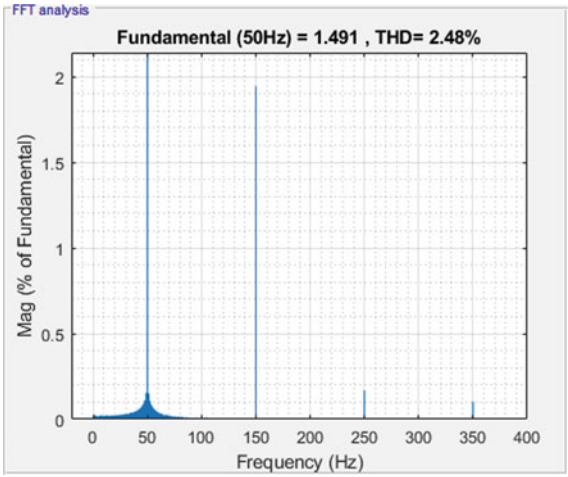

Fig. 6 The spectral analysis of the absorbed grid current by the PWM rectifier

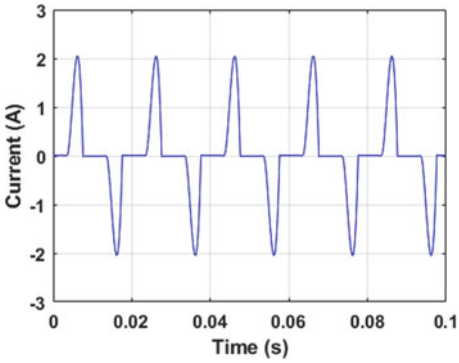

Fig. 7 The absorbed grid current by the diode rectifier

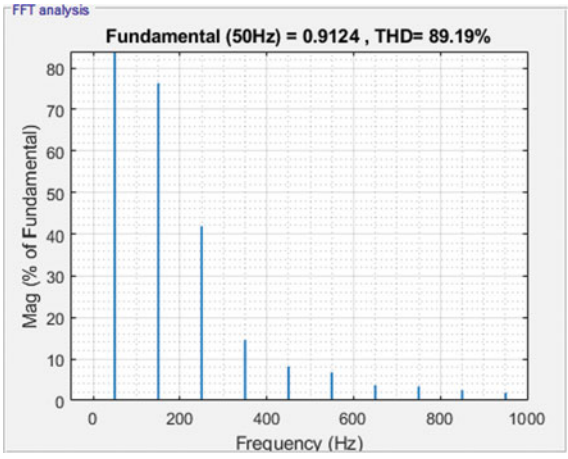

Fig. 8 The spectral analysis of the absorbed grid current by the diode based rectifier

disturbed. It is worth noting that this polluting diode converter has a bad power factor equal to 0.7121.

Figure 9 shows that the voltage delivered by the designed power converter (PWM rectifier) has a good transient regime that tracks reference steps with a short response time and no overshoot. These results also show that in the steady-state, the generated voltage follows exactly the reference voltage without any static error.

To verify the robustness of the implemented PI controller, we have tested the designed PWM rectifier under electrical load variations by always applying a voltage reference equal to 100 V. At the top of Fig. 10, we observe that the output voltage follows the reference with the presence of a small overshoot at times of load variation that does not exceed 3.5 V. The PI controller corrects these overshoots in a time of

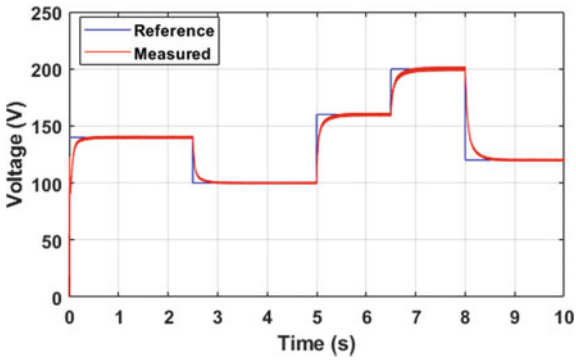

Fig. 9 The reference and the generated voltage by the designed AC/DC power converter

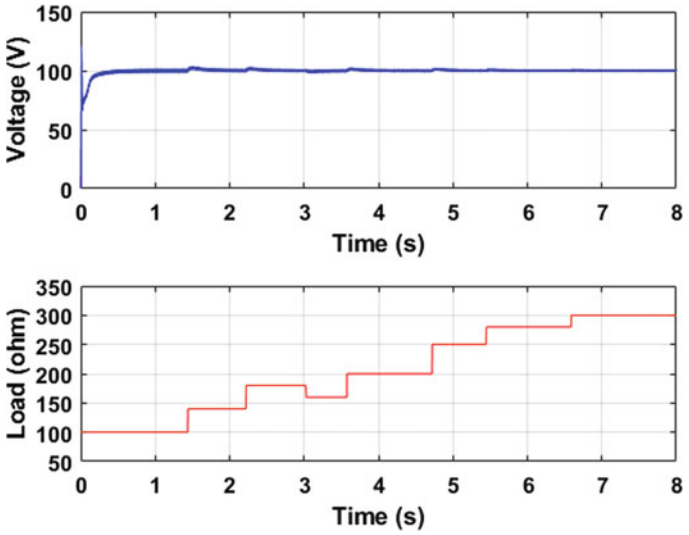

Fig. 10 The output voltage and the profile of the electrical load variations

less than 0.3 s. We note that the profile of the variation of the load is presented by the red curve at the bottom of Fig. 10.

4 Conclusion

In this work, a high-efficiency AC/DC power converter with a high input power factor and a low THD capable of attaining a significant power level has been proposed. The power circuit consists essentially of a single-phase PWM rectifier, which is an AC to DC converter using power transistors (Insulated-gate bipolar transistors in our case).

On one hand, PI controllers are used to force the current drawn from the electrical grid to be sinusoidal and in phase with the grid voltage, resulting in fewer harmonics and a power factor near unity. On the other hand, the controller adjusts the output voltage to meet the needs of the DC load.

The simulation results, relative to the designed power supply, show the good performance of this power topology. On grid side, the THD of current is equal to 2.48% and the power factor is equal to 0.98. On the load side, the results show robustness in terms of rejection of disturbances and output voltage reference tracking. Towards the end, simulation results of a diode rectifier show its poor performance compared to that obtained by the PWM rectifier.

In perspective, experimental validation of the proposed control technique will be carried out, and new control techniques will be employed to enhance the performance of this power supply topology.

Acknowledgements This work is supported by Moroccan Research Institute for Solar Energy and New Energies (IRESEN).

References

1. Mohan, N., Undeland, T.M., Robbins, W.P.: Power Electronics: Converters, Applications, and Design. John Wiley & Sons, Hoboken, NJ (2003)
2. de León Puig, N.I.P., Bozalakov, D., Acho, L., Vandevelde, L., Rodellar, J.: An adaptive–predictive control scheme with dynamic hysteresis modulation applied to a DC–DC buck converter. ISA Trans. **105**, 240–255 (2020). https://doi.org/10.1016/j.isatra.2020.05.015
3. Mitra, A., Chowdhuri, S.: Analysis of single phase PWM rectifier for different applications. J. Inst. Eng. India Ser. B. **98**, 161–169 (2017). https://doi.org/10.1007/s40031-016-0217-9
4. Rodriguez, J.R., Dixon, J.W., Espinoza, J.R., Pontt, J., Lezana, P.: PWM regenerative rectifiers: state of the art. IEEE Trans. Ind. Electron. **52**, 5–22 (2005). https://doi.org/10.1109/TIE.2004.841149
5. Siva Prasad, J.S., Bhavsar, T., Ghosh, R., Narayanan, G.: Vector control of three-phase AC/DC front-end converter. Sadhana **33**, 591–613 (2008). https://doi.org/10.1007/s12046-008-0045-y
6. Gnanavadivel, J., Senthil Kumar, N., Yogalakshmi, P.: Comparative study of PI, Fuzzy and Fuzzy tuned PI controllers for single-phase AC-DC three-level converter. J. Electric. Eng. Technol. **12**, 78–90 (2017). https://doi.org/10.5370/JEET.2017.12.1.078

7. Lakshmi, M.B., Thangasankaran, R., Gnanavadivel, J., Christa, S.T.J.: Performance Evaluation of Fuzzy Controlled Single Phase PWM Rectifier. In: 2018 Second International Conference on Electronics, Communication and Aerospace Technology (ICECA), pp. 1974–1979. IEEE, Coimbatore (2018)
8. Kang, L., Zhang, J., Zhou, H., Zhao, Z., Duan, X.: Model predictive current control with fixed switching frequency and dead-time compensation for single-phase PWM rectifier. Electronics **10**, 426 (2021). https://doi.org/10.3390/electronics10040426
9. Eskandari-Torbati, H., Khaburi, D.A., Eskandari-Torbati, V.: Control of three phase PWM rectifier using virtual flux-based predictive direct power control and SVM under harmonic conditions: DPC method for three phase PWM rectifier using dead beat controL. Int. J. Numer. Model. **29**, 205–221 (2016). https://doi.org/10.1002/jnm.2064
10. Vaideeswaran, V., Sankar, N.: Control Techniques of Three Phase PWM Rectifier. 8, 6
11. Teixeira, R.D.A., Silva, W.L.A., Pessoa, G.A.P.D.C.A., Neto, J.T.C., Villarreal, E.R.L., Salazar, A.O., Lock, A.S.: One cycle control of a PWM rectifier a new approach. Energies **13**, 5523 (2020). https://doi.org/10.3390/en13205523
12. Zhang, C., Yu, S., Ge, X.: A Stationary-frame current vector control strategy for single-phase PWM rectifier. IEEE Trans. Veh. Technol. **68**, 2640–2651 (2019). https://doi.org/10.1109/TVT.2019.2895290
13. Wan, X., Ren, J., Wan, T., Jing, S., Xiong, S., Guo, J.: A control strategy of single phase voltage source PWM rectifier under rotating coordinate. In: 2017 2nd International Conference on Power and Renewable Energy (ICPRE). pp. 162–165. IEEE, Chengdu (2017)

Characteristics Dynamic Analysis and Modeling of Quasi-Z-Source Inverters for PV Applications

E. Jaoide, F. El Aamri, M. Outazkrit, A. Radouane, and Az. Mouhsen

Abstract The Z-Source Inverter (ZSI) was found to be suitable for grid-connected PV systems due to its ability to boost and convert voltage in a single stage. Compared to the conventional inverter, the ZSI inverter has a new control parameter in addition to the modulation index, which is the shoot-through duty ratio. The Quasi-Z Source Inverter (QZSI) is the modern topology derived from the ZSI and the most widely used in power generation, mainly due to the improved input profiles. Nevertheless, the design and control of the impedance-source inverter requires more attention than the conventional inverter, especially for renewable energy sources as PV systems. This paper investigates the operating principle of the QZSI in the steady-state, a dynamic small-signal model is also developed, the simulation results of the influence of the different parameters are discussed.

Keywords Quasi-Z-source inverter · PV application · Conventional inverter · Small signal · Shoot-through

1 Introduction

Due to the lack of fossil fuels in the world, the return to renewable energy has become crucial. Photovoltaic power generation has been extremely important in recent years as it has become less costly and more efficient, with several technological innovations in this field [1].

For reasons of efficiency and reliability, the power converter area can neither keep up with the development of the renewable energy generation, indeed, inverters have been the topic of much research and development over the last few decades. New

E. Jaoide (✉) · M. Outazkrit · A. Radouane · Az. Mouhsen
Faculty of Science and Technology, IRM Laboratory, Hassan First University of Settat, Settat, Morocco
e-mail: e.jaoide@uhp.ac.ma

F. El Aamri
Hassan II University, Mohammadia, Morocco

M. Bendaoud et al. (eds.), *The Proceedings of the International Conference on Electrical Systems & Automation*, https://doi.org/10.1007/978-981-19-0039-6_8

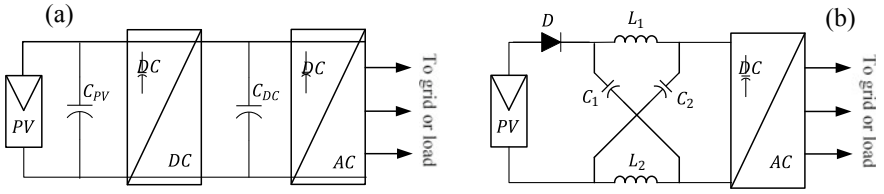

Fig. 1 **a** conventional two stage PV conversion, **b** Z-source inverter

solutions and topologies are always aimed at managing energy recovery and power management for photovoltaic (PV) applications [1].

The voltage supplied by a photovoltaic generator is usually low and not sufficient to power a grid-connected DC/AC converter. An elevation stage is therefore necessary, PV systems are currently connected to the grid via PV inverters, such two-stage architecture is usually implemented using a boost converter, in order to regulate the PV source output voltage and a voltage source inverter (VSI) in order to achieve the inversion operation as shown in Fig. 1a. This type of architecture suffers from reduced efficiency, higher cost, and larger size [1–3].

About twenty years ago, a DC-AC single-stage converter known as a Z-source inverter (ZSI) (Fig. 1b) appeared in the literature [2]. This new converter replaces the "DC/DC converter plus inverter" combination, this family of power conditioning stages has become a more suitable solution to overcome the limitations of the two-stage configuration, which is vital for variable or less sufficient voltage sources, such as PV energy sources. The ZSI is, in fact, equipped with a hybrid L-C cross impedance network arranged in an "X" shape, which allows the addition of inverter arm short-circuit states. Indeed, through a specific control strategy, this type of converter allows to lower or to raise the voltage with a minimum of components and a certainly low cost [1, 2].

Several modifications of the original topology are proposed in the literature [3, 4], All these various topologies are obtained by changing the parent structure (Fig. 1b) or by rearranging the inductor and capacitor connections. The most interesting feature of the ZSI and his derived topologies is that we can obtain an output voltage theoretically variable from zero to infinity at any given input source voltage [1, 3].

For PV applications, the discontinuous input current of ZSI does not allow the extraction of the maximum power from the PV source, to overcome this problem, the Quasi-Z-Source Inverter (QZSI) was designed [3–5], this topology inherits all the characteristics of ZSI with a continuous input current.

The novel inverter topology QZSI (Fig. 2) is largely used with renewable sources, with the PV systems in particular [4, 6–9]. It provides many advantages compared to the original ZSI topology. These benefits include improved input profiles and reduced voltage ratings of passive components.

This paper presents the QZSI converter as the famous converter that can bypass input voltage drops in a single-stage conversion. Also, a study and modeling of this converter will be developed.

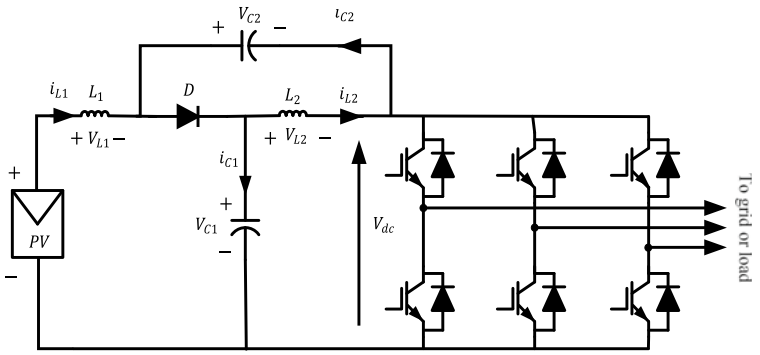

Fig. 2 qZSI with continuous input current for PV application

2 Operating Principle

Even though the many different topologies of these impedance source inverters, they use a similar basic operating principle as the original ZSI [2]. The basic operating principle involves the use of an additional switching state to the standard eight states of the space vector modulation, which is used with the classic three-phase inverter. Indeed, the insertion of the impedance network between the DC source and the converter allows.

the converter arms to short-circuit. This additional state is known as the "shoot-through" (ST) state and it is the mechanism used to boost the input voltage. In this state, the inverter operates as a short circuit by simultaneously switching on at least two-phase leg switches. Note that, The ST state is not allowed in the conventional VSI. On other hand, in the non-shoot through the state (called active or zero states), the inverter operates like the conventional VSI, in this state the three-phase inverter is equivalent to a current source.

The operating principle of the QZSI is based on two main states [2]:

2.1 Non-shoot-Through State (Non-ST)

The conventional three-phase inverter (Fig. 1a) uses eight standard switching states to modulate the six power switches and to perform the inverting operation. These standards states comprise two null states (when all upper or lower switches are activated) and six active states. The equivalent circuit is given by Fig. 3b, during the non-ST states, the inverter operates as a current source, the capacitor voltage ripple is neglected and the dc-link voltage is equal to a constant value [1, 2]. it is mentioned that the diode is ON and the impedance network capacitors (C_1 and C_2) are charged in this state [6].

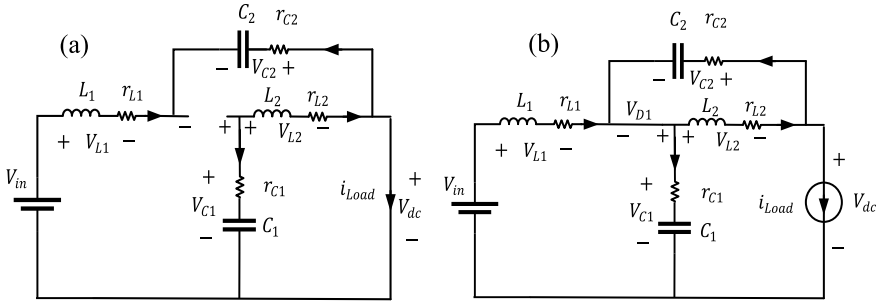

Fig. 3 Equivalent circuit of qZSI: **a** Shoot through state; **b** non-shoot-through state

2.2 Shoot-Through State (ST)

This state is allowed in ZSI family and should be introduced into any zero state so as not to impact the active states, and therefore, the output AC voltage. in this state, the inverter is equivalent to a short circuit and Vdc is equal to zero as illustrated in Fig. 3a. The inductances charge through the capacitors, the diode in reverse, the inductor L_1 charges through the DC source and the C_2 capacitor, the C_1 capacitor discharges into the inductor L_2 [6].

3 Steady-State Modeling

3.1 Boost factor and obtainable output voltage

We take T_C as the switching cycle, T_S as the interval of the shoot-through state and T_{NS} the interval of the non-shoot-through state, with, $T_C = T_S + T_{NS}$ and we define $D = {}^{T_S}/_{T_C}$ as the shoot-through duty ratio. From Fig. 3a, (we neglect the internal resistances of the inductors and the series resistances of the capacitors), during the T_S interval, we have:

$$v_d = -(V_{C1} + V_{C2}), \quad V_{dc} = 0, \quad v_{L1} = V_{C2} + V_{in}, \quad v_{L2} = V_{C1} \tag{1}$$

From Fig. 3b, during the T_{NS} interval, one may can have:

$$v_d = 0, \quad V_{dc} = V_{C1} + V_{C2}, \quad v_{L1} = V_{in} - V_{C1}, \quad v_{L2} = -V_{C2} \tag{2}$$

Over one switching cycle at the steady-state, the average voltage of the inductors is zero, so from the previous Eqs. (1) and (2) we have:

$$V_{L1} = \overline{v}_{L1} = D(V_{C2} + V_{in}) + (1 - D)(V_{C1} - V_{in}) = 0 \tag{3}$$

$$V_{L2} = \overline{v}_{L2} = DV_{C1} + (1 - D)(-V_{C2}) = 0 \tag{4}$$

We can therefore deduce the following expressions:

$$V_{C1} = \frac{1 - D}{1 - 2D} V_{in} \quad \text{and} \quad V_{C2} = \frac{D}{1 - 2D} V_{in} \tag{5}$$

The peak input voltage of the inverter in the active state is given by the following expression:

$$V_{dc} = V_{C1} + V_{C2} = \frac{1}{1 - 2D} V_{in} = BV_{in} \tag{6}$$

The ratio of the output voltage of the impedance network to the DC input voltage $= {}^{1}/_{1 - 2D}$, B is the boost factor of the QZSI. Theoretically, the elevation factor can vary from one to infinity by varying D from 0 to 0.5 [1–5].

3.2 Steady State Model

As mentioned above the impedance network of QZSI and shoot-through duty ratio are used to boost the input voltage to desired dc-link voltage. The QZS network (qZSN) model will be the average of the QZSN models for each state (ST state and NST state) [1–6]. For the accuracy of the mathematical model, the internal resistances of the inductors and the series resistances of the capacitors will be taken into account in the rest of this study, Fig. 3 shows the directions of the inductor currents and the capacitor voltage of the impedance network, where r_C is the series resistance of the capacitors and r_L is the stray resistance of the inductors. The chosen state vector is formed by capacitors voltages and the inductors currents [1, 6–10], thus, $x = \left[i_{L1}\ i_{L2}\ v_{C1}\ v_{C2} \right]^T$. The system inputs will be the inverter output current and input voltage, then, $u = \left[v_{in}\ i_{Load} \right]^T$, while the output vector is composed by the capacitor voltage and the inductor current $y = \left[i_{L1}\ v_{C1} \right]^T$.

As in [1–6], let $C = C_1 = C_2$ and $L = L_1 = L_2$, the parasite resistances of inductors $r_L = r_{L1} = r_{L2}$, and the equivalent series resistance of capacitors, $r_C = r_{C1} = r_{C2}$.

According to Fig. 3a the dynamics of the inductors L_1, L_2 and capacitors C_1 and C_2 during the ST state can be expressed as:

$$
\begin{aligned}
L\frac{di_{L1}}{dt} &= -(r_L + r_C)i_{L1} + v_{C2} + V_{in} \\
L\frac{di_{L2}}{dt} &= -(r_L + r_C)i_{L2} + v_{C1} \\
C\frac{dv_{C1}}{dt} &= -i_{L2} \\
C\frac{dv_{C2}}{dt} &= -i_{L1}
\end{aligned}
\tag{7}
$$

which is written as:

$$
\begin{aligned}
F\dot{x} = A_1 x + B_1 u &= \begin{bmatrix} L & 0 & 0 & 0 \\ 0 & L & 0 & 0 \\ 0 & 0 & C & 0 \\ 0 & 0 & 0 & C \end{bmatrix} \bullet \begin{bmatrix} \dot{i}_{L1} \\ \dot{i}_{L2} \\ \dot{v}_{C1} \\ \dot{v}_{C2} \end{bmatrix} \\
&= \begin{bmatrix} -(r_L + r_C) & 0 & 0 & 1 \\ 0 & -(r_L + r_C) & 1 & 0 \\ 0 & -1 & 0 & 0 \\ -1 & 0 & 0 & C \end{bmatrix} \bullet \begin{bmatrix} i_{L1} \\ i_{L2} \\ v_{C1} \\ v_{C2} \end{bmatrix} + \begin{bmatrix} 1 & 0 \\ 0 & 0 \\ 0 & 0 \\ 0 & 0 \end{bmatrix} \bullet \begin{bmatrix} V_{in} \\ I_{Load} \end{bmatrix}
\end{aligned}
\tag{8}
$$

According to Fig. 3b. the dynamics of the inductors L_1, L_2, C_1, and C_2 during the non-ST state can be expressed as:

$$
\begin{aligned}
F\dot{x} = A_2 x + B_2 u &= \begin{bmatrix} L & 0 & 0 & 0 \\ 0 & L & 0 & 0 \\ 0 & 0 & C & 0 \\ 0 & 0 & 0 & C \end{bmatrix} \bullet \begin{bmatrix} \dot{i}_{L1} \\ \dot{i}_{L2} \\ \dot{v}_{C1} \\ \dot{v}_{C2} \end{bmatrix} \\
&= \begin{bmatrix} -(r_L + r_C) & 0 & 0 & 1 \\ 0 & -(r_L + r_C) & 1 & 0 \\ 0 & -1 & 0 & 0 \\ -1 & 0 & 0 & C \end{bmatrix} \bullet \begin{bmatrix} i_{L1} \\ i_{L2} \\ v_{C1} \\ v_{C2} \end{bmatrix} + \begin{bmatrix} 1 & r_C \\ 0 & r_C \\ 0 & -1 \\ 0 & -1 \end{bmatrix} \bullet \begin{bmatrix} V_{in} \\ I_{Load} \end{bmatrix}
\end{aligned}
\tag{9}
$$

Using the state space average method [6–10], The DC side model of qZSI can be described as below:

$$
A = DA_1 + (1 - D)A_2 \quad \text{and} \quad B = DB_1 + (1 - D)B_2 \tag{10}
$$

Then we get:

$$A = \begin{bmatrix} -(r_L + r_C) & 0 & D-1 & D \\ 0 & -(r_L + r_C) & D & D-1 \\ 1-D & -D & 0 & 0 \\ -D & 1-D & 0 & C \end{bmatrix} \text{ and } B = \begin{bmatrix} 1 & (1-D)r_C \\ 0 & (1-D)r_C \\ 0 & D-1 \\ 0 & D-1 \end{bmatrix} \tag{11}$$

Which can be written as:

$$F\dot{x} = Ax + Bu \tag{12}$$

In the steady-state, the model becomes $Ax + Bu = 0$. From this expression, the values of the various quantities (V_{C1}, I_{L1}, …) of the operating point in steady-state can be determined [1, 3].

4 Small Signal Modeling

The elaboration and analysis of the small signal model of the qZSN is required to deduce the transfer functions relating to the various variables of the system [2–8]. The equivalent circuit of QZSI (Fig. 3) is still used to determine and analyze the QZSI small signal model. We will use the same state vector and the same equations determined in the previous section.

Modeling and studying the dynamic behavior of the converter is a prerequisite for designing its control system [2–8]. Notably, it is interesting to investigate how the output voltage is affected by fluctuations in the input voltage or load current. In fact, the state variable small signal relationship is derived by introducing perturbations $\hat{d}$,$\hat{v}_{in}$ and $\hat{i}_{load}$ to d, v_{in} and i_{Load}. This perturbation introduces a variation of $\hat{i}_{L1}$, $\hat{i}_{L2}$, $\hat{v}_{C1}$ and $\hat{v}_{C2}$ to the state variable i_{L1}, i_{L2}, v_{C1} and v_{C2}.

The above variations are represented in the form of $x = X + \hat{x}$, where X is the continuous terms and $\hat{x}$ are perturbations of variables $x = i_{Load}, v_{in}, d, i_{L1}, i_{L2}, v_{C1}$ and v_{C2}. the averaged model that depicts the dynamics of the network impedance is obtained by substituting $x = X + \hat{x}$ into Eq. (12), as follows:

$$\begin{aligned} F\frac{d}{dt}(\hat{x} + X) = &\left[A_1(\hat{d} + D) + A_2(1 - ((\hat{d} + D)))\right](\hat{x} + X) \\ &+ \left[B_1(\hat{d} + D) + B_2(1 - (\hat{d} + D))\right](\hat{u} + U) \end{aligned} \tag{13}$$

where: $\hat{u} = \left[\hat{v}_{in}\hat{i}_{load}\right]^T$ and $\hat{x} = \left[\hat{i}_{L1}\ \hat{i}_{L2}\ \hat{v}_{C1}\ \hat{v}_{C2}\right]^T$.

The development of Eq. (13) as in [12] leads to an equation containing 3 terms, the first is the DC component, the second is a linear AC term while the third is a non-linear term [11, 12].

The desired small signal model can be limited to the linear AC terms, the DC terms in both sides of the Eq. (13) are equal and considered known, the non-linear terms are smaller and can be neglected [11, 12].

Finally, the small signals model can be written as follows:

$$\begin{aligned} F\frac{d\hat{x}}{dt} &= [A_1D + A_2(1-D)]\hat{x} + [B_1D + B_2(1-D)]\hat{u} + (A_1 - A_2)X\hat{d} \\ &\quad + (B_1 - B_2)U\hat{d} \\ &= A\hat{x} + B\hat{u} + (A_1 - A_2)X\hat{d} + (B_1 - B_2)U\hat{d} \end{aligned} \tag{14}$$

By developing the Eq. (14) we get:

$$\begin{aligned} F\frac{d\hat{x}}{dt} &= \begin{bmatrix} -(r_L + r_C) & 0 & D-1 & D \\ 0 & -(r_L + r_C) & D & D-1 \\ 1-D & -D & 0 & 0 \\ -D & 1-D & 0 & C \end{bmatrix} \begin{bmatrix} \hat{i}_{L1} \\ \hat{i}_{L2} \\ \hat{v}_{C1} \\ \hat{v}_{C2} \end{bmatrix} \\ &\quad + \begin{bmatrix} 1 & (1-D)r_C \\ 0 & (1-D)r_C \\ 0 & D-1 \\ 0 & D-1 \end{bmatrix} \begin{bmatrix} \hat{v}_{in} \\ \hat{i}_{Load} \end{bmatrix} + \begin{bmatrix} V_{C1} + V_{C2} - r_C I_{Load} \\ V_{C1} + V_{C2} - r_C I_{Load} \\ -I_{L1} - I_{L2} + I_{Load} \\ -I_{L1} - I_{L2} + I_{Load} \end{bmatrix} \hat{d} \end{aligned} \tag{15}$$

By applying the Laplace transformation to (15), we have:

$$\begin{aligned} Ls\hat{i}_{L1}(s) &= -(r_L + r_C)\hat{i}_{L1}(s) + (D-1)\hat{v}_{C1}(s) + D\hat{v}_{C2}(s) + \hat{v}_{in}(s) \\ &\quad + (1-D)r_C\hat{i}_{Load}(s) + V_0\hat{d} \\ Ls\hat{i}_{L2}(s) &= -(r_L + r_C)\hat{i}_{L2}(s) + D\hat{v}_{C1}(s) + (D-1)\hat{v}_{C2}(s) + \hat{v}_{in}(s) \\ &\quad + (1-D)r_C\hat{i}_{Load}(s) + V_0\hat{d} \\ Cs\hat{v}_{C1}(s) &= (1-D)\hat{i}_{L1}(s) - D\hat{i}_{L2}(s) + (D-1)\hat{i}_{Load}(s) + I_0\hat{d} \\ Cs\hat{v}_{C2}(s) &= -D\hat{i}_{L1}(s) + (1-D)\hat{i}_{L2}(s) + (D-1)\hat{i}_{Load}(s) + I_0\hat{d} \end{aligned} \tag{16}$$

where: $V_0 = V_{C1} + V_{C2} - r_C I_{Load}$ and $I_0 = -I_{L1} - I_{L2} + I_{Load}$.

By using the flow graph on the Eq. (16) [1, 10], the Laplace transfer functions small signal of the multi-input multi-output qZSN as shown in Fig. 4 can be derived as given by Eq. (17) [1, 6–10]:

$$\begin{aligned} \hat{v}_{Ci}(s) &= G^{\hat{v}_{Ci}}_{\hat{v}_{in}}(s)\hat{v}_{in}(s) + G^{\hat{v}_{Ci}}_{\hat{i}_{Load}}(s)\hat{i}_{Load}(s) + G^{\hat{v}_{Ci}}_{\hat{d}}(s)\hat{d} \\ \hat{i}_{Li}(s) &= G^{\hat{i}_{Li}}_{\hat{v}_{in}}(s)\hat{v}_{in}(s) + G^{\hat{i}_{Li}}_{\hat{i}_{Load}}(s)\hat{i}_{Load}(s) + G^{\hat{i}_{Li}}_{\hat{d}}(s)\hat{d} \quad with \quad i = 1, 2 \end{aligned} \tag{17}$$

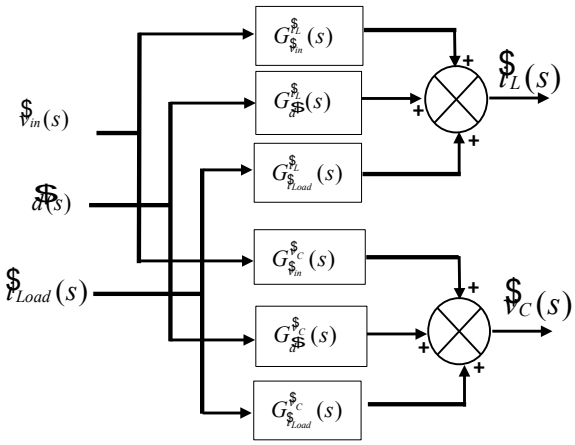

Fig. 4 qZSI small signal model

Each small signal transfer function for the $\hat{v}_{Ci}(s)$ and $\hat{i}_{Li}(s)$ to the $\hat{v}_{in}(s)$, $\hat{i}_{Load}(s)$ *and* $\hat{d}$ is obtained by assuming the other two inputs to be zero.

The transfer functions from the duty ratio $\hat{d}$ to $\hat{i}_{L1}$ and $\hat{i}_{L2}$ are identical, as $G_{\hat{d}}^{\hat{i}_L}(s)$ and the transfer function from $\hat{d}$ to $\hat{v}_{C1}$ and $\hat{v}_{C2}$ are also identical, as $G_{\hat{d}}^{\hat{v}_C}(s)$. The most commonly used detailed transfer functions can be obtained as follows [1, 2, 4, 6, 9, 10]:

$$G_{\hat{d}}^{\hat{v}_C}(s) = \frac{I_0(Ls + r_L + r_C) + (1-2D)V_0}{LCs^2 + C(r_L + r_C)s + (1-2D)^2} \tag{18}$$

$$G_{\hat{d}}^{\hat{i}_L}(s) = \frac{V_0 Cs - (1-2D)I_0}{LCs^2 + C(r_L + r_C)s + (1-2D)^2} \tag{19}$$

The transfer functions $G_{\hat{d}}^{\hat{v}_C}(s)$ and $G_{\hat{d}}^{\hat{i}_L}(s)$ are usually used for the capacitor voltage and inverter output current control [1, 2, 6, 9, 11]. The small-signal models can be taken to explore the dynamics of qZS network under system parameter variations. Considering the variation of the inductance L, capacitance C, equivalent resistance r_L, r_C, and ST duty ratio D.

5 Dynamic Analysis of qZSI Model

The small signal model developed could be interesting to preview the dynamic behavior of the QZSI as the parameters change. Considering the variation of the inductance L, capacitance C, equivalent resistance r_L, r_C, and ST duty ratio D. the study of the location of the roots and poles of the system can provide interesting information on the dynamics of the system. In order to design the system control

loops with adequate phase margins, the system dynamics must be predicted. the most important transfer function to design the control system is the one from the duty ratio $\hat{d}$ to the capacitor voltage $\hat{v}_{C1}$ [2–6, 9, 10, 13, 14].

According to the above Eq. (18), the characteristic equation of the QZSN can be defined as follows:

$$LCs^2 + C(r_L + r_C)s + (1-2D)^2 = 0 \quad \Rightarrow \quad s^2 + \frac{(r_L + r_C)s}{L} + \frac{(1-2D)^2}{LC} = 0 \tag{20}$$

Equation (20) may be written in the following standard form:

$$s^2 + 2z\omega_n s + \omega_n^2 = 0 \text{ where } \omega_n = \frac{1-2D}{\sqrt{LC}} \text{ and } z = \frac{r_L + r_C}{1-2D}\sqrt{\frac{C}{L}}) \tag{21}$$

z is the damping ratio and ω_n is the natural pulsation (frequency).

From the above equation, we can deduce that the parameters of the impedance network (L, C, r_L and r_C), and the duty ratio D are factors that determine the system dynamic characteristics.

To get a clear idea of the dynamics of the impedance network, various locations of the poles and zeros of the transfer function $G_{\hat{d}}^{\hat{v}_C}(s)$ are studied by varying the parameters L, C and D. The values of the various system parameters are given in the following table [7] (Table 1).

Figure 5 shows Pole-zero map, bode diagrams, and step responses of $G_{\hat{d}}^{\hat{v}_C}(s)$ with varying the parameters of the impedance network. The non-minimum phase (NMP) undershoot is indicated by the presence of right half-plane roots (RHP) in the transfer functions. When the ST duty ratio increases, the dynamic capacitor voltage will drop first, and then it will continue to rise [1–6, 10, 13, 14].

Figure 4a, b shows the pole-zeros map and bode diagram when L varies, When L increases, the degree of the NMP undershoot and the settling time also increases. With the increase of C, the impact on the NMP undershoot is negligible, while the settling time rises, as shown in Fig. 4c, d. Large values of L and C lead to small ripples in the steady-state but will also slow down the transient response.

From Fig. 5e, it can be seen that when the value of L is larger, the overshoot of the step response is important, and the settling time is longer. From Fig. 5f, it can be seen that when C increases, the overshoot decreases but the rise time becomes

Table 1 Parameters of the qZSI for model verification

Parameters	Values	Parameters	Values
L	500μH	r_L	0.47Ω
C	400μF	r_C	0.03Ω
D	0.25	I_{Load}	9.9 A
V_{in}	130 V		

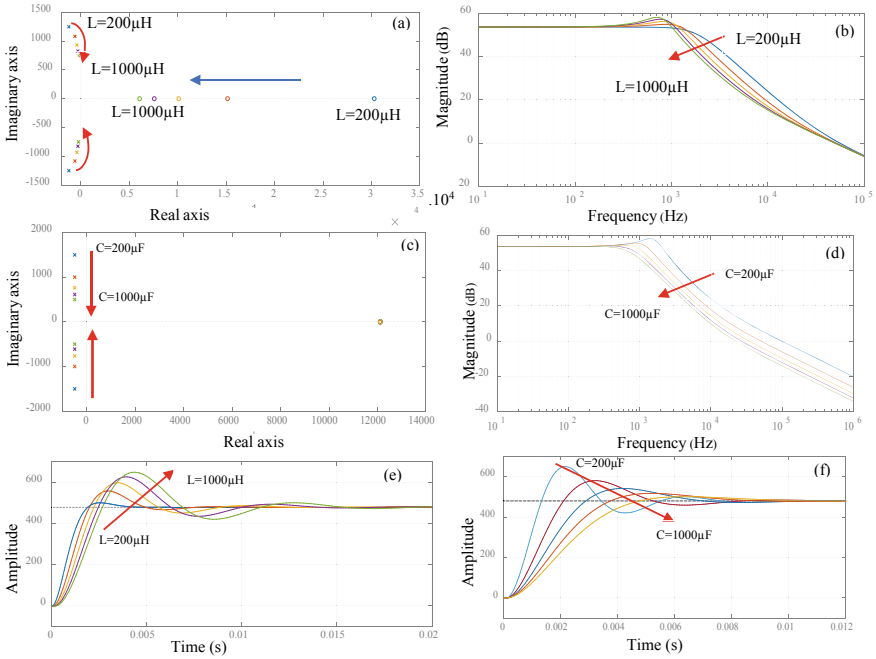

Fig. 5 **a** Zero-pole trajectory, **b** Bode diagram, inductance changing; **c** Zero-pole trajectory, **d** Bode diagram capacitance changing; **e** Step response inductance changing; **f** Step response capacitance changing

longer. Thus, the results in the time domain are in coherence with the frequency domain analysis.

The impact of other parameters on the dynamic behavior of qZSN can be determined in a similar way. For duty cycle D, increasing the shoot-through duty ratio D leads to an increase in the degree of the NMP undershoot. We can also demonstrate that the settling time varies in the same way as D.

Furthermore, with respect to the equivalent resistances of the passive components, the increase of the resistances r_L or r_C will increase the degree of the NMP undershoot and system damping ratio simultaneously.

6 Conclusion

This paper focuses on the study of impedance network converters, especially QZSI which is currently very used in the PV systems grid-connected, due to continuous input current and other several advantages when compared to the conventional ZSI. The detailed mathematical of the steady-state model and the small signal of qZSI are presented. The state-space averaging method is used to derive the transfer functions.

By a small signal model analysis, the dynamic characteristics of the QZSN have been investigated. A detailed analysis of the dynamic characteristics as a under parameters variations of the qZSN has also been reported. The dynamics of the transfer functions and the behavior of the dynamic converter will be used to design the qZSI system and controller design.

References

1. Liu, Y., Abu-Rub, H., Ge, B., et al.: Impedance source power electronic converters. Wiley (2016)
2. Peng, F.Z.: Z-source inverter. IEEE Trans. Ind. Appl. **39**, 504–510 (2003)
3. Siwakoti, Y.P., Peng, F.Z., Blaabjerg, F., et al.: Impedance-source networks for electric power conversion part I: a topological review. IEEE Trans. Power Electron. **30**, 699–716 (2014)
4. Badin, R., Huang, Y., Peng, F.Z., Kim, H.-G.: Grid interconnected Z-source PV system. In: 2007 IEEE Power Electronics Specialists Conference, pp. 2328–2333. IEEE (2007)
5. Anderson, J., Peng, F.Z.: A class of quasi-Z-source inverters. In: 2008 IEEE Industry Applications Society Annual Meeting, pp. 1–7. IEEE (2008)
6. Liu, W., Yuan, J., Yang, Y., Kerekes, T.: Modeling and control of single-phase quasi-Z-source inverters. In: IECON 2018–44th Annual Conference of the IEEE Industrial Electronics Society, pp. 3737–3742. IEEE (2018)
7. Li, Y., Peng, F.Z., Cintron-Rivera, J.G., Jiang, S.: Controller design for quasi-Z-source inverter in photovoltaic systems. In: 2010 IEEE Energy Conversion Congress and Exposition, pp. 3187–3194. IEEE (2010)
8. AsSakka, A.O., ElShahed, M.A., Hassan, M.A.M., Senjyu, T.: Modeling and control of a PV based QZSI for grid connected applications. In: 2017 International Conference on Control, Automation and Information Sciences (ICCAIS), pp. 67–72. IEEE (2017)
9. Li, Y., Jiang, S., Cintron-Rivera, J.G., Peng, F.Z.: Modeling and control of quasi-Z-source inverter for distributed generation applications. IEEE Trans. Industr. Electron. **60**, 1532–1541 (2012)
10. Liu, Y., Ge, B., Ferreira, F.J.T.E., et al.: Modeling and SVPWM control of quasi-Z-source inverter. In: 11th International Conference on Electrical Power Quality and Utilisation, pp. 1–7. IEEE (2011)
11. Elbaset, A.A., Hassan, M.S.: Small-Signal MATLAB/Simulink Model of DC–DC Buck Converter. In: Design and Power Quality Improvement of Photovoltaic Power System, pp. 97–114. Springer (2017)
12. Silva, J.F., Pinto, S.F., Rashid, M.H.: Control methods for switching power converters. In: Power electronics handbook, pp. 935–998. Academic (2007)
13. Lannert, T., Isen, M., Braun, M.: Small signal modeling of the quasi-Z-source-inverter and a novel control strategy to minimize the influence of input voltage disturbances. In: 2013 15th European Conference on Power Electronics and Applications (EPE), pp. 1–10. IEEE (2013)
14. Liu, W., Pan, Y., Yang, Y.: Small-signal modeling and dynamic analysis of the quasi-Z-source converter. In: IECON 2019–45th Annual Conference of the IEEE Industrial Electronics Society, pp. 5039–5044. IEEE (2019)

Modeling and Control of a PFC Forward Converter with Linear Control for Charging the Urban Cars

Mohamed Arrach, Khalid Chikh, and Abdesslam Lokriti

Abstract This paper describes an electrical urban car on board charger, which is considered as a new challenge of the mobility market. The main goal of this research paper, is to model and control, under Matlab/Simulink, an isolated forward topology fed by single phase source, with power factor correction (PFC) technique, to charge the urban car battery. It discusses the modeling of PFC forward converter as an onboard charger, started by definition of the keys characteristics in term of power stage, control strategy and input power quality. To achieve this goal, a power stage is designed referring to specifications of power charger, a PFC technique is used to keep high input power quality, and a small ac signal analysis is established to determine the closed-loop control parameters using constant current and constant voltage technique to charge the battery of the urban car.

Keywords Forward converter · PFC technique · Li-ion battery · Linear control · Hysteresis control · Urban cars

1 Introduction

With ever increasing concerns on environmental issues and clean energy, electric vehicles (EVs) have attracted more and more attention of governments, industries, and customers. EVs are popularly regarded as one of the most effective strategies to reduce the oil dependence and gas emission, and increase the efficiency of energy conversion [1]. Now, the car market is fermenting a revolution, and the trigger is all kinds

M. Arrach (✉) · K. Chikh · A. Lokriti
LASTI Laboratory of ENSA Khouribga, Sultan Moulay Slimane University of Beni Mellal, Beni Mellal, Morocco
e-mail: mohamed.arrach@usms.ac.ma

K. Chikh
e-mail: Khalid.chikh@usms.ac.ma

A. Lokriti
e-mail: abdesslam.lokriti@usms.ac.ma

M. Bendaoud et al. (eds.), *The Proceedings of the International Conference on Electrical Systems & Automation*, https://doi.org/10.1007/978-981-19-0039-6_9

of Electric vehicles (EVs) [2]. Due to their lower maintenance costs, lower ownership costs, noise reduction, and charging at home and work and around the community are some of the additional advantages of using EVs [3]. Moreover, the main objectives for a sustainable development of cities are identified as: construction of green areas, urban and environmental regeneration, compact urban planning, accessibility to all the areas of the city, sustainable and interconnected transport, development of pedestrian and cycle zones to encourage the spread of non-motorized mobility throughout the urban area [4]. So, to respond to sustainable mobility, Morocco government is signed, with *Stellantis Group* in the October, 19th 2019, the agreement to provide a 225 units of a special series of the small electric vehicle called *Citroen AMI* limited to 45 km/h speed. This urban car is specially adapted to the workers mission of the Moroccan post "*Barid Almaghreb*". Thus, such initiative could inspire other transportation companies in the Moroccan country.

2 System Overview

2.1 Presentation of the Vehicle

The *Citroen AMI*, in Fig. 1, is a urban car with a two-passenger, with no licence car agreement, urban car with an autonomy up to 70 km and a nominal battery capacity of 5.5 kWh. It was developed by the French manufacturer "Stellantis", produced in the beginning of 2020 and marketed below June 2020. Its main technical specifications, from "Stellantis" internet site, are mentioned in Table 1.

Table 1 Main specifications data of citroen AMI

Main technical data of Citroen Ami	
Engine power	6 kW
Battery capacity	5.5 kWh
Charging time on a domestic socket	3 hours under 1.8kW
Autonomy (WLTP cycle)	75 km
Weight	471 kg (with battery)
Speed	45 km / h

Fig. 1 Citroen AMI car

2.2 Charging Levels Techniques Literature

Battery chargers play a crucial role to keep the battery in its optimal state of health. Two power transfer methods to the battery are possibles: conductive or inductive. The Conductive chargers use metal-to-metal contact as in most appliances and electronic devices while the inductive charging of EVs is based on magnetic contact less power transfer [5]. The location of the battery charger depends of its power level. Two types of battery are existing: on-board charger and off-board charger. The on-board type, delivering AC voltage, to allow its owner to charge his vehicle everywhere once a suitable AC power source is available. Typical on-board chargers limit the power because of weight, space, and cost constraints and are dedicated to charge the battery for a long period of time [6] which is usually compatible with level "one" and level "two" chargers up to 23 kW. Otherwise, applications in commercial and public domains preferably used Level 3 and DC fast charging [7]. It typically operates with a high power three phase circuit and requires a multiple stage conversion to provide the required DC current. Therefore, a dedicated low frequency medium voltage (MV) to low voltage (LV) transformer is used to supply three-phase power to EV fast-charging stations, minimize the distribution network, and provide galvanic isolation [8].

2.3 Overview of the Proposed Topology

This paper aims to propose an isolated topology based on forward converter fed by single phase source, with PFC technique, to charge the car battery and meet the isolation criteria between input source and the battery load which is guaranteed by the high frequency transformer T_1 mentioned in Fig. 2.

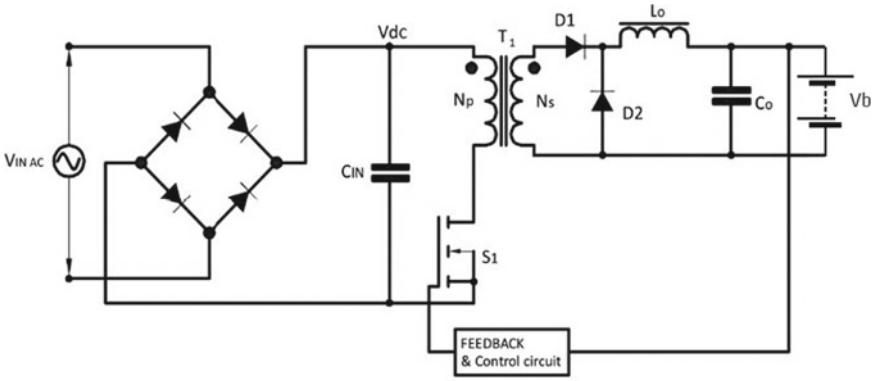

Fig. 2 Proposed schematic of forward battery charger

2.4 Battery Charging Algorithm

Although Li-ion batteries are preferred over other battery technologies for their lightweight, high energy storage, low charge loss, no requirements of complete discharge, and a great amount of charge and discharge cycles [10]. Lithium-ion batteries must be operated in a safe and reliable operating area, which is affected by the charge rate, temperature and voltage range [11]. In order to charge lithium-ion batteries, constant current (CC)/constant voltage (CV) is often adopted for high-efficiency charging and sufficient protection [12]. This method consists of two phases. In the first phase the battery is charged with constant current, while the voltage across the battery gradually increases [13]. Once, the battery reaches its nominal value, the current begins slowly to decay until full charge as mentioned in the Fig. 3.

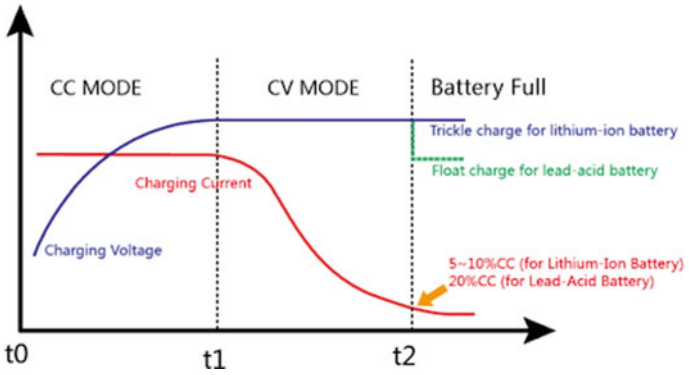

Fig. 3 Schematic of CC–CV algorithm

3 Power Stage Design Parameters

This paper adopts forward converter because of the simple structure and high efficiency [14]. The forward topology is derived from the buck topology. With a single transistor used, forward converter employs also a high frequency transformer to ensure a galvanic isolation between input and output voltage, which makes it a good choice for this application.

3.1 Duty Cycle Calculation

The first step to calculate the switch current is to determine the duty cycle, D, for the maximum input voltage. The maximum input voltage is used because this leads to the maximum switch current. Calculation of the duty cycle in forward topology is given by the following Eq. (1):

$$D = \frac{V_{out}}{V_{int}} \tag{1}$$

3.2 HF-Transformer Design

Power transformers have been researched for more than a century and their design, optimization and material problems have been investigated extensively for sinusoidal voltage application as well as square wave voltage application [15]. The selection of this component must be defined carefully to do not reach the saturation of its magnetic core. The winding ratio between the primary winding and the secondary winding must be chosen in order to satisfy the previous condition of saturation.

3.3 Inductor Design

The selection of the right value of inductor is an important issue to guarantee a good current profile and get the desired output power. The inductor must have a minimum possible of series resistance to limit the power dissipation in the converter to meet a good efficiency. The value of the inductor depends of the switching frequency, desired current ripple, input and output voltage as given by Eq. (2):

$$L0 = \frac{V_{out} \times (V_{in} - V_{out})}{\Delta I_{L0} \times f_s \times V_{in}} \tag{2}$$

where:

V_{in} : Input voltage in (V);
f_s : Switching frequency in (Hz);
V_{out} : Output Voltage in (V);
ΔI_{L0} : Ripple current in (A).

4 Design of Control Loops Parameters

4.1 Design of PFC AC–DC Rectifier Control

The battery charger for this high-voltage battery controls the converter according to the charging profile of the battery and has two stages [16]. The first stage is a PFC boost converter used to limit the total harmonic distortion of input current to meet the high power quality ratio minimum limit and keep maintain the voltage across to the input of the second stage DC-DC converter while the second. As mentioned in Fig. 4, to make the input current follows the input voltage, the reference signal of the output voltage, of PFC converter, is compared with sensed voltage in the DC bus V_o, and then controlled through voltage block A_v. The output of A_V is multiplied by the absolute value of input voltage by its RMS value $|Vg|$. Afterward, the output of the multiplier is compared to the sensed inductor current to pass through the current loop A_i error amplifier. The amplified error signal is the input for the pulse width modulator, adjusting the power switch duty ratio so as to minimize the error between the reference and the sensed inductor current while the "gate driver" is a hysteresis block commands the main switch S1.

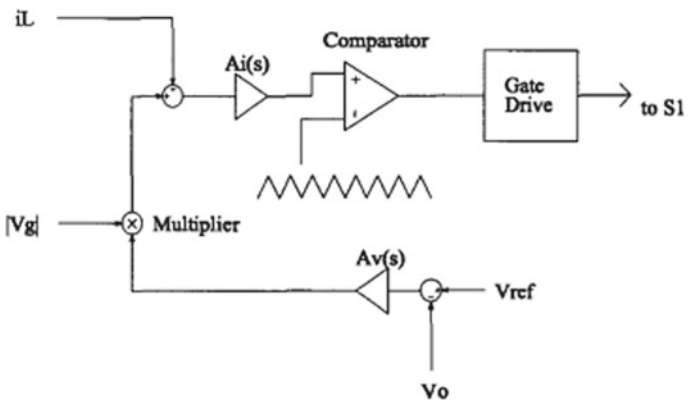

Fig. 4 Conventional pfc control circuit [9]

4.2 Design of DC–DC Converter Control

To make a closed loop of the power stage and design the control parameters, a small ac signal ac analysis is performed works under continuous conduction mode (CCM). The control strategy, as given in Fig. 5, is based on two loops: inner current loop and outer voltage loop. The inner current loop maintain The constant current (CC) until reaching the nominal voltage value across the battery. While The outer voltage loop maintains the nominal voltage, with a decay of current, across the battery terminals until the full charge. Transition between the two modes is automatic. If the battery voltage is below CV reference, the converter is in CC mode. Once the battery voltage reaches the CV reference, the converter operates in CV mode until the current goes to zero [17].

The transfer functions of the both inner and outer loops are calculated based on the ac small signal analysis equivalent circuit. To control the converter, the desired crossover frequency and phase margin criteria are already known, based the switching frequency value to meet stability and damping ratio requirements. The outer voltage loop should determine the reference of the inductor current which is compared to the sensed value of the inductor. While the inner current loop control the output current. To determine the parameters of the two blocks we should set the crossover frequency and make sure the phase margin does not exceed the standard. For the current control loop was set to 2 kHz, and one-tenth 200 Hz should be the crossover frequency for the voltage control loop. The following Eqs. (3), (4) and (5) are the transfer functions of the equivalent circuit of forward converter after ac small signal analysis:

$$T_{vi} = \frac{1}{R_f} * \times \frac{T_{vd}}{T_{id}} \tag{3}$$

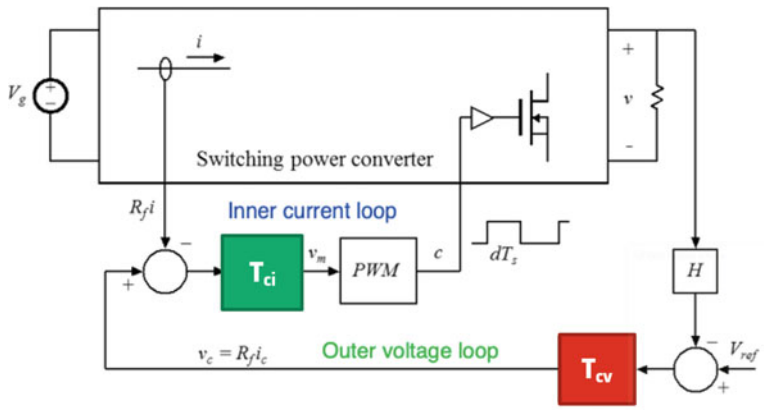

Fig. 5 Schematic of forward closed control loops

where:

R_f : Sensing current resistor;
T_{vd} : Control to output transfer function;
T_{id} : Control to current transfer function;
T_{vi} : Voltage to current transfer function;

$$T_{vd} = T_{vd_0} \frac{1}{1 + s.L/r} \tag{4}$$

where $T_{vd_0} = \frac{V_{out}}{D}$

$$T_{id} = T_{id_0} \frac{1}{1 + s.L/r} \tag{5}$$

where $T_{id_0} = \frac{V_{out}}{D.r}$

The key parameters of the two PI blocks are given in the following Eqs. (6) and (7):

$$T_{ci} = T_{cm}(1 + \omega_z/s) \tag{6}$$

$$T_{cv} = T_{vm}(1 + \omega_z/s) \tag{7}$$

where:

T_{cv} : Outer voltage loop control.
T_{ci} : Inner current loop control.
T_{cm} : Its refers to the static gain of current loop K_{p_1}.
$T vm$: The proportional gain of voltage loop K_{p_2}.
ω_z/s The inverted zero (integral gain) to push frequency response to the desired crossover frequency K_i.

To determine the control parameters of the two loops, a small signal analysis of the converter was established. The static gain values of the control loops is obtained with Eqs. (6) and (7) while the integrator gain of is taken as the third of the static gain.

5 Simulation Results and Discussion

To simulate the behavior of our proposed PFC forward converter, a Matlab/Simulink model is designed and controlled with hysteresis control, with a band of 0:1, in AC/DC PFC rectifier stage and linear control in the forward DC-DC converter as shown in Fig. 6. The first stage is connected to single phase grid under 220 Volts followed by forward converter of 1:8 kW which feeds a battery of 48 V with a capacity of 115 Ah. The specification design of the power stage and control parameters are given respectively in Tables 2 and 3.

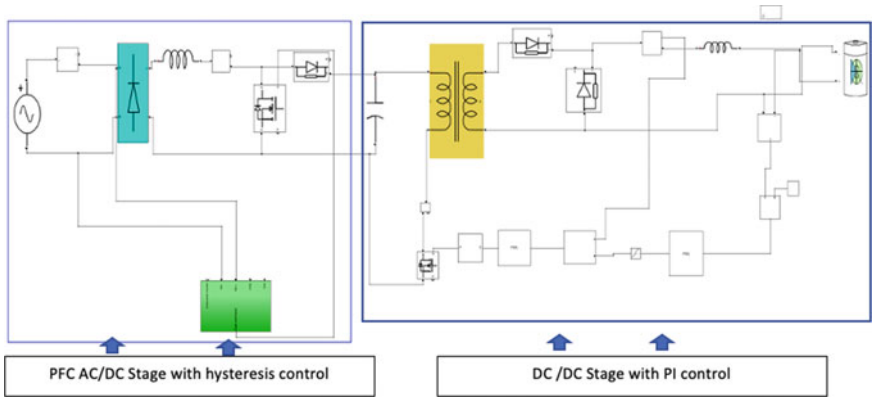

Fig. 6 Simulink model of the proposed charger

Table 2 Simulation parameters of PFC forward converter

Name	Parameter	Value	Unit
Input voltage 1-phase	V_{in_1}	220	V
Output voltage	V_{out}	48	V
Output current	I_{out_1}	38	A
Output power	P_1	1.8	kW
Inductor	L_1	9.5	mH
Sensing resistor	R_f	1	Ω
ESR of inductor	r	50	$m\Omega$
Switching frequency	f_s	20	kHz
Ripple current	ΔI_L	10	%
Duty cycle	D_1	20	%

Table 3 Key parameters of control blocks

Name	Parameter	Value
Proportional gain current loop	K_{p_1}	0.55
Integrator gain current loop	K_{i_1}	0.18
Proportional gain voltage loop	K_{p_2}	11.76
Integrator gain voltage loop	K_{i_2}	3.92
Sensing current	R_f	1
Sensing voltage	H	1

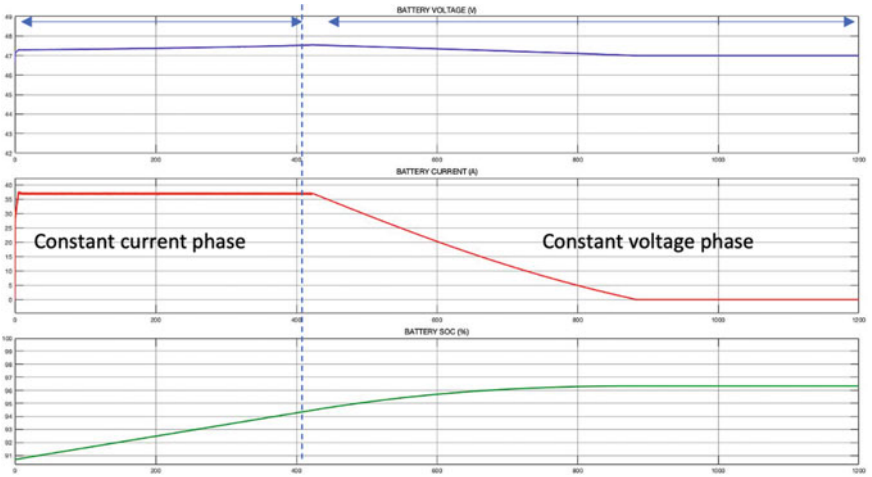

Fig. 7 Profile simulation response of battery PFC forward converter

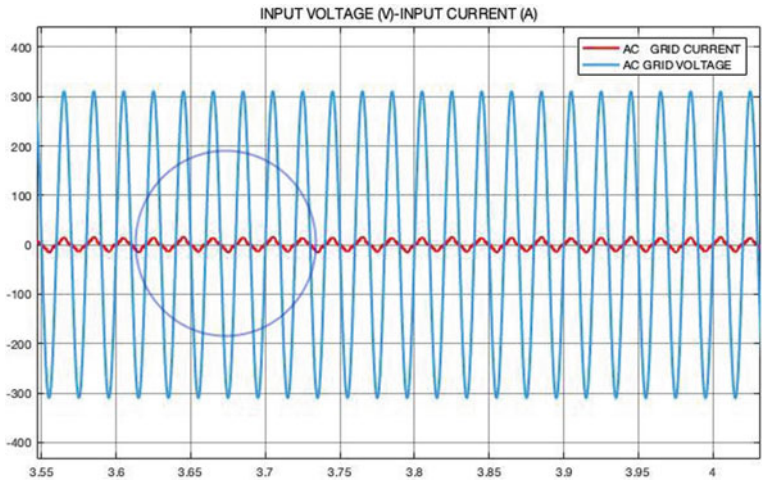

Fig. 8 Power factor correction of the AC–DC stage

As given in the model Fig. 7, the battery of 115 Ah, fed by 1.8 kW with initial state of charge at 90%. We can observe that "constant current-constant voltage" algorithm works as excepted with "CC mode" from 0 minutes until 6, 5 min with a state of charge of 95% with a maintained constant current and constant voltage mode in the last 3, 5 min with good performance in dynamic response and terms of transition between CC mode and CV mode.

We can observe also, that the PFC technique works as expected with a good phase leg and good shape of input current as illustrated in Fig. 8.

6 Conclusion

In this work paper, a PFC forward converter with hysteresis and PI control is designed and simulated, to charge, citroen ami, the urban cars with a power of 1.8 kW under single phase. We have designed the whole charger based of forward converter with PFC technique, applied to AC/DC rectifier, to meet high power factor quality between input current and input voltage. The PFC rectifier stage was obtained using hysteresis control while the linear control was used for the forward DC/DC converter stage, with two loops, using the constant current and constant voltage algorithm. In the previous results, we have note that the proposed charger works as expected in term of control dynamic response, expected nominal power, and input power quality. Thus, this charger can be recommended for all urban electrical vehicles, with Li-ion battery, under single phase source.

References

1. Chan, C.C.: The state of the art of electric, hybrid, and fuel cell vehicles. Proc. IEEE **95**(4), 704–718 (2007)
2. Liu, C., Chau, K.T., Wu, D., Gao, S.: Opportunities and challenges of vehicle-to-home, vehicle-to-vehicle, and vehicle-to-grid technologies. Proc. IEEE **101**(11), 2409–2427 (2013)
3. Lutsey, N., Searle, S., Chambliss, S., Bandivadekar, A.: Assessment of leading electric vehicle promotion activities in united states cities. In: International Council Clean Transportation, Washington, DC, USA, Technical Report (2015)
4. Consilvio, A., Di Febbraro, A., Sacco, N., Torre, A.: On exploring the potentialities of autonomous vehicles in urban spatial planning. In: 2019 6th International Conference on Models and Technologies for Intelligent Transportation Systems (MT-ITS), pp. 1–7 (2019)
5. Hayes, J.G., Egan, M., Murphy, J.D., Schulz, S., Hall, J.: Wide load resonant converter supplying the SAE J-1773 electric vehicle inductive charging interface. IEEE Trans. Ind. Appl. **35**(4), 884–895 (1999)
6. Haghbin, S., Khan, K., Lundmark, S., Alaküla, M., Carlson, O., Leksell, M., Wallmark, O.: Integrated Chargers for EV's and PHEV's: examples and new solutions. In: Proceeding of International Conference Electrical Machines (ICEM) (2010)
7. Habib, S., Khan, M.M., Hashmi, K., Ali, M., Tang, H.: A comparative study of electric vehicles concerning charging infrastructure and power levels. In: International Conference on Frontiers of Information Technology (FIT) **2017**, 327–332 (2017)
8. Tahir, Y., et al.: A state-of-the-art review on topologies and control techniques of solid-state transformers for electric vehicle extreme fast charging. IET Power Electron. **14**, 1560–1576 (2021)
9. Tanitteerapan, T., Mori, S.: An input current shaping technique for PFC flyback rectifier by using inductor voltage detection control method. In: Proceedings of IEEE Region 10 International Conference on Electrical and Electronic Technology. TENCON 2001 (Cat. No.01CH37239), vol. 2 (2001), pp. 799–803
10. Oswal, M., Paul, J., Zhao, R.: A Comparative Study of Lithium-Ion Batteries. Univ. Southen California, Los Angeles, CA, USA (2010)
11. Chen, W., Liang, J., Yang, Z., Li, G.: A review of Lithium-Ion battery for electric vehicle applications and beyond. Energy Proc. **158**, 4363–4368 (2019). ISSN 1876-6102
12. Vu, V., Tran, D., Choi, W.: Implementation of the constant current and constant voltage charge of inductive power transfer systems with the double-sided LCC compensation topology for

electric vehicle battery charge applications. IEEE Trans. Power Electron. **33**(9), 7398–7410 (2018)
13. Gücin, T.N., Biberoğlu, M., Fincan, B.: A constant-current constant-voltage charging based control and design approach for the parallel resonant converter. In: 2015 International Conference on Renewable Energy Research and Applications (ICRERA), pp. 414–419 (2015). https://doi.org/10.1109/ICRERA.2015.7418447
14. Sun, J., Rengui, L., Wei, G., Bingliang, X., Zhu, C.: A high efficiency equalizer based on forward converter for series connected battery string. IEEE Veh. Power Propuls. Conf. **2012**, 376–379 (2012)
15. Agarwal, R., Martin, S., Shi, Y., Li, H.: High frequency transformer design for medium voltage shipboard DC-DC converter. IEEE Electr. Ship Technol. Sympos. (ESTS) **2019**, 499–504 (2019)
16. Das, P., Pahlevaninezhad, M., Drobnik, J., Moschopoulos, G., Jain, P.K.: A nonlinear controller based on a discrete energy function for an AC/DC boost PFC converter. IEEE Trans. Power Electron. **28**(12), 5458–5476 (2013). https://doi.org/10.1109/TPEL.2012.2232681
17. Mohamed, A., Khalid, C., Abdesslam, L.: Modeling and control of a synchronous buck converter fed by single phase system for charging the Urban electrical vehicles. IEEE PES/IAS PowerAfrica **2021**, 1–5 (2021)
18. Ayachit, A., Kazimierczuk, M.K.: Averaged small-signal model of PWM DC-DC converters in CCM including switching power loss. IEEE Trans. Circ. Syst. II: Express Briefs **66**(2), 262–266 (2019)
19. Singh, B., Chaturvedi, G.D.: Comparative performance of isolated forward and flyback AC–DC converters for low power applications. Joint Int. Conf. Power Syst. Technol. IEEE Power India Conf. **2008**, 1–6 (2008)

Vehicle Performance and Wheel Load Analysis for Electric Traction Motors Sizing

Amine El Houre, Mohammed Chaker, Driss Yousfi, and Zakaria Bourzouk

Abstract In this paper, a sizing method for an electric vehicle's traction motor is presented and discussed. The method is based on vehicle performance and wheel load analysis on different road loads. The motor ratings are investigated and selected by evaluating road driving conditions obtained from ECE15 drive cycle, acceleration performance, gradeability and maximum speed. This study is conducted using a realized simulation model in Matlab/Simulink. The sized and the selected motor is integrated into a developed test bench for evaluation and validation.

Keywords Electric vehicle · Traction motor · Sizing · Drive cycle · Matlab/Simulink

1 Introduction

Today's global energy demand has increased dramatically as a result of rapid population growth and technological progress. Indeed, transport is a major contributor to the world's rise in energy use [1]. Due to this rise, the world community is deeply concerned about the depletion of fossil fuel reserves and the environmental adverse effects of road transport related to toxic emissions and greenhouse gases. This has resulted in a peaked vehicle electrification interest, mainly hybrid electric vehicles (HEVs) and battery electric vehicles (BEVs) [2]. Because BEVs have a high drivetrain efficiency and do not release exhaust emissions, they have been classified as CO_2 neutral under legislation up to this day [3]. To respond to the rapid increase of vehicle electrification, the sizing of the electric powertrain components is necessary. Generally, these components are: the electric traction motor, battery and converters.

A. El Houre (✉) · M. Chaker · D. Yousfi
ESETI Laboratory, National School of Applied Sciences, Mohamed First University, Oujda, Morocco

Z. Bourzouk
Capgemini Engineering, Casablanca, Morocco

M. Bendaoud et al. (eds.), *The Proceedings of the International Conference on Electrical Systems & Automation*, https://doi.org/10.1007/978-981-19-0039-6_10

Speaking of the electrical machines, they are selected based on the vehicle performance and loads requirements in addition to high power density, efficiency and cost [4–6].

The vehicle's driving performance is often assessed by its acceleration performance, maximum speed, and road gradeability [7]. To obtain the performance criteria without excessive motor ratings, the traction machine is designed based on power and torque versus speed characteristics and expected road conditions. The road driving conditions are mostly evaluated using the drive cycle method, which describes highway, urban or rural driving [8, 9].

In this paper, a sizing method for an electric vehicle traction motor is proposed.

The method consists of evaluating the motor's requirements from the vehicle's main specifications and characteristics. The motor should be able to handle a certain acceleration performance, gradeability, and top speed. Also, it should deliver power, torque and speed needs on road driving conditions similar to those of the ECE 15 drive cycle. The sized traction motor was validated using a test bench with the help of an automated measurement platform and a LabVIEW graphical user interface [9]. The main distinguishing feature of this work, in comparison to others [10, 11], is the integration of the sized motor into the test bench for validation.

2 Vehicle Dynamics Equations

A basic understanding of vehicle dynamics is crucial during the powertrain design process since it indicates the resistive load that the powertrain must deal with when driving.

To model the vehicle dynamics for the purpose of power and load analysis, the vehicle is treated as a rigid mass concentrated on its center of gravity [12]. The vehicle is considered stable, leaving us only with the dynamics in the longitudinal forward direction. In all cases, the forces that interact with the vehicle in this direction are: the aerodynamic resistance F_a, the rolling resistance F_r, the grading force F_g and, the acceleration force F_{acc}.

By exploiting Newton's second law, we can write:

$$F_D = F_a + F_r + F_g + F_{acc} = \frac{1}{2}\rho C A (V - Vw)^2 + Mgfr\cos\alpha + Mg\sin\alpha + M\frac{\mathrm{d}V}{\mathrm{d}t} \quad (1)$$

where F_D is the tractive force needed to drive the vehicle, ρ is the mass density of air (Kg/m^3), C the aerodynamic drag coefficient, A (m^2) is the frontal area of the vehicle, V (m/s) is the vehicle speed, Vw (m/s) is the component of wind speed, M is the vehicle mass (Kg), g is the gravity constant (m/s^2), fr is the rolling resistance coefficient, α is the road inclination angle and t is time (s).

Table 1 Electric vehicle main specifications

Quantity	Value
Radius of wheels (m)	0.25
Vehicle front area (m^2)	2.3
Air density (kg/m^3)	1.225
Aerodynamic drag coefficient	0.5
Rolling resistance coefficient	0.015
Vehicle mass (kg)	600
Overall gear ratio	7.6:1
Gear efficiency	100%
Maximum vehicle speed (km/h)	50
Drive cycle	ECE-15

The torque T_{wheel} needed on the wheel to drive the vehicle can be deducted using the following equation:

$$T_{wheel} = F_D \times R \tag{2}$$

where R is the wheel radius (m).

In our study and analysis, we will focus on a three wheeled light vehicle dedicated to urban areas with a single speed gearbox. Table 1 shows the vehicle main specifications.

3 Vehicle Performance and Wheel Load Analysis

Knowledge of the usage phase is necessary for a good vehicle design. Vehicles are utilized in a variety of settings in different conditions. These conditions impose various requirements on the vehicle for static and dynamic road loads.

Vehicle performance often comprises acceleration performance, which is measured by the time required to accelerate the vehicle from zero to a certain speed, gradeability, which is measured by the maximum road grade that the vehicle can overcome at a given speed, and the vehicle maximum speed [7]. However, these performances don't give enough information regarding real life driving situations [13], which is why methods to emulate road loads were developed. One of the best known techniques to emulate road loads is the drive cycle method. It was devised to represent driving conditions in several environments.

In this section, vehicle performance and wheel load is analyzed based on the electric vehicle specifications in Table 1.

3.1 Drive Cycle Based Analysis

Drive cycles were developed to emulate road driving conditions of a vehicle for several road types, such as urban, rural, or highway driving [14]. In our case, the vehicle is supposed to be driven on an urban road according to the ECE-15 drive cycle shown in Fig. 1.

The drive cycle is characterized by a vehicle top speed of 50 km/h and a maximum vehicle acceleration of 1.042 m/s^2.

By exploiting the Eqs. (1) and (2), a MATLAB/Simulink model was realized as seen in Fig. 2.

The discrete drive cycle bloc produces speed and acceleration performance according to the ECE-15 drive cycle. The vehicle dynamics bloc receives the speed and acceleration references and outputs the speed and torque needed on the wheel. Finally, the gearbox model converts the wheel requirements into motor requirements.

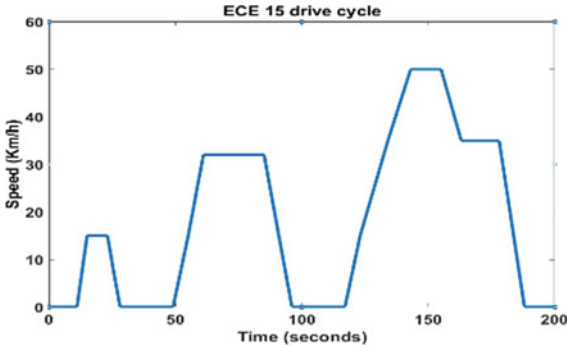

Fig. 1 ECE 15 drive cycle

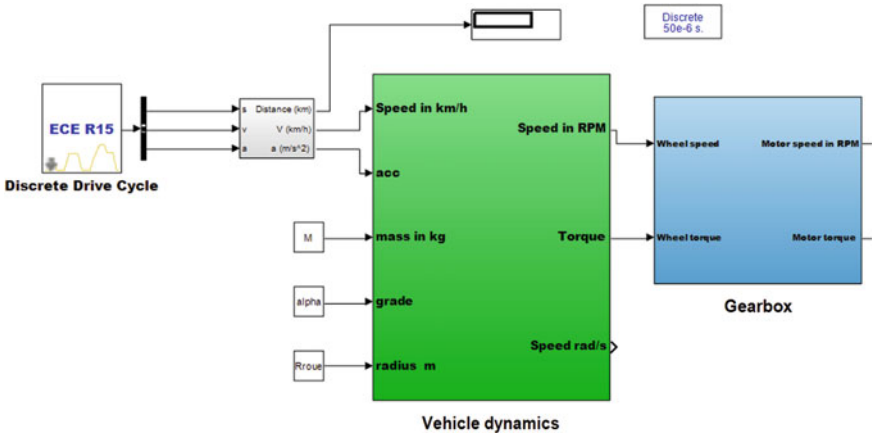

Fig. 2 Drive cycle based simulation model

The dynamics bloc model contains the mathematical formulas from (1) and (2), the wind speed is neglected since the vehicle is supposed to be driven with low speed in an urban area. Also, because acceleration force and grading force are related to vehicle mass, a particular acceleration level generates the same wheel force as a particular road grade level for any vehicle [8]. For this reason, the grading force is not considered in the drive cycle based analysis and acceleration performance study.

The simulation results in Fig. 3, show that for the ECE15 drive cycle, the vehicle's motor should allow a maximum speed of 4032 rpm and maximum torque of 26.93 N m.

From the results in Fig. 4, it is convenient to say that for the ECE15 cycle, the drive motor should be able to deliver a maximum power of 7.51 kW.

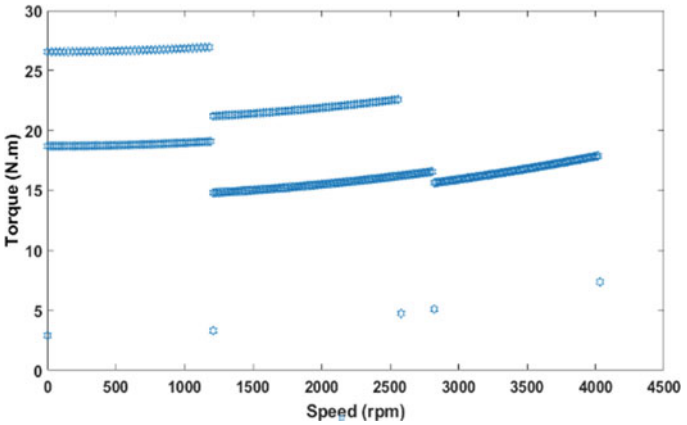

Fig. 3 Torque versus speed characteristics for ECE15 drive cycle

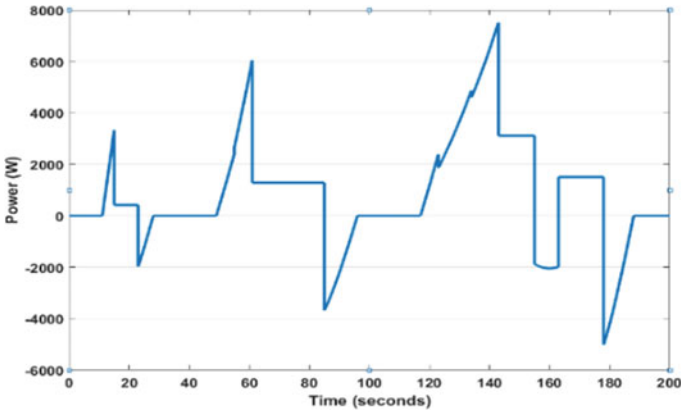

Fig. 4 Power versus time characteristics for ECE15 drive cycle

3.2 Acceleration Performance

The vehicle's acceleration capability is assessed by the time needed to accelerate the vehicle from zero speed to a certain speed.

From Eq. (1), the traction power P_t can be written as:

$$P_t = V \times F_D = V \times \left(\frac{1}{2}\rho CAV^2 + Mgfr + M\frac{\mathrm{d}V}{\mathrm{d}t}\right) \tag{3}$$

The wind speed and grading force were neglected as explained in the drive cycle based analysis. Thus the time t_a to accelerate from zero speed to a final speed can be expressed as:

$$t_a = \int_0^{V_f} \frac{M}{\frac{P_t}{V} - \left(Mgfr + \frac{1}{2}\rho CAV^2\right)} \mathrm{d}V \tag{4}$$

where V_f is the vehicle final speed (m/s).

According to [7] and Eqs. (3) and (4), the traction power can be expressed as:

$$P_t = \frac{M}{2t_a}(V_f^2 + V_b^2) + \left(\frac{2}{3}MgfrV_f + \frac{1}{5}\rho CAV_f^3\right) \tag{5}$$

where t_a is the acceleration time (s), V_b is the vehicle base speed and V_f is the vehicle final speed (m/s). These speeds are illustrated in Fig. 5a.

By observing Fig. 5, it is clear that the ideal tractive effort versus speed profile of a vehicle is very similar to the typical torque versus speed profile of an electric traction motor. Thus the vehicle speed V_b, which marks the end of the constant tractive effort region corresponds to the electric motor base speed. Whereas V_f is the final speed in acceleration, and V_{max} is the vehicle maximum speed.

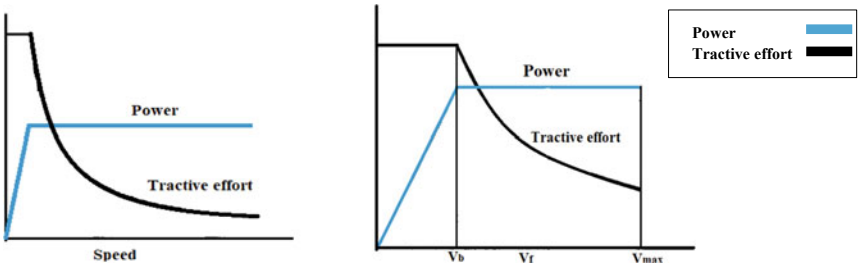

Fig. 5 **a** Ideal tractive effort and power versus speed profile of a vehicle. **b** Typical tractive effort and power versus speed profile of an electric traction motor

Table 2 Acceleration parameters

Quantity	Value
Base speed (km/h)	30
Final speed (km/h)	50
Acceleration time (s) from 0 to 50 km/h	12

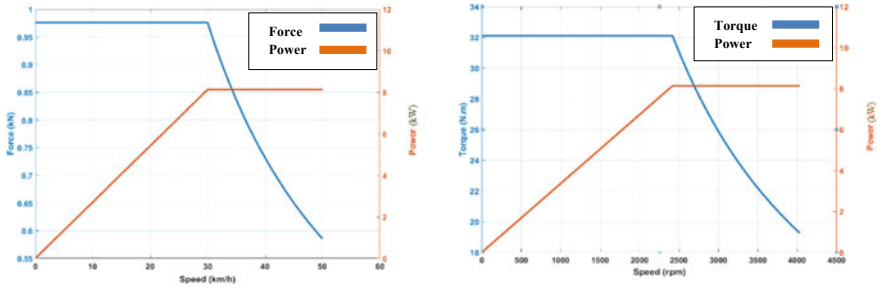

(a) (b)

Fig. 6 **a** Force and power versus speed profile of the vehicle. **b** Torque and power versus speed profile the traction motor

Generally, the acceleration performance of a vehicle is defined as the minimum time to accelerate from zero to 100 km/h. But since our top speed is 50 km/h, the acceleration time is chosen accordingly.

Based on Eq. (5), we made a simulation model to analyze the acceleration performance. Parameters from Tables 1 and 2 were used. The simulation results are presented in Fig. 6a, b.

By analyzing the acceleration profile of the vehicle in Fig. 6a, we can see that at the vehicle startup, the required force is 975.7 N, this force is constant until the vehicle reaches a speed of 30 km/h, where it becomes inversely proportional to speed. The power in the other hand, ramps up from zero at standstill position until 8131 W at 30 km/h, from this point the power is kept constant for the rest of the speed levels.

The vehicle acceleration performance in Fig. 6a was converted into an electric traction motor performance in Fig. 6b. This figure shows that the required torque in the constant torque region is 32.1 N m, whereas the motor should allow the power of 8131 W in the constant power region. The motor base speed is 2419 rpm and it should allow a top speed of 4032 rpm.

To wrap up, the electric traction motor must be able to handle a maximum power of 8131 W with a maximum torque value of 32.1 N m and a top speed of 4032 rpm.

3.3 Road Gradeability of the Vehicle

The highest slope that a vehicle can climb at a given speed while using the maximum power from the powertrain is referred to as its gradability.

For the gradability analysis, the Eq. (1) becomes:

$$F_D = F_a + F_r + F_g = \frac{1}{2}\rho C A V^2 + Mgfr\cos\alpha + Mg\sin\alpha \tag{6}$$

This equation can be further simplified to [8]:

$$F_D = F_a + F_r + F_g = \frac{1}{2}\rho C A V^2 + Mgfr + Mgp\% \tag{7}$$

where p% is the road grade percentage.

Using this equation, a simulation model was created. The parameters needed for this analysis are described in Tables 1 and 3.

According to Table 3, the vehicle should be able to climb a road grade of 6% while keeping a speed of 50 km/h. Additionally, the vehicle should be able to move in a grade level of 12%. Generally, battery electric vehicles specify a starting gradeability of 25% [15], but for our specific application, we only opted for the aforementioned gradeabilty level.

The results in Fig. 7a, b illustrate the vehicle's power and traction effort required for road loads at 6% an 12%. From Fig. 7a, b, we can deduce that the required torque to drive the vehicle with 50 km/h at a 6% grade is 19 N m with a power of 8018 W.

Table 3 Road gradeability specifications

Quantity	Value (%)
Grade at 50 km/h	6
Starting gradeability	12

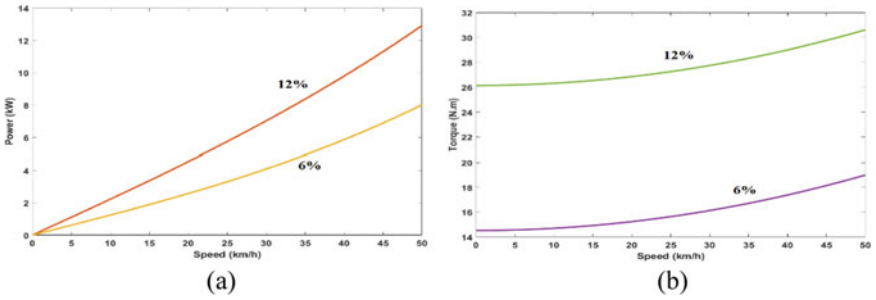

Fig. 7 **a** Power versus speed road loads. **b** Torque versus speed road loads

This same power level allows a speed of 34.6 km/h at a 12% grade with a torque of 28.2 N m.

As a result, the electric traction motor should be able to deliver a power of 8018 W, a torque of 28.2 N m and a speed of 4032 rpm.

3.4 Maximum Speed of the Vehicle

The maximum speed of the vehicle while cruising, describes the top speed that the motor can reach and maintain on a flat road. This means that the grading force and acceleration force are null. Leaving us only with the aerodynamic resistance force and the rolling resistance force. The Eq. (1) becomes:

$$F_D = F_a + F_r = \frac{1}{2}\rho C A (V - Vw)^2 + Mgfr \tag{8}$$

When cruising at maximum speed of 50 km/h, the motor required speed is 4032 rpm and the torque needed is 7.38 N m. Thus the power required is 3.1 kW.

4 Electric Traction Motor Sizing

Based on the conducted analysis in the previous section, we have extracted several conclusions regarding each performance.

First, the ECE15 drive cycle analysis revealed a maximum torque motor requirement of 26.93 N m, a maximum speed of 4032 rpm and peak power of 7.51 kW. As for the acceleration performance, we have reached an even higher torque requirement of 32.1 N m and power of 8131 W. Moving to the gradeabilty analysis, we have found that the motor should be able to deliver a power of 8018 W and torque of 28.2 N m. Finally, the maximum speed analysis showed that the needed power is 3.1 kW and 7.38 N m torque.

By comparing the results, it is clear that the acceleration performance has the highest power and torque requirements. Thus, the electric traction motor should be able to deliver the characteristics of Table 4.

Table 4 Motor specifications

Quantity	Value
Rated power (W)	8131
Maximum torque (N m)	32.1
Rated base speed (rpm)	2419
Maximum speed (rpm)	4032

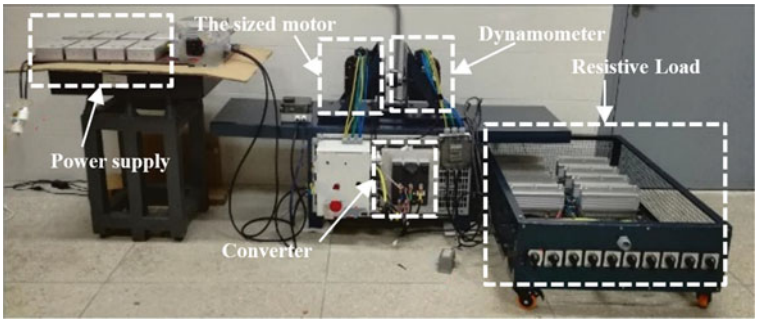

Fig. 8 The electric traction system test bench

Although this analysis was conducted on limited conditions for a specific electric vehicle, it could be generalized for other electric vehicles. The use of customized or other conventional drive cycles, different gradeability requirements, or maximum speeds do not affect by any means the analysis methodology. The motor ratings are chosen according to the maximum requirements of each performance.

After sizing and selection of the convenient motor, it is then integrated either directly in a EV or in a test bench for further evaluations.

In our case, the selected commercial motor was chosen to be close to ratings shown in Table 4 and was mounted on a realized test bench (Fig. 8) [9]. To validate its suitability for our three-wheeled vehicle, several motor performances tests are conducted using the test bench. The validation is based on Hardware-In-the-Loop simulation, by exploiting and comparing the simulation requirements of Sect. 3 of this paper and other simulation works with the actual motor performances.

5 Conclusion

In this paper, a sizing method for an electric traction motor of a battery electric vehicle is presented. This method is based on vehicle dynamics and performance analysis on different road loads. The electric lightweight vehicle is considered to be driven in road conditions similar to the ECE15 drive cycle. In addition, the vehicle requires a certain acceleration performance, gradeability and a maximum speed of 50 km/h. In order to investigate these characteristics and requirements, simulation work under MATLAB/Simulink is conducted. The results from these simulations, expose the needed electric motor requirements. Also, these results show that the maximum motor requirements for our vehicle can be deduced using the acceleration performance only. From these findings, the electric traction motor is selected and mounted in a developed test bench, in order to validate its use in the actual electric vehicle.

Acknowledgements This work was supported by ALTRAN Maroc (currently CAPGEMINI ENGINEERING) and the Moroccan Research Institute for Solar Energy and New Energies (IRESEN).

References

1. International Energy Outlook 2013—Energy Information Administration. https://www.eia.gov/outlooks/archive/ieo13/. Last accessed 2021/04/20
2. de Santiago, J., Bernhoff, H., Ekergård, B., Eriksson, S., Ferhatovic, S., Waters, R., Leijon, M.: Electrical motor drivelines in commercial all-electric vehicles: a review. IEEE Trans. Veh. Technol. **61**, 475–484 (2012). https://doi.org/10.1109/TVT.2011.2177873
3. Wappelhorst, S.: Europe's CO_2 emission performance standards for new passenger cars: lessons from 2020 and future prospects, p. 25. https://theicct.org/sites/default/files/publications/eu-ev-pv-co2-emission-performance-sept21.pdf
4. Ehsani, M., Gao, Y., Longo, S., Ebrahimi, K.M.: Modern Electric, Hybrid Electric, and Fuel Cell Vehicles. CRC Press, Boca Raton (2018). https://doi.org/10.1201/9780429504884
5. Park, H.-J., Lim, M.-S.: Design of high power density and high efficiency wound-field synchronous motor for electric vehicle traction. IEEE Access **7**, 46677–46685 (2019). https://doi.org/10.1109/ACCESS.2019.2907800
6. Sarigiannidis, A.G., Beniakar, M.E., Kladas, A.G.: Fast adaptive evolutionary PM traction motor optimization based on electric vehicle drive cycle. IEEE Trans. Veh. Technol. **66**, 5762–5774 (2017). https://doi.org/10.1109/TVT.2016.2631161
7. Ehsani, M., Gao, Y., Gay, S.: Characterization of electric motor drives for traction applications. In: IECON'03. 29th Annual Conference of the IEEE Industrial Electronics Society (IEEE Cat. No.03CH37468), vol. 1, pp. 891–896 (2003). https://doi.org/10.1109/IECON.2003.1280101
8. Grunditz, E.: BEV powertrain component sizing with respect to performance, energy consumption and driving patterns (2014)
9. El Houre, A., Yousfi, D., Bourzouk, Z., Chaker, M.: Development of an automated measurement platform for an electrical traction system test bench. In: Motahhir, S., Bossoufi, B. (eds.) Digital Technologies and Applications, pp. 1799–1808. Springer International Publishing, Cham (2021). https://doi.org/10.1007/978-3-030-73882-2_163
10. Tabbache, B., Djebarri, S., Kheloui, A., Benbouzid, M.: A power presizing methodology for electric vehicle traction motors. Int. Rev. Model. Simul. **6**, 29–32 (2013)
11. Akl, M., Ahmed, A., Rashad, E.E.: A wide component sizing and performance assessment of electric drivetrains for electric vehicles. Presented at the December 18 (2019). https://doi.org/10.1109/MEPCON47431.2019.9008195
12. Gillespie, T.D.: Fundamentals of Vehicle Dynamics. SAE International, Warrendale, PA (1992)
13. Arfa Grunditz, E., Thiringer, T.: Electric vehicle acceleration performance and motor drive cycle energy efficiency trade-off. In: 2018 XIII International Conference on Electrical Machines (ICEM), pp. 717–723 (2018). https://doi.org/10.1109/ICELMACH.2018.8507201
14. A Reference Book of Driving Cycles for Use in the Measurement of Road Vehicle Emissions: Version 3. IHS (2009)
15. 2013 Nissan Leaf. Advanced Vehicle Testing Activity. https://avt.inl.gov/vehicle-button/2013-nissan-leaf. Last accessed 2021/10/04

Output Feedback Stabilization of Positive T-S Fuzzy Continuous Delayed Systems

R. Oubah and O. Benmessaouda

Abstract This study solves the problematic of stabilization by output feedback control of Takagi-Sugeno (T-S) fuzzy delayed systems by using linear programming (LP) and imposing positivity in closed-loop. The Sufficient stabilization conditions are determined by applying the unique Lyapunov-Krasovskii function (LKF). In order to show the efficiency of our design approach, an example of a real plant is presented. The comparison between Linear Programming (LP) an Linear Matrix Inequality (LMI) is introduced.

Keywords Takagi-Sugeno fuzzy systems · Positive closed loop systems · Continuous systems · Sufficient conditions of stability in closed-loop · Linear programming

1 Introduction

The issue is about particular category of non linear systems termed Takagi-Sugeno models [1]. The Takagi-Sugeno fuzzy models can be defined as a group of linear models connected by non linear functions, termed membership functions, the variables of membership functions are dependant. The choice of premise variables that partition the space is real difficult problematic [2, 3].

Positive systems appear frequently in practical applications that's why this type of systems have been a large interest by researchers in recent years [4–8]. In [9], the positive Takagi-Sugeno fuzzy systems has been treated for the first time and results of stability by using Linear Matrix Inequality are presented.

This document focuses on analysis the terms of stabilization of T-S systems controlled by output feedback, while imposing positiveness of system in closed-loop. This analysis was made by linear programming (LP) approach. An example of a real

Ecole Marocaine des Sciences de l'Ingénieur.

R. Oubah (✉) · O. Benmessaouda
EMSI, Membre de Honoris United Universities, Marrakesh, Morocco

M. Bendaoud et al. (eds.), *The Proceedings of the International Conference on Electrical Systems & Automation*, https://doi.org/10.1007/978-981-19-0039-6_11

process is proposed. A comparison between results of Linear Programming approach and with the ones of extension results of [10] is presented.

The necessary terms of stability in closed-loop for continuous positive T-S systems were proposed in [11].

The sufficient terms of stabilization found by state feedback control for continuous positive Takagi-Sugeno systems with delay were proposed in [12]. Nevertheless, in this work, the proposed conditions of stabilization for continuous positive T-S systems with delay controlled by output feedback control are sufficient, and expressed in terms of Linear Programming.

The remainder of this paper is structured as follows: In part 2, the depiction of Takagi-Sugeno fuzzy systems with fixed state delay and the fuzzy control law based on the PDC structure is introduced. Afterwards, in Sect. 3, we give the conditions of stabilization of continuous Takagi-Sugeno delayed systems while imposing positivity in closed-loop. In Sect. 4, an application of a real process and comparison between obtained results of (LP) approach and with the ones of (LMI) are given to show the efficiency of our design approach. Some conclusions are given in Sect. 5.

Notation:

- N^T: Transpose of a real matrix N.
- $E \succ 0$: positive matrix if $e_{ij} \geq 0, \forall (i, j), \exists (i, j) : e_{ij} \succ 0$, where e_{ij} are elements of E.
- For a square matrix $Q > 0$, $(Q \geqslant 0)$ if $Q \in^{n \times n}$ is positive definite (positive semi definite, respectively).
- A is Metzler if $a_{ij} \geq 0$ whenever $i \neq j$, where a_{ij} are elements of A.

2 Problem Formulation

Especially, T-S fuzzy system is defined by fuzzy IF-THEN rules, which locally represent linear input-output relations of a system. The fuzzy system could be represented by:

Rule i: IF $z_1(t)$ is F_i^1 and ... and $z_p(t)$ is F_i^p Then:

$$\dot{x}(t) = A_i x(t) + A_{i1} x(t - \tau) + B_i u(t) \tag{1}$$

$$x(t) = \Psi(t) \succ 0, t \in [-\tau, 0] \tag{2}$$

$$y(t) = C_i x(t) \tag{3}$$

with $x(t) \in R^n$: the state, $u(t) \in R^m$: the control input, $y(t) \in R^l$: the output, τ: fixed delay, r: the number of IF-THEN rules, F_i^j: the fuzzy sets, and $z_1(t) \ldots z_p(t)$: premise variable.

The overall output feedback control law is given by:

$$u(t) = K_i y(t), \tag{4}$$

Systems (1) will be written as:

$$\dot{x}(t) = \sum_{i=1}^{r} h_i(z(t))(A_i x(t) + A_{i1} x(t-\tau) + B_i u(t)) \tag{5}$$

with

$$u(t) = \sum_{j=1}^{r} h_j(z(t)) K_j y(t) = \sum_{j=1}^{r} \sum_{s=1}^{r} h_j(z(t)) h_s(z(t)) K_j C_s x(t) \tag{6}$$

where $h_i(z(t)) = \frac{w_i(z(t))}{\sum_{i=1}^{r} w_i(z(t))}$; $w_i(t) = \prod_{j=1}^{p} F_i^j(z(t))$, with $h_i(z(t)) \geq 0; \forall t \geq 0$; $\sum_{i=1}^{r} h_i(z(t)) = 1$, $i = 1, 2, \ldots, r$ and $j = 1, 2, \ldots, p$.

By using (6), the system in closed-loop (5) is then described as:

$$\dot{x}(t) = \sum_{i=1}^{r} \sum_{j=1}^{r} \sum_{s=1}^{r} h_i(z(t)) h_j(z(t)) h_s(z(t)) \left[(A_i + B_i K_j C_s) x(t) + A_{i1} x(t-\tau) \right]$$

If C_s is equal to all of subsystems, the system will be written as:

$$\dot{x}(t) = \sum_{i=1}^{r} \sum_{j=1}^{r} h_i(z(t)) h_j(z(t)) \left[(A_i + B_i K_j C) x(t) + A_{i1} x(t-\tau) \right] \tag{7}$$

The objective of this job consists to proposed new sufficient terms of stabilization of T-S fuzzy systems controlled by output feedback while ensuring positivity of the state at each time. Our aim is to introduced an algorithm

Assumption 1 The matrix C_i is common to all subsystems: $C_1 = C_2 = \cdots = C_r = C$ and C_s is a positive matrix ($s = 1, 2, \cdots, r$).

Generally, this assumption is applicable to obtain r subsystems from a nonlinear system and its not limiting for T-S fuzzy systems for practical process, even matrices B_i are similar.

Definition 1 The T-S fuzzy system (5) is said to be controlled positive if, given any nonnegative initial state and any input function $u(t) \geq 0$, the corresponding trajectory remains in the positive orthant for all t: $x(t) \in R_+^n$.

Lemma 1 *[5] The autonomous delayed system (5) is positive if and only if A_i is a Metzler matrix and A_{i1} is a nonnegative matrix for $i = 1, \ldots, r$.*

The terms of stability in closed-loop for T-S system, expressed by LMIs approach are:

Theorem 1 *For positive matrices A_{i1}, if there exist a diagonal matrix $X = X^T \succ 0$, $V = V^T \succ 0$, matrices G_j; $i, j = 1, 2, \ldots, r$ and Z satisfying the following LMIs:*

$$\begin{cases} M_{ij} + M_{ji} \prec 0; \ \ i \leq j \\ CX = VC \\ A_i X + B_i G_j C \ \ is \ Metzler \end{cases}.$$

where

$$M_{ij} = \begin{pmatrix} XA_i^T + C^T G_j^T B_i^T + A_i X + B_i G_j C + Z & A_{i1} X \\ * & -Z \end{pmatrix}$$

Then system (7) with $P = X^{-1}$; $G_j = K_j V$ and $R = X^{-1} Z X^{-1}$ is asymptotically stable and controlled positive.

Proof To establish these conditions, the following Lyapunov-Krasovskii functional was used:

$$V(x(t)) = x(t)^T P x(t) + \int_{t-\tau}^{t} x(\upsilon)^T R x(\upsilon) d\upsilon \tag{8}$$

Note that these results are an extension of results given by [10] where the latter presented delay-dependent stabilization conditions of controlled positive T-S fuzzy systems with time varying delay with state feedback control.

3 Main Results

The terms of stability in closed-loop of T-S system (5) expressed by LP approach are introduced in this part.

Remark It's enough to demonstrate the stabilization of dual system (5), since we know that the dual system (5) is asymptotically stable, if and only if the system (5) is asymptotically stable.

Theorem 2 *For positive matrices A_{i1}, and C, system (7) is asymptotically stable and controlled positive if there exist a vector $\lambda \succ 0$, $\beta \succ 0$, vectors $y_1^j, \ldots, y_l^j \in R^m$ for $i, j = 1, \ldots, r$; $s = 1, \ldots, l$ and $e, f = 1, \ldots, n$; satisfying the following LPs:*

$$\begin{cases} A_i \lambda + B_i \sum_{s=1}^{l} y_s^j + \beta \prec 0, \\ A_{i1} \lambda - \beta \preceq 0, \\ \frac{1}{l} a_{ef}^i \left(\sum_{h=1}^{n} c_{sh} \lambda_h \right) + c_{sf} b_e^i y_s^j \succ 0, \ \ e \neq f \end{cases}$$

with

$$K_j = \left[\frac{y_1^j}{\sum_{h=1}^{n} c_{1h}\lambda_h}, \frac{y_2^j}{\sum_{h=1}^{n} c_{2h}\lambda_h} \ldots, \frac{y_n^j}{\sum_{h=1}^{n} c_{1h}\lambda_h} \right]; j = 1, \ldots, r;\ s = 1, \ldots, l$$

and

$$A_i = (a^i)_{ef}; e, f = 1, \ldots, n; B_i = \begin{bmatrix} b_1^i \\ b_2^i \\ \cdots \\ b_n^i \end{bmatrix}; C = \begin{bmatrix} c_1 \\ c_2 \\ \cdots \\ c_n \end{bmatrix} \text{ where } c_s = [c_{s1} \ldots c_{sn}].$$

Proof The choice of the Lyapunov-Krasovskii functional in this case will be:

$$V(x(t)) = x^T(t)\lambda + \int_{t-\tau}^{t} x^T(s)\beta ds; \lambda > 0, \beta > 0$$

The time derivative of the Lyapunov-Krasovskii functional is:

$$\dot{V}(x(t)) = \dot{x}^T(t)\lambda + x^T(t)\beta - x^T(t-\tau)\beta \tag{9}$$

replace the $\dot{x}^T(t)$ in Eq. (9) by the formula of the dual system of (7) which is as follows:

$$\dot{x}(t) = \sum_{i=1}^{r}\sum_{j=1}^{r} h_i(z(t))h_j(z(t)) \left[(A_i + B_i K_j C)^T x(t) + A_{i1}^T x(t-\tau)\right].$$

The expression of the derivative of the functional (9) becomes:

$$\begin{aligned}
\dot{V}(x(t)) &= \sum_{i=1}^{r}\sum_{j=1}^{r} h_i(z(t))h_j(z(t)) \left[x^T(t)(A_i + B_i K_j C)\right. \\
&\quad \left. + x^T(t-\tau)A_{i1}\right]\lambda + x^T(t)\beta - x^T(t-\tau)\beta \\
&= \sum_{i=1}^{r}\sum_{j=1}^{r} h_i(z(t))h_j(z(t)) \left[x^T(t)(A_i + B_i K_j C) + x^T(t-\tau)A_{i1}\right]\lambda \\
&\quad + \sum_{i=1}^{r}\sum_{j=1}^{r} h_i(z(t))h_j(z(t)) \left[x^T(t) - x^T(t-\tau)\right]\beta \\
&= \sum_{i=1}^{r}\sum_{j=1}^{r} h_i(z(t))h_j(z(t)) \left[x^T(t)\left[(A_i + B_i K_j C)\lambda + \beta\right]\right. \\
&\quad \left. + x^T(t-\tau)\left[A_{i1}\lambda - \beta\right]\right].
\end{aligned}$$

Finally,

$$\begin{cases} (A_i + B_i K_j C)\lambda + \beta \prec 0, \\ A_{i1}\lambda - \beta \preceq 0, \ \ i, j \in \{1, \ldots, r\} \end{cases} \tag{10}$$

implies $\dot{V}(x(t)) \prec 0$. To ensure that the trajectory remains in the positive orthant, matrices $A_i + B_i K_j C$ must be Metzler. Now, by letting $K_j = [K_1^j \ K_2^j \ldots \ K_l^j]$ where K_s^j are vectors in R^m, one has $K_j C\lambda = \sum_{s=1}^{l} K_s^j \left[\sum_{h=1}^{n} c_{sh}\lambda\right] = \sum_{s=1}^{l} y_s^j$, with $K_s^j \left[\sum_{h=1}^{n} c_{sh}\lambda\right] = y_s^j$. Consequently, inequality (10) can be written as

$$\begin{cases} A_i\lambda + B_i \sum_{s=1}^{l} y_s^j + \beta \prec 0, \\ A_{i1}\lambda - \beta \preceq 0, \end{cases}$$

and

$$K_j = \left[\frac{y_1^j}{\sum_{h=1}^{n} c_{1h}\lambda_h}, \frac{y_2^j}{\sum_{h=1}^{n} c_{2h}\lambda_h} \ldots, \frac{y_n^j}{\sum_{h=1}^{n} c_{1h}\lambda_h} \right]; \ \ j = 1, \ldots, r.$$

To ensure that the system (7) is positive in closed-loop, matrices $A_i + B_i K_j C$ must be Metzler for $i, j = 1, \ldots, r$.

Thus,

$$\left[A_i + B_i K_j C\right]_{ef} = a_{ef}^i + b_e^i \sum_{s=1}^{l} K_s^j c_{sf} = \sum_{s=1}^{l} \left[\frac{1}{l} a_{ef}^i + c_{sf} b_e^i \frac{y_s^j}{\sum_{h=1}^{n} c_{sh}\lambda_h} \right]$$

where a_{ef}^i are the components of matrix A_i; $e, f \in 1, 2, \ldots, n$.

$\frac{1}{l} a_{ef}^i + c_{sf} b_e^i \frac{y_s^j}{\sum_{h=1}^{n} c_{sh}\lambda_h} \succ 0$ implies $\sum_{s=1}^{l} \left[\frac{1}{l} a_{ef}^i + c_{sf} b_e^i \frac{y_s^j}{\sum_{h=1}^{n} c_{sh}\lambda_h} \right] \succ 0$

As C is a positive matrix and $\lambda \succ 0$, therefore $\sum_{h=1}^{n} c_{sh}\lambda_h \succ 0$.

Consequently $\frac{1}{l} a_{ef}^i \left(\sum_{h=1}^{n} c_{sh}\lambda_h \right) + c_{sf} b_e^i y_s^j \succ 0$ implies $A_i + B_i K_j C \succ 0$.

In case of the matrices A_{i1}, B_i are positive and A_i Metzler matrices, the control law has to be positive if required $y_s^j \geq 0$.

Corollary 1 *For positive matrices A_{i1} and B_i, matrices A_i Metzler, system (7) is asymptotically stable and positive if there exist a vector λ, β, vectors $y_1^j, \ldots, y_l^j \in$*

R^m for $i, j = 1, \ldots, r$; $s = 1, \ldots, l$ and $e, f = 1, \ldots, n$; satisfying the following LPs:

$$\begin{cases} A_i\lambda + B_i \sum_{s=1}^{l} y_s^j + \beta \prec 0, \\ A_{i1}\lambda - \beta \preceq 0, \\ y_s^j \succ 0, \end{cases}$$

with $K_j = \left[\frac{y_1^j}{\sum_{h=1}^{n} c_{1h}\lambda_h}, \frac{y_2^j}{\sum_{h=1}^{n} c_{2h}\lambda_h} \ldots, \frac{y_n^j}{\sum_{h=1}^{n} c_{1h}\lambda_h} \right]$; $j = 1, \ldots, r$; $s = 1, \ldots, l$.

4 Application to a Real Plant Model

Consider the process composed of two linked tanks of capacity 22 L each. This system can be described by:

$$\begin{aligned} \dot{x}_1(t) &= u_1(t) - q_{12}(t) - q_1(t) \\ \dot{x}_2(t) &= u_2(t) + q_{12}(t) - q_2(t) \end{aligned}$$

where x_i holds for the level in liters of tank, u_j represents the flow in liter/mn of pump j, q_{12} is the variation of the flow between the two tanks and q_i the loss flow of each tank. Applying the Torricelli law, one obtains:

$$\begin{aligned} q_1 &= \gamma_1\sigma_1\sqrt{2gx_1} = R_1\sqrt{x_1} \\ q_2 &= \gamma_1\sigma_2\sqrt{2gx_2} = R_2\sqrt{x_2} \\ q_{12} &= \gamma_{12}\sigma_1\sqrt{2g|x_1 - x_2|}sign(x_1 - x_2) \\ &= R_{12}\sqrt{|x_1 - x_2|}sign(x_1 - x_2) \end{aligned}$$

where γ_i and γ_{ij} are physical constants, σ_i is the tank section and g the gravity acceleration. The process model is then as follows:

$$\begin{aligned} \dot{x}_1(t) &= u_1 - R_1\sqrt{x_1} - R_{12}\sqrt{|x_1 - x_2|}sign(x_1 - x_2) \\ \dot{x}_2(t) &= u_2 - R_2\sqrt{x_2} + R_{12}\sqrt{|x_1 - x_2|}sign(x_1 - x_2) \end{aligned}$$

We note that the obtained model is nonlinear, so, we apply the classical transformation:

$\sqrt{x_i} = \frac{x_i}{\sqrt{x_i}} = x_i z_i$ with $z_i = \frac{1}{\sqrt{x_i}}$; $\frac{1}{\sqrt{|x_1 - x_2}} = \frac{z_1 z_2}{\sqrt{|z_2^2 - z_1^2|}}$ to procure a T-S fuzzy representation for this nonlinear system.

The corresponding model is then given by:

$$\begin{cases} \dot{x}(t) = A(z_1, z_2)x(t) + Bu(t) \\ y(t) = Cx(t) \end{cases}$$

where matrix $A(z_1, z_2)$ has the general following form:

$$A(z_1, z_2) = \begin{pmatrix} -R_1 z_1 - \frac{R_{12}}{\sqrt{|z_1^2 - z_2^2}} & \frac{R_{12} z_1 z_2}{\sqrt{|z_1^2 - z_2^2}} \\ \frac{R_{12} z_1 z_2}{\sqrt{|z_1^2 - z_2^2}} & -R_2 z_2 - \frac{R_{12}}{\sqrt{|z_1^2 - z_2^2}} \end{pmatrix}; B = I_2; C = I_2$$

The delayed model can be written as:

$$\begin{cases} \dot{x}(t) = (1 - \epsilon)A(z_1, z_2)x(t) + \epsilon |A(z_1, z_2)|x(t - \tau) \\ + Bu(t) \\ y(t) = Cx(t) \end{cases}$$

with $\epsilon \in [0, 1]$ and τ: fixed delay.

The following control is used:

$$u(t) = \sum_{j=1}^{r} h_j(z(t)) K_j C x(t) + L_j y_r,$$

where K_j ensures the stabilization together with the positivity in closed-loop while L_j achieves the tracking objective ($y(\infty) = y_r$).

The system in closed-loop becomes:

$$\begin{aligned} \dot{x}(t) &= \sum_{i=1}^{r} h_i(z(t)) \left((A_i + B K_i C) x(t) + A_{i1} x(t - \tau) + B L_i y_r \right) \\ &= G(h)x(t) + A_r(h)x(t - \tau) + BL(h)y_r; \end{aligned}$$

where $G(h) = A(h) + BK(h)C$, $A_r(h) = \sum_{i=1}^{r} h_i(z(t))A_{i1}$, Similar notation is used for $K(h)$ and $L(h)$.

The goal is $y(\infty) = y_r$, so $L(h) = \left[-C \left(G(h) + A_r(h) \right)^{-1} B \right]^{-1}$.

Present this system as the T-S model: by considering that $z_i \in [a_i; b_i]$; $i = 1, 2$ the four following rules are taken into account:

$$\begin{cases} If\ z_1\ is\ a_1\ and\ z_2\ is\ a_2\ Then: \dot{x} = A_1 x \\ If\ z_1\ is\ a_1\ and\ z_2\ is\ b_2\ Then: \dot{x} = A_2 x \\ If\ z_1\ is\ b_1\ and\ z_2\ is\ a_2\ Then: \dot{x} = A_3 x \\ If\ z_1\ is\ b_1\ and\ z_2\ is\ b_2\ Then: \dot{x} = A_4 x \end{cases}$$

The membership functions are given by:

$$h_1(k) = f_{11}(k)f_{21}(k); \quad h_2(k) = f_{11}(k)f_{22}(k);$$
$$h_3(k) = f_{12}(k)f_{21}(k); \quad h_4(k) = f_{12}(k)f_{22}(k);$$

where $f_{i1}(k) = \frac{z_i(k)-b_i}{a_i-b_i}$ and $f_{i2}(k) = 1 - f_{i1}(k) = \frac{a_i-z_i(k)}{a_i-b_i}$; $i = 1, 2$.

The membership functions are obtained as:

$$h_1(k) = \frac{(z_1(k)-b_1)(z_2(k)-b_2)}{(a_1-b_1)(a_2-b_2)}; \quad h_2(k) = \frac{(z_1(k)-b_1)(a_2(k)-z_2(k))}{(a_1-b_1)(a_2-b_2)};$$
$$h_3(k) = \frac{(a_1-z_1(k))(z_2(k)-b_2)}{(a_1-b_1)(a_2-b_2)}; \quad h_4(k) = \frac{(a_1-z_1(k))(a_2-z_2(k))}{(a_1-b_1)(a_2-b_2)};$$

The obtained matrices A_i of the subsystems are:

$$A_1 = \begin{pmatrix} -R_1a_1 - \frac{R_{12}a_1a_2}{\sqrt{|a_1^2-a_2^2|}} & \frac{R_{12}a_1a_2}{\sqrt{|a_1^2-a_2^2|}} \\ \frac{R_{12}a_1a_2}{\sqrt{|a_1^2-a_2^2|}} & -R_2a_2 - \frac{R_{12}a_1a_2}{\sqrt{|a_1^2-a_2^2|}} \end{pmatrix};$$
$$A_2 = \begin{pmatrix} -R_1a_1 - \frac{R_{12}a_1b_2}{\sqrt{|a_1^2-b_2^2|}} & \frac{R_{12}a_1b_2}{\sqrt{|a_1^2-b_2^2|}} \\ \frac{R_{12}a_1b_2}{\sqrt{|a_1^2-b_2^2|}} & -R_2b_2 - \frac{R_{12}a_1b_2}{\sqrt{|a_1^2-b_2^2|}} \end{pmatrix};$$
$$A_3 = \begin{pmatrix} -R_1b_1 - \frac{R_{12}b_1a_2}{\sqrt{|b_1^2-a_2^2|}} & \frac{R_{12}b_1a_2}{\sqrt{|b_1^2-a_2^2|}} \\ \frac{R_{12}b_1a_2}{\sqrt{|b_1^2-a_2^2|}} & -R_2a_2 - \frac{R_{12}b_1a_2}{\sqrt{|b_1^2-a_2^2|}} \end{pmatrix};$$
$$A_4 = \begin{pmatrix} -R_1b_1 - \frac{R_{12}b_1b_2}{\sqrt{|b_1^2-b_2^2|}} & \frac{R_{12}b_1b_2}{\sqrt{|b_1^2-b_2^2|}} \\ \frac{R_{12}b_1b_2}{\sqrt{|b_1^2-b_2^2|}} & -R_2b_2 - \frac{R_{12}b_1b_2}{\sqrt{|b_1^2-b_2^2|}} \end{pmatrix};$$

The number of the LMIs to be solved are reduced because matrix B in this example is common.

The corresponding T-S model with fixed delay can be given as follows:

$$\begin{cases} \dot{x}(t) = \sum_{i=1}^{4} h_i(z(t))((1-\epsilon)A_ix(t) + \epsilon|A_i|x(t-\tau) + B_iu(t)) \\ y(t) = \sum_{i=1}^{4} h_i(z(t))C_ix(t) \end{cases} \tag{11}$$

The matrices A_i are Metzler and matrices A_{i1} and B_i are positive for the real plant model, thus, to design controllers ensuring stabilization of this kind of system, it's enough to solve the conditions of Theorem 1 and Corollary 1.

4.1 Simulation Results of Delayed System

The following results are obtained by using the conditions expressed by (LMI) presented in Theorem 1:

$$P = 1.0e^{-5} * \begin{pmatrix} 0.4421 & 0 \\ 0 & 0.4209 \end{pmatrix}; R = 1.0e{-}5 * \begin{pmatrix} 0.1553 & -0.0612 \\ -0.0612 & 0.1499 \end{pmatrix}$$
$$K_1 = \begin{pmatrix} 0.0203 & 0.0209 \\ 0.0220 & 0.0242 \end{pmatrix}; K_2 = \begin{pmatrix} 0.0311 & 0.0459 \\ 0.0483 & 0.0776 \end{pmatrix}$$
$$K_3 = \begin{pmatrix} 0.0842 & 0.0533 \\ 0.0560 & 0.0452 \end{pmatrix}; K_4 = \begin{pmatrix} 0.0265 & 0.0233 \\ 0.0245 & 0.0256 \end{pmatrix}$$

Closed-loop matrices are got as:

$$\hat{A}_1 = \begin{pmatrix} -0.3801 & 0.2302 \\ 0.2312 & -0.4058 \end{pmatrix}; \quad \hat{A}_2 = \begin{pmatrix} -0.2852 & 0.1710 \\ 0.1733 & -0.3965 \end{pmatrix}$$
$$\hat{A}_3 = \begin{pmatrix} -0.4462 & 0.2013 \\ 0.2040 & -0.3236 \end{pmatrix}; \quad \hat{A}_4 = \begin{pmatrix} -0.8236 & 0.4910 \\ 0.4922 & -0.7912 \end{pmatrix}$$

The following results are obtained by using the conditions expressed by (LP) presented in Corollary 1:

$$\lambda = \begin{pmatrix} 394.4 \\ 391.7 \end{pmatrix}; \beta = \begin{pmatrix} 58.41 \\ 57.87 \end{pmatrix}; y_1^1 = y_2^1 = \begin{pmatrix} 5.8598 \\ 9.3409 \end{pmatrix}$$
$$y_1^2 = y_2^2 = \begin{pmatrix} 5.7824 \\ 26.1641 \end{pmatrix}; y_1^3 = y_2^3 = \begin{pmatrix} 30.941 \\ 9.397 \end{pmatrix};$$
$$y_1^4 = y_2^4 = \begin{pmatrix} 31.23 \\ 25.85 \end{pmatrix};$$

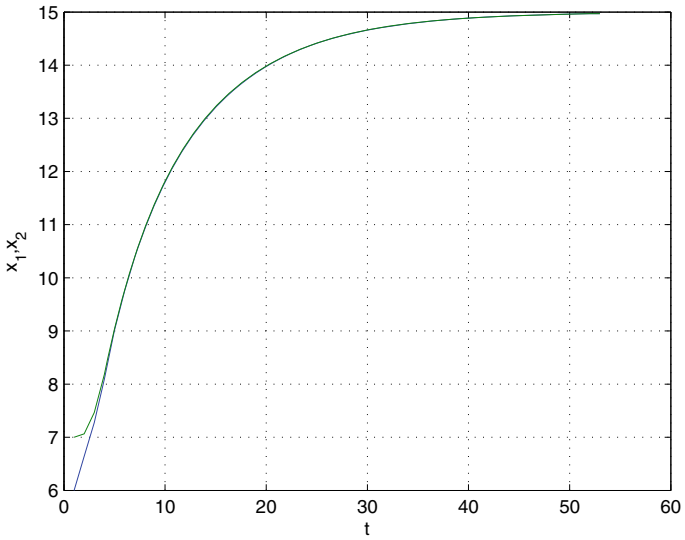

Fig. 1 Evolution of the states x_1 and x_2 (LMI)

$$K_1 = \begin{pmatrix} 0.0149 & 0.0150 \\ 0.0237 & 0.0238 \end{pmatrix}; \quad K_2 = \begin{pmatrix} 0.0147 & 0.0148 \\ 0.0663 & 0.0668 \end{pmatrix}$$
$$K_3 = \begin{pmatrix} 0.0784 & 0.0790 \\ 0.0238 & 0.0240 \end{pmatrix}; \quad K_4 = \begin{pmatrix} 0.0792 & 0.0797 \\ 0.0655 & 0.0660 \end{pmatrix}$$

Closed-loop matrices are got as:

$$\hat{A}_1 = \begin{pmatrix} -0.3856 & 0.2242 \\ 0.2329 & -0.4062 \end{pmatrix}; \quad \hat{A}_2 = \begin{pmatrix} -0.3016 & 0.1398 \\ 0.1914 & -0.4073 \end{pmatrix}$$
$$\hat{A}_3 = \begin{pmatrix} -0.4519 & 0.2270 \\ 0.1718 & -0.3448 \end{pmatrix}; \quad \hat{A}_4 = \begin{pmatrix} -0.7709 & 0.5475 \\ 0.5333 & -0.7508 \end{pmatrix}$$

We apply simulation with the following data: the trajectory reference $y_r = [15, 15]^T, \epsilon = 0.1$, and initial points $\Psi(t) = [6, 7]^T, t \in [-\tau, 0]$, results are obtained as (Figs. 1, 2, 3, 4, 5 and 6):

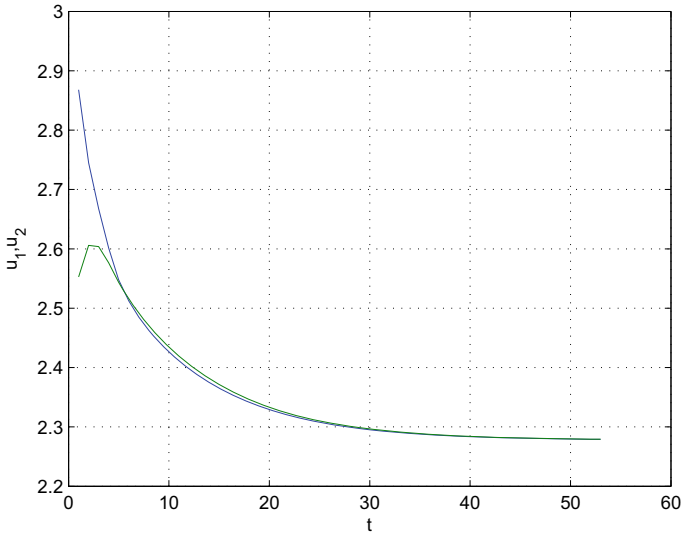

Fig. 2 Evolution of the two pump flows (LMI)

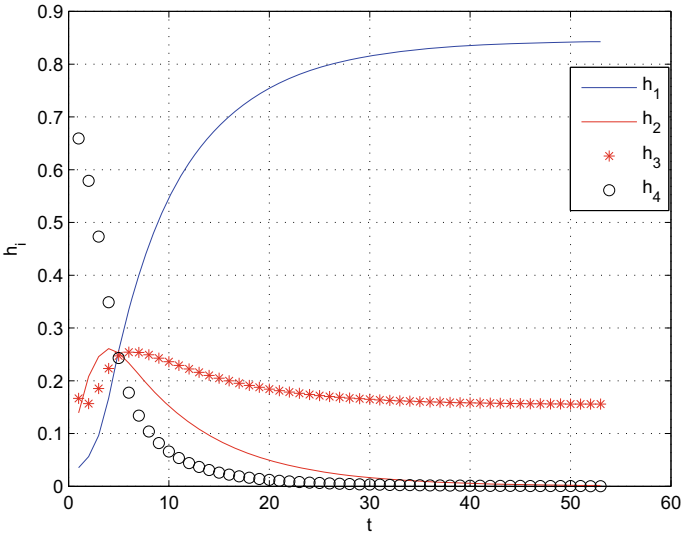

Fig. 3 Membership function (LMI)

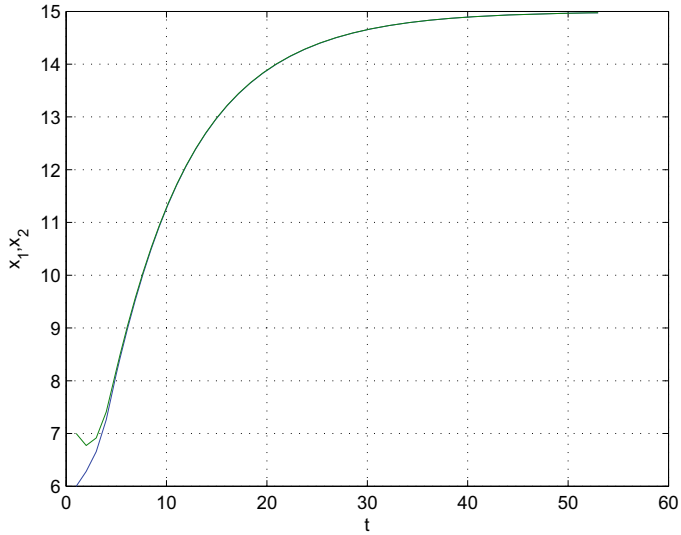

Fig. 4 Evolution of the states x_1 and x_2 (LP)

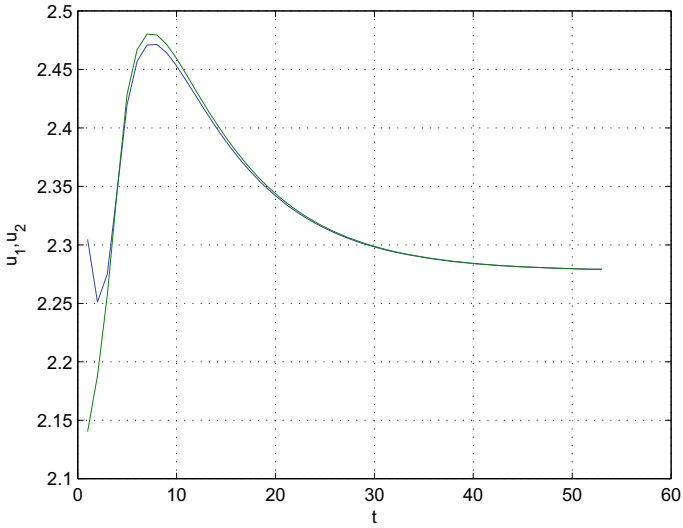

Fig. 5 Evolution of the two pump flows (LP)

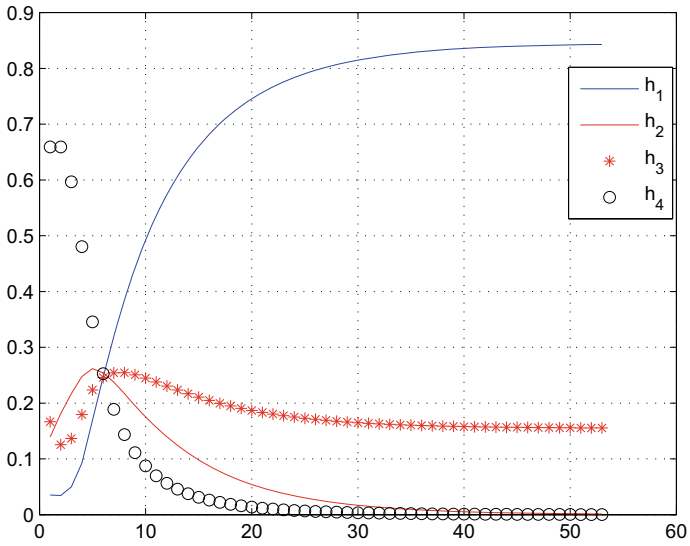

Fig. 6 Membership function (LP)

4.2 Results and Comparison

We apply the Corollary 1 on a real plant and we compare it with extension results presented on [10], the domain of feasibility obtained by linear programming is very large than LMI ones (Fig. 7).

5 Conclusion

The necessary conditions of stability and stabilization of positive T-S fuzzy continuous delayed systems are introduced in [11]. Later we were able to find the sufficient conditions of stability and stabilization of positive T-S fuzzy continuous delayed systems controlled by state feedback, this terms are presented in [12].

This work proposed sufficient conditions of stabilization of nonlinear systems controlled by output feedback, while imposing positivity in closed-loop, the T-S fuzzy techniques are used.

The study is performed by using a linear programming approach. Finally, an application to a real model of a process with two tanks was presented together with a comparison between our results and the ones of extension results of [10] expressed by Linear Matrix Inequality (LMI) method.

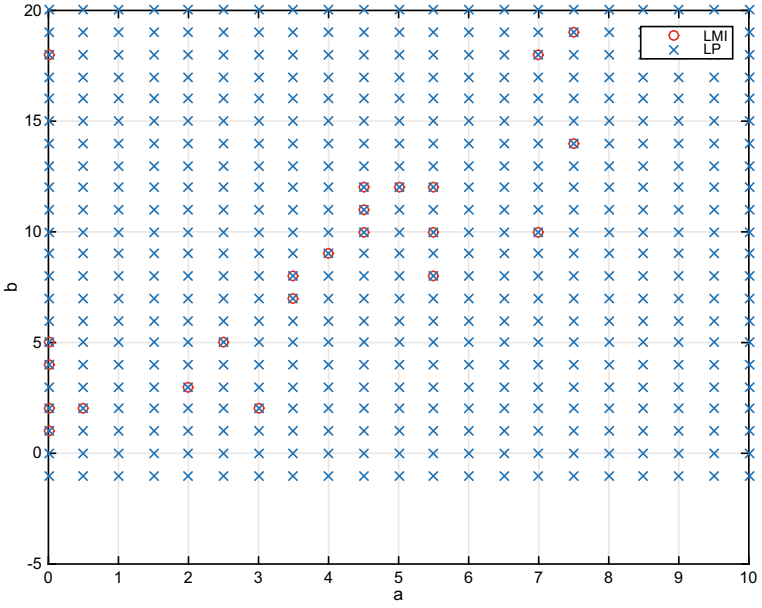

Fig. 7 Feasibility area of the LMI and LP methods

References

1. Takagi, T., Sugeno, M.: Fuzzy identification of systems and its application to modeling and control. IEEE Trans. Syst. Man Cybern. **15**(1), 116–132 (1985)
2. Gasso, K.: Identification des systèmes dynamiques non linéaires: approche multimodales. Thése de l'Institut National Polytechnique de Lorraine (2000)
3. Wang, L.X., Mendel, J.M.: Fuzzy basis functions, universal approximation and orthogonal least-squares. IEEE Trans. Neural Networks **3**(5), 807–814 (1992)
4. Ait Rami, M., Tadeo, F.: Linear programming approach to impose positiveness in closed-loop and estimated states. In: 17th International Proceeding on Mathematical Theory of Networks and Systems, Kyoto, Japan (2006)
5. Hmamed, A., Benzaouia, A., Ait Rami, M., Tadeo, F.: Memoryless control to drive states of delayed continuous-time systems within the nonnegative orthant. In: Proceedings of the 18th World Congress, IFAC, Seoul, Korea, 6–11 July 2008
6. Kaczorek, T.: Stability of positive continuous-time linear systems with delays. Bull. Pol. Acad. Sci. Tech. Sci. **57**(4) (2009)
7. Farina, L., Rinaldi, S.: Positive Linear Systems: Theory and Application. Wiley, New York (2000)
8. Kaczorek, T.: Positive 1D and 2D Systems. Springer, Berlin (2002)
9. Benzaouia, A., Hmamed, A., El Hajjaji, A.: Stabilization of controlled positive discrete-time T-S fuzzy systems by state feedback control. Int. J. Adapt. Control Signal Process. **24**(12), 1091–1106 (2010)
10. Benzaouia, A., El Hajjaji, A.: Delay-dependent stabilization conditions of controlled positive T-S fuzzy systems with time varying delay. IJCIC **7**(4) (2011)
11. Benzaouia, A., Oubah, R., El Hajjaji, A., Tadeo, F.: Stability and stabilization of positive Takagi Sugeno fuzzy continuous systems with delay. In: 50th IEEE Conference on Decision

and Control and European Control Conference (CDC-ECC), Orlando, FL, USA, pp. 12–15 (2011)
12. Oubah, R., Benzaouia, A.: Stability and stabilization of positive Takagi-Sugeno fuzzy continuous systems with delay by linear programming. In: 5th International Conference on Systems and Control (ICSC 2016), Marrakesh, Morocco, pp. 25–27 (2015)

Control of Reverse Osmosis Process at a Brackish Water Desalination Station

Moumni Mohammed and Massour El Aoud Mohamed

Abstract Reverse osmosis (RO) membrane desalination has become the key solution for the saltwater desalination process, because of its low cost and energy efficiency. However, desalination is a very complex process, due to the interactions between the inputs and the impact of each of them on the system outputs. The control of RO process operating parameters is a major concern, because it impacts directly the desalination plant's performance. The Maroc central station is taken as a case study, in this station, the feed flow, permeate flow and conversion rate are the three outputs parameters that are controlled by three separated loops. This control has not given good results. The main of this research is to study the use of PID controller based on MIMO dynamic model, while taking into consideration interactions between controller parameters. The suggested control design is examined by simulation using the Simulink/Matlab software. The results show clearly the performance of the used model to control RO process in optimum operating conditions, in order to extend the plant equipment's lifespan.

Keywords Desalination · Brackish water · Reverse osmosis · PID control

1 Introduction

The desalination of salt water by reverse osmosis (RO) technology has developed very significantly in recent years. Because of its high efficiency, it is extensively used in industrial seawater and brackish water treatment. Water supply constraints in different regions of the world have required the development of the (RO) desalination process to ensure the drinkable water provision of the people living in these areas. In operating of a reverse osmosis desalination process, it is essential that system condi-

M. Mohammed (✉) · M. E. A. Mohamed
LASTI, ENSA, Sultan Moulay Slimane University, Beni Mellal, Morocco
e-mail: massour@usms.ma

M. Bendaoud et al. (eds.), *The Proceedings of the International Conference on Electrical Systems & Automation*, https://doi.org/10.1007/978-981-19-0039-6_12

tions are supervised and controlled at appropriate set points to produce the required quantity of potable water while avoiding damage to the system [1]. RO desalination system is an important method to provide desalted water. It is an advanced water purification technology, where the semi-permeable membrane is used to desalinate the sea water or brackish groundwater. To make the water pass through the semi-permeable membrane, the high-pressure pump is used in this process. Due to the high pressure of the water passing through the membrane, the salt water becomes fresh water [2]. The performance of RO plants is quite sensitive to the quality of feed and plant operating conditions, that is, an RO plant requires a highly efficient pretreatment process and an accurate control system to maintain its operation close to the optimum conditions. Several researches have been interested in effect of changing in temperature and salinity of feed water on the RO plant's operating parameters [3, 4], which make it essential to implement control strategies of this process. RO desalination plants require an effective controller to increase their performance, as well as to maintain their operating parameters near optimal conditions, which results in higher efficiency, along with extending the lifetime of their membranes [5]. Several control strategies can be found in the literature on the conception and implantation of controllers for RO systems. The first multi-loop control system for RO was proposed by Alatiqi et al. [6] based on system identification. In the article [7], the authors performed a new genetic algorithm auto-tuned PID controller for the optimal control of simulated RO plant. In the research [8] : Particle Swarm Optimization (PSO) algorithm is used to tune the PID controller parameters in Reverse Osmosis (RO) desalination process. Janaa [2], have used PSO technique to tune PID controller for desalination systems, a simple model was presented to control the feed pressure and conductivity. A dynamic model was proposed by Chaaben [9] by using empirical transfer matrix, which models the small brackish water desalination unit as a MIMO (Multi Input Multi Output) system. The output parameters are the permeat flow rate Qp and the permeat salinity Cp, In addition, the input variables are the rotational speed of the motor pump and the opening of the reject valve. Using the model defined by Chaaben et al. [9], Phuc et al. [10] have controlled The permeat flow Qp and product water salinity Cp by manipulate variable speed pump and reject valve. This study outlines the current RO process at the desalination plant using the outcome of a Matlab/Simulink simulation. An analysis of the station's operating data has shown that the actual control strategy does not allow to reach the optimal and desired performance, due to the feed water (brackish water) quality fluctuation over time. For that reason, an innovative control design is being proposed to counterbalance the effect of the fluctuation, and thus extend the membranes lifespan.

2 Process Description

The RO desalination plant object of this study is composed from three lines of production. The schematic diagram of each line is shown in Fig. 1, the structure is based on two stages, where the concentrate flow of the first stage is the feed water for

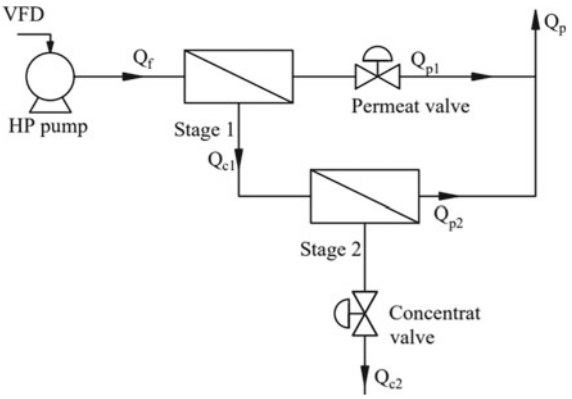

Fig. 1 RO process design

the second stage of RO components to produce more permeate. The permeate water collected from the first stage is added to the permeate water of the second stage. The role of the high pressure (HP) pump is to elevate the pressure of the feed water to the suitable level for the membrane. The required pressure is related to the concentration C_f and temperature T of the brackish water. The osmotic pressure increases with the concentration, hence, the operating pressure P_f must be higher than the osmotic pressure that corresponds to the concentration of the rejected flow at the membrane rack outlet, as well as membranes fouling. The feed water concentration of this plant varies during the year between 1 and 3 g/l, and its temperature varies between 7 and 32 °C. In order to manage the changing characteristics of the brackish water and to respect the operating conditions of this plant, the recommended conversion rate for each production line with its two stages is 75%, and the production flow rate of two stages is about 390 m^3/h.

To ensure control of the above instructions, each HP feed pump is equipped with a variable frequency drive (VFD) to vary the pump speed, which changes both the flow rate and the pressure of the membranes feed water. The modeling of the RO process was the main objective of the article [11]. The Matlab/Simulink software tools have been deployed to design a numerical model of RO process. The equations used for this objective are summarized in Table 1.

The conversion rate of an RO plant is defined by the ratio between the permeat flow rate Q_p and the feed flow rate Q_f.

$$Y = \frac{Q_p}{Q_f} \tag{6}$$

Since the configuration of RO process is based on double stage, each stage has a conversion rate Y_1 and Y_2.

$$Q_{p1} = Y_1.Q_f \tag{7}$$

$$Q_{p2} = Y_2.Q_{c2} \tag{8}$$

Table 1 RO process equations

Definition	Equation
Osmotic perssure (bar)	$\pi = i.C.R.T$ (1)
Permeate flux (ms^{-1})	$J_w = A_w(\Delta P - \Delta\pi)$ (2)
Solvent permeability coefficient($ms^{-1}.Pa^{-1}$)	$A_w(T) = A_0 \exp(6.433 - \frac{1885}{T})$ (3)
Permeat flow (m^3/h)	$Q_p = S.J_W$ (4)
Drop pressure across membrane (bar)	$\Delta P = (\frac{P_f + P_c}{2} - P_p) = \Delta\pi + (\frac{Q_p}{S.A_w})$ (5)

Where:
i : the number of ions dissociated in the case of an electrolyte;
P_f: Feed Pressure (bar);
C: concentration of salts in ($mol.m^{-3}$);
P_c: Concentrate Pressure (bar);
R: ideal gas constant R = 8.314 ($J.mol^{-1}.k^{-1}$);
P_p: Permeate Pressure (bar);
T: the absolute temperature of the solution in Kelvin;
S: Surface of the membrane (m^2)

The conversion rate of the RO process adopted in this plant, can be expressed as follow:

$$Y = \frac{Q_f - Q_{c2}}{Q_f} \tag{9}$$

3 Model of HP Pump with VFD

The most important equipment of a RO plant is the high pressure pump. It is used to ensure the desired pressure and flow rate to the membranes to desalinate the brackish water. The type of pumps installed at the RO desalination station object of this study is the centrifugal pump. The main objective of flow control is to maintain the required flow level in a pumping system or to change it within specific range. There are many control methods that can be applied to centrifugal pumping systems. For reverse osmosis plants where flow or pressure control is required, the most effective technology to monitor these parameters is pump speed control.Variable Frequency Drive(VFD) is the the most efficient controller and energy saver for mechanical machines in industries [12]. This technology improves the operational flexibility of the pump drive compared to throttling control, and it saves on energy costs. Currently, the performance of frequency inverters enables their use as an intelligent supervisor for the pump drive [13]. The centrifugal pump model described by Eq. (10), presents a model based on motor dynamics. Effects of pump flow rate and speed are shown in modeling equation. The equation is a form of Riccatti equation where a, b and c are determinable constants from pump geometry. H,Q and N are respectively head, flow rate and rotation speed of pump.

$$H = a.Q^2 + b.Q.N + c.N^2 \tag{10}$$

An interpolation of this equation is done using Matlab and the curves provided by the manufacturer to define the a, b, c coefficients, in order to model the HP pump installed in this station. The results obtained for these coefficients:

$$a = 3.27e^{-5}; b = 2.95e^{-5}; c = -3.173e^{-4} \tag{11}$$

Varying the rotational speed has a direct impact on the pumps' efficiency. By reducing the system speed, the intersection point of the system curve is displaced along a line of constant efficiency. The operating point is selected such that the pump continues to operate in its ideal range. The affinity laws are respected, which signifies that there is a substantial reduction in absorbed power as flow and head are decreased.

$$Flow : \frac{N_n}{N} = \frac{Q_n}{Q} \tag{12}$$

$$Head : \left(\frac{N_n}{N}\right)^2 = \frac{H_n}{H} \tag{13}$$

4 Control Valve

A control valve is a powered device that changes the fluid flow rate in a process control system. It is composed of three main parts: the valve body, the actuator that forces the valve stem to move, and the positioner that controls the position of the valve stem to match the control signal. A control valve is simply an orifice with a variable area of flow. The volumetric flow rate for incompressible fluid through an orifice is given by [14]:

$$Q = C_v \sqrt{\frac{\Delta P}{Sg}} \tag{14}$$

where:

Q Flow rate gpm;
ΔP Pressure drop across the valve psi;
Sg Fluid specific gravity (water = 1);
C_v Valve flow coefficient.

The flow coefficient C_v is a measure of the capacity of the valve body and trim, is also used to determine the valve size that will best allow the valve to pass the required flow rate while providing stable control of the process fluid. Each type of valve has a particular C_v coefficient which corresponds to the opening angle.

5 Design of Controllers

The design of the control implemented in the station under study is based on three separate loops:

- The first loop is designed to control the feed flow rate Q_f at 520 m^3/h by acting on the (VFD).
- The second loop controls the set value Y 75% of the conversion rate of the RO process system with its two stages by adjusting the valve installed at the reject.
- The third loop controls the set value 300 m^3/h of the first stage permeat flow Q_p1 by adjusting the valve installed at the permeat of the first stage. Indeed, the first loop is a cascade control loop based on two PI controllers with the output of the first controller provides the set point for the second controller, the second set point concernes the maximum value of recommended feed pressure represented in the simulation as saturation. The second PI controller commands the VFD of AC motor coupled with the HP pump, where the input of VFD is the frequency adjusted by the controller. Separately, the second and third loops control respectively the conversion rate of the system and the permeate flow rate of the first stage.

6 Results and Discussion

The first work carried out, was to present on Matlab/Simulink the configuration of the RO process control adopted at the station object of this study. The results obtained are illustrated in Figs. 2, 3 and 4.

The principle of the current RO process control in this station, especially in the first loop, is to keep the feed flow rate at the set value despite the change of the feed water parameters. These affect the permeability of the membranes and subsequently the HP pump pressure changes. The control adopted in this station is made by the variation of the drop pressure through the membranes. Which is considered as a regulation by fouling of the membranes. As a study, two cases were taken into consideration to evaluate the reaction of the controllers to maintain the set values (T = 22 °C; Cf = 1.6 g/l) and (T = 13 °C; Cf = 1.8 g/l). Using the simulation shown in the article [11], the pressure drop across the membranes created by these new values is calculated, then, this value is considered as a pressure drops for the HP pump which causes the change in flow rate in each case.

Figure 2 shows the stability of response in terms of HP pump flow rate, despite the change of feed water parameters, Fig. 4 shows the evolution of the permeate flow rate after the action of controller 2 and Fig. 3 shows the evolution of the conversion rate.

Several researches have shown that with the operation of the membranes, these last ones can lose its initial performances due to several factors. The most common factor for RO process is the membrane fouling. The major contributing factors to membrane fouling include [15]:

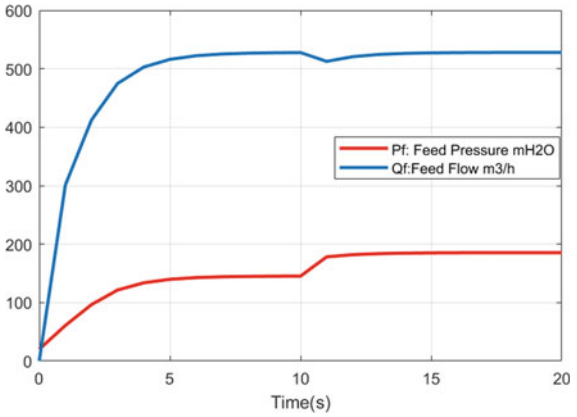

Fig. 2 Control of feed flow and pressure

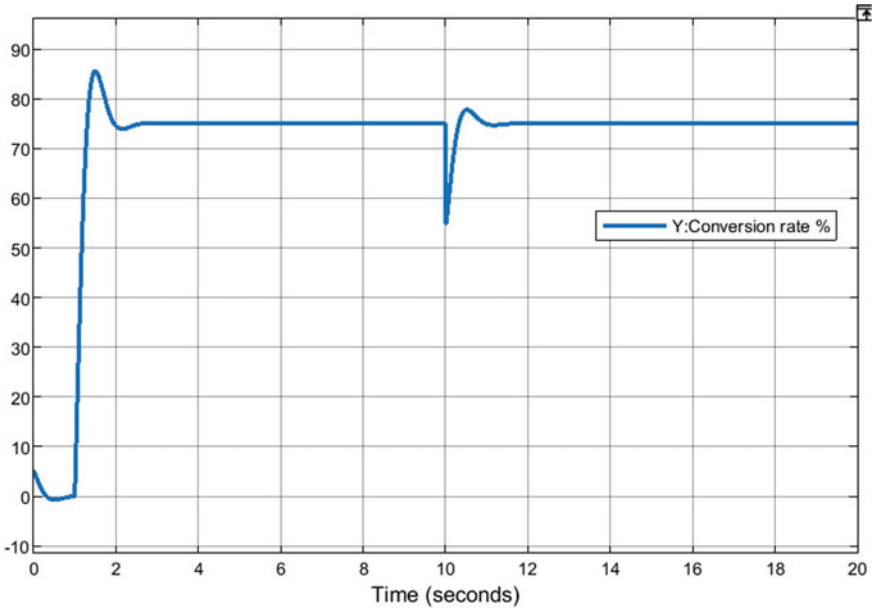

Fig. 3 Control of process conversion rate

- Feed chemistry and composition, pH, ionic strength, and foulant concentration.
- Concentration polarization (CP): CP can be broadly described as the deposition of rejected solutes on the membrane's surface, creating a region near the membrane with spatially varying concentrations known as the polarized layer.
- Membrane properties include membrane material type, porosity, hydrophobicity, surface charges, membrane morphology, and molecular weight cut-off (MWCO).

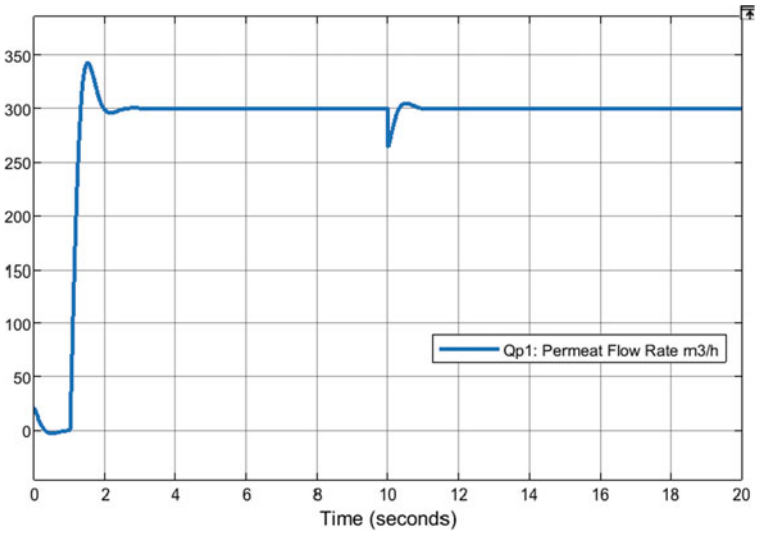

Fig. 4 Control of permeat flow rate Qp1

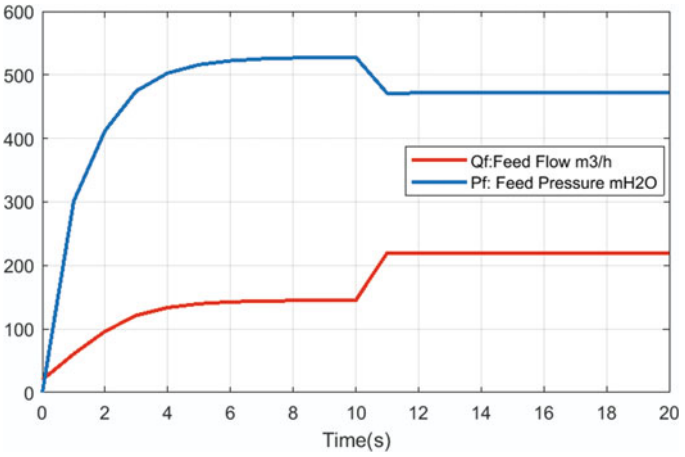

Fig. 5 Feed flow and pressure after membrane fouling

- Process operating conditions such as temperature, pressure, aeration, permeate flux, and several other hydrodynamic conditions.

This study is devoted to the fouling membranes due to the control of the operating parameters, in fact, after two years of operation of the plant, it was found that the feed pressure increased for the same quality of treated water (salinity and temperature). Since the pressure is limited at a maximum value, it seems that in some cases the feed rate doesn't reach the set value, although it was working normally at the beginning

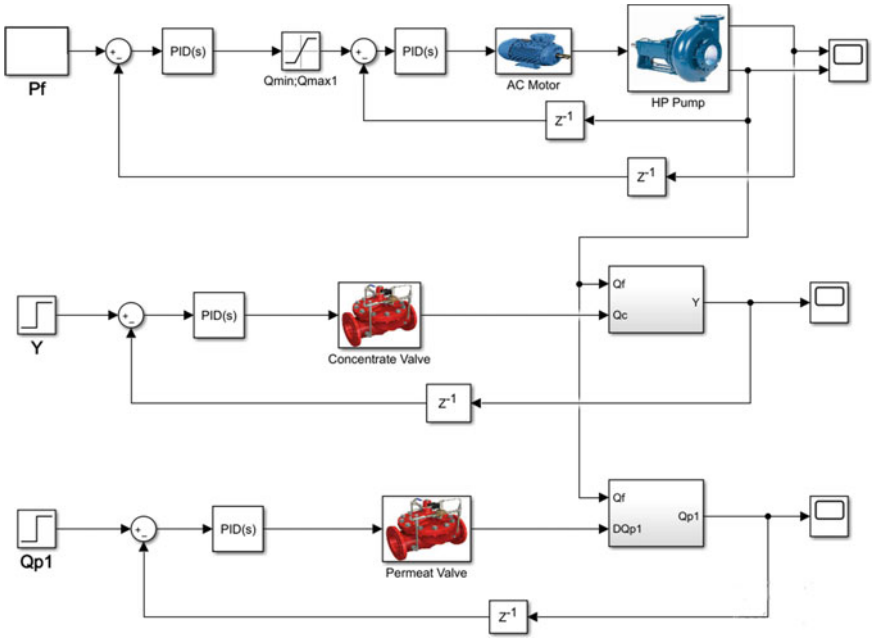

Fig. 6 Design of the proposed control

of the plant operation. In this case, the VFD cannot be switched to a higher speed as long as the maximum pressure is reached. Figure 5 illustrates this phenomenon. Given to this situation, another control is proposed, which consists of predicting the feed pressure before attacking the membrane by calculating this value using salinity and temperature sensors, where each new value of these parameters will generate the new feed pressure value. The control of the RO process will be considered as a MIMO system (Multi Input Multi Output), the three PID Controllers have the role of controlling the three set values (Output), feed pressure, permeate flow rate and the conversion rate.

These will act on the (INPUT) which are respectively the frequency delivered by the VFD of the HP pump, the opening of the permeate valve C_{v1} and the concentrate valve C_{v2}.

Since the variation of the feed flow rate impacts the change of the permeate flow rate and the concentrate flow rate, and using the equations developed previously (7,9), an interaction between the inputs and outputs of the system is established on Matlab/Simulink. The tuning of these 3 PID controllers is done by taking into account this interaction. The VFD is supposed to change the rotation speed to follow the calculated pressure set point, The VFD and the AC motor are represented in the simulation as shown in Fig. 6 by the block "AC Motor". The block "HP pump" is established by using the Eqs. 10, 12 and 13 and the coefficient a, b, c (11) which, approximately characterizes the HP pump installed in this plant.

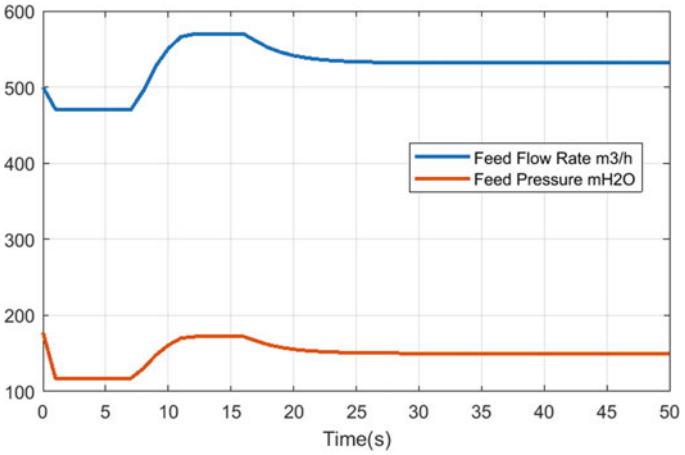

Fig. 7 The feed flow and pressure response of the proposed control

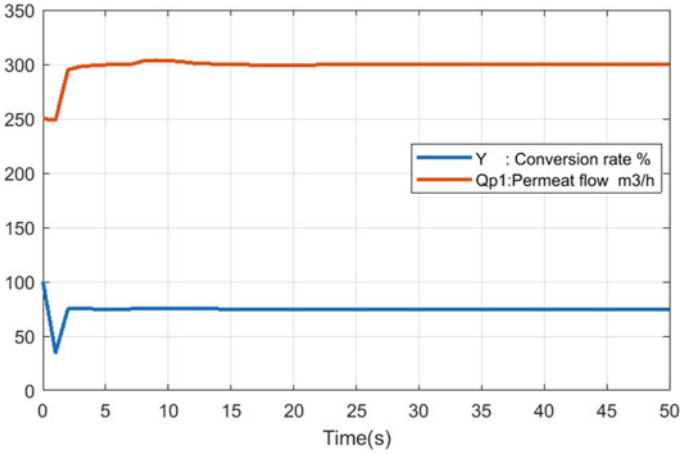

Fig. 8 The conversion rate response of the proposed control

As recommended in the literature [16], the flow rate delivered by the HP pump should not exceed 10% of the set flow rate defined by the manufacturer, in order to avoid disturbing the system operation. In order to study the performance of the proposed control, 3 cases of feed water quality are considered (T = 22 °C; C_f=1.6 g/l);(T = 13 °C; C_f = 1.8 g/l);(T = 25 °C; C_f = 2,7 g/l). The corresponding feed pressure in these cases is respectively 12 bar, 18.2 bar and 15.1 bar.

Figure 7 shows the evolution of the feed flow rate and feed pressure of the HP pump obtained by the new design of the proposed control.

It can be noted that the feed pressure follows the set point, and the feed flow rate delivered remains within the designated range [Qmin, Qmax], and this, despite the

change of the pressure set point corresponds to a new feed water quality, which confirms the stability of the controller even when the operating conditions are changed. Figure 8 shows the response of the RO process conversion rate Y and the permeate flow rate Q_{p1} of the first stage, after the action of the PID controllers on the permeate valves of the first stage and the concentrate. From the obtained results, it can be seen that these two controllers are also stable in spite of the change of the water quality, which guarantees the robustness and the performance of the chosen control.

7 Conclusions

In this work, the model of desalination water by RO process with double stages was developed. Then, the current control of this complex process was done using Matlab/Simulink. After an analysis of the obtained results on site, it turned out that the control affects the equipment performance of this station. As suggested, another effective control method was established in order to keep the life span of the membranes. The results gave satisfaction and showed the stability of the controllers towards the change of the operating conditions.

References

1. Bartmana, A.R., Zhua, A., Christofidesa, P.D., Cohena, Y.: Minimizing energy consumption in reverse osmosis membrane desalination using optimization-based control. J. Proc. Cont. **20**(2010), 1261–1269 (2010). https://doi.org/10.1016/j.jprocont.2010.09.004
2. Janaa, I., Asunthab A., Brindhab, A., Selvamc, K., Srinivasand, A.: Tuning of PID controller for reverse osmosis (RO) desalination system using particle swarm optimization (PSO) technique. Int. J. Cont. Theo. Appl. **10**(39) (2017). ISSN: 0974-5572
3. Al-Obaidi, M.A., Alsarayreh, A.A., Al-Hroub, A.M., Alsadaie, S., Mujtaba, I.M.: Performance analysis of a medium-sized industrial reverse osmosis brackish water desalination plant. Desalination **443**(27), 2–284 (2018)
4. Alsarayreh, A.A., Al-Obaidi, M.A., Al-Hroub, A.M., Patel, R., Mujtaba, I.M.: Evaluation and minimisation of energy consumption in a medium-scale reverse osmosis brackish water desalination plant. J. Cleaner Prod. **248**, 119220 (2019)
5. Raul, R.P., Javier, S.M., Gustavo, P.Z., Mario, E.S.-A.: Real-time implementation of an expert model predictive controller in a pilot-scale reverse osmosis plant for brackish and seawater desalination. Appl. Sci. **9**(14), 2932 (2019). https://doi.org/10.3390/app9142932
6. Alatiqi, I., Ghabris, A., Ebrahim, S.: Measurement and control in reverse osmosis desalination. Desalination **75**, 119–140 (1989)
7. Kim, J.S., Kim, J.H., Park, J.M., ParK, S.M., Choe, W., Heo, H.: Auto tuning PID controller based on improved genetic algorithm for reverse osmosis Plant. Int. J. Intell. Syst. Technol. **30**, 232–237 (2008)
8. Rathore, N.S., Anirudha, N.K.: PID controller tuning in reverse osmosis system based on particle swarm optimization. Int. J. Sci. Res. Publ. **3**(6), 1 (2013). ISSN 2250-3153
9. Chaaben, A.B., Andoulsi, R., Sellami, A., Mhiri, R.: MIMO modeling approach for a small photovoltaic reverse osmosis desalination system. J. Appl. Fluid Mech. **4**(1), 35–41

10. Phuc, B.D.H., You, S.-S., Lim, T.-W., Kim, H.-S.: Modified PID control with H loop shaping synthesis for RO desalination plants. Desalination Water Treatment (2016). https://doi.org/10.1080/19443994.2016.1156029
11. Moumni, M., Massour, M.: Modeling of reverse osmosis process at a brackish water desalination station. In: 2021 7th International Conference on Optimization and Applications (ICOA). IEEE (2021). https://doi.org/10.1109/ICOA51614.2021.9442632
12. Saidur, R., Mekhilef, S., Ali, M.B., Safari, A., Mohammed, H.A.: Applications of variable speed drive (VSD) in electrical motors energy savings. Renew. Sustain. Energy Rev. **16**(1), 543–550 (2012). https://doi.org/10.1016/j.rser.2011.08.020
13. Viholainen, J., Tamminen, J., Ahonen, T., Ahola, J., Vakkilainen, E., Soukka, R.: Energy-efficient control strategy for variable speed-driven parallel pumping systems. Energy Effi. **6**, 495–509 (2013). https://doi.org/10.1007/s12053-012-9188-0
14. Pipeline Rules of Thumb Handbook (Eighth Edition): Control Valves, pp. 187–225 (2014). https://doi.org/10.1016/B978-0-12-387693-5.00007-3
15. AlSawaftah, N., Abuwatfa, W., Darwish, N., Husseini, G.: A comprehensive review on membrane fouling: mathematical modelling, prediction, diagnosis, and mitigation. Water **13**, 1327 (2021). https://doi.org/10.3390/w13091327
16. Singh, R.: Membrane technology and engineering for water purification: application. Syst. Des. Operat. Elsevier Science, Book by Rajindar Singh (2014)

Breast Cancer Detection System Based on Microwave Imaging Antenna

Zerrad Fatima-Ezzahra, Makroum El-Mostafa, Taouzari Mohamed, and Jamal El-Aoufi

Abstract A microwave breast imaging system has been presented in this paper to detect an undesirable tumor in a breast phantom. The suggested antenna consists of a rectangular slotted patch, a tapered slot ground, and parasitic components in the shape of a four-star to improve far-field antenna characteristics like gain, which is critical for the breast imaging system. In the operating band, the developed antenna obtained a −10 dB impedance bandwidth of 6.3 GHz moved from 3.8 to 10.1 GHz and a 6.8 dBi maximum gain. Antennas are placed around the breast phantom once it is created to capture scattering parameter data for tumor characterization.

Keywords Breast tumor detection system · Microwave imaging · Antenna · Microwave

1 Introduction

Breast cancer is thought to be one of the most serious health problems that originate from breast tissue across the world. It is the cause of about a quarter of all female-related diseases worldwide each year. Every year, more than 2 million new instances of breast cancer are identified across the world, with a high mortality rate [1]. However, early detection improves the chances of survival by allowing for immediate treatment [2]. As illustrated in Fig. 1, GLOBALCAN documented 9.2 million cancer cases in women in 2020, with breast cancer accounting for the majority

Z. Fatima-Ezzahra (✉) · M. El-Mostafa
Faculty of Science and Technical, Hassan First University of Settat, Laboratory IMII, 26000 Settat, Morocco
e-mail: F.zerrad@uhp.ac.ma

T. Mohamed
Applied Sciences, Laboratory LISA, Hassan First University, 26100 Berrechid, Morocco

J. El-Aoufi
Laboratory of Aeronautical Telecommunication, International Academy of Civil Aviation, Mohammed VI, 27182 Nouaceur, Morocco

M. Bendaoud et al. (eds.), *The Proceedings of the International Conference on Electrical Systems & Automation*, https://doi.org/10.1007/978-981-19-0039-6_13

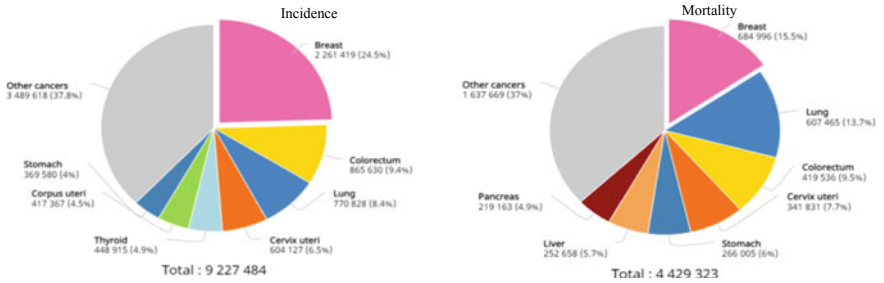

Fig. 1 Estimated number of new cancer cases and deaths in 2020

(24.5%). Current medical imaging methods that can be used to generate reconstructions of human tissue include ultrasound scanners, planar X-ray, X-ray computed tomography (CT), and nuclear-magnetic-resonance imaging (MRI). However, each of these methods has its own set of disadvantages [3]. Ultrasound, for example, is a low-cost technology that is especially helpful for some tissues, although it has contrast limits and cannot scan objects with significant acoustic impedance variations, such as air gaps and bones. Despite this, CT is very effective for imaging high-contrast subjects, but it exposes the patient to a lot of ionizing radiation, whereas MRI is non-ionizing and gives superb soft tissue imaging. Scanners are also quite expensive to buy and run. Microwave Imaging (MWI) has been recognized as a viable non-ionizing and non-invasive alternative imaging method for breast cancer detection because of all these problems. MWI is used to scan tissues based on changes in their dielectric properties [4]. In compared to standard testing, MWI has several benefits. To begin with, microwave imaging is free of ionizing radiations (X-rays), which are not allowed for screening purposes in women under the age of 50 [5]. Furthermore, during microwave imaging examinations, the patient appears to be more at ease since this method of measurement does not need painful breast compression. The core concept of MWI is to examine how the back-scattered signal varies as the electrical properties of tissues change. Antennas are important in MWI because they are used to impinge MW signals on human tissue [6]. Following that, a significant difference in the back-scattered signal will be utilized to detect cancerous tumor cells in the breast with a high dielectric constant value when compared to normal breast tissue. As a result, the antenna must fulfill characteristics [2], such as small size, a wide bandwidth with higher gain, high efficiency, the ability to function at low and high frequencies, and human tissue penetration. Moreover, Fig. 2 shows a block diagram of the imaging system. The antenna will be connected to the VNA through a switching matrix, and the antenna array will be held on a circular rotating platform. Using MATLAB script, the complete system will be managed by a processing unit. This program will be used to capture backscattered signals for subsequent post-processing [7]. A prototype imaging system for monitoring breast health and early identification of breast cancers is provided in this study. Antennas are used in the system, with one antenna acting as a transmitter and the other as a receiver. The following is the structure of this work: The details of the antenna design are

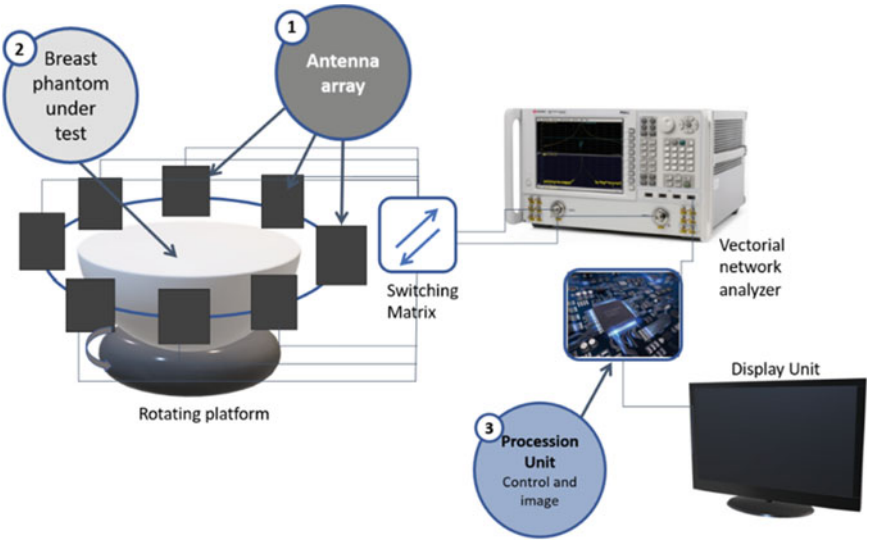

Fig. 2 Block diagram of the imaging system

discussed in Section II. Then, the effects of various geometrical parameters on the antenna performances and the numerical results are presented. In section III, a breast phantom simulation is presented. Section IV introduces the Imaging Performances and the system setup for breast phantom screening. While section V gives a final conclusion.

2 Antenna Performance

This section proposes a compact slotted microstrip patch antenna. The proposed antenna is made up of a rectangular slotted patch, a tapered slot ground and four-star shape parasitic components. The use of parasitic components increases the antenna's bandwidth and gain performance. In addition, the suggested prototype has 29*26.6*1.6 mm^3 in dimension with more than 6 dBi realized gain, 80% efficiency over the radiating bandwidth and it achieves an overall bandwidth (S11 < − 10 dB) of 6.3 GHz shifted from 3.8 to 10.1 GHz.

2.1 Antenna Design

Figure 3 shows the proposed antenna's geometric layout. The antenna's total dimensions are 29*26.6*1.6 mm^3 and it is designed on a Rogers RT/Duroid 5880 substrate

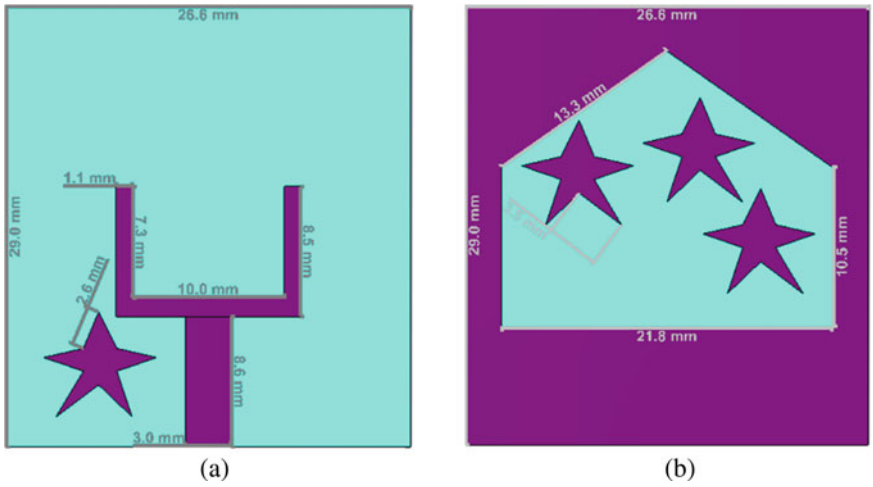

Fig. 3 The proposed antenna geometry. **a** Top view and. **b** Bottom view

with a dielectric constant of 2.2 and a loss tangent of 0.0009. In addition, a rectangular slotted radiating patch element linked to a 50 Ω microstrip-fed line, a tapered shaped slot ground and parasitic components in the form of a star on the substrate are used in the construction of the antenna to obtain a large bandwidth and a high gain in a small size antenna [8].

The presence of parasitic components, a rectangular slotted radiating patch element, and a tapered shaped slot ground all have a significant influence on impedance matching [9]. By including the star-shaped parasitic components, the side lobe level is reduced while the gain in the main lobe is raised. The parasitic resonator's influence on the reflection coefficient is seen in Fig. 4a. It illustrates that the parasitic resonator has a significant impact on lower bandwidth improvement. The improved structure with the resonator and slotted patch decreased the useable lower

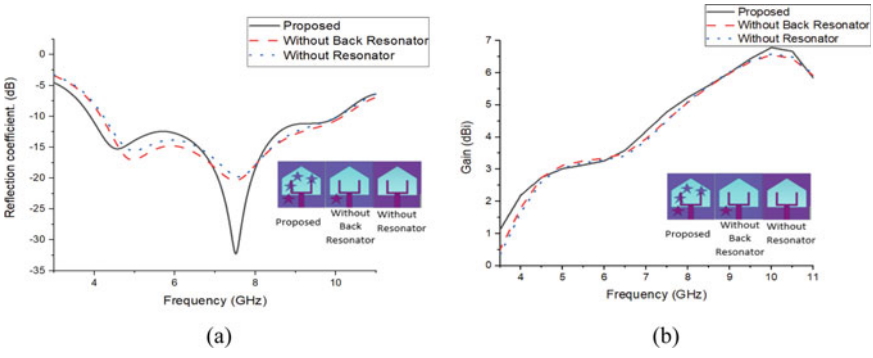

Fig. 4 Effects of the parasitic resonator, **a** on reflection coefficient and, **b** on the gain

frequency band by roughly 600 MHz (shifted from 4.22 to 3.88 GHz). Moreover, Fig. 4b shows how the antenna gain varies depending on the structure. According to the graph, the gain for the suggested design is better than for other configurations. By using the parasitic resonators, the peak gain was increased to 6.8 dBi from 6.5 dBi. Furthermore, additional current conducting paths are created when parasitic components are used. As a result, the capacitance and inductance of the prototype's input impedance are modified, which leads to modify the antenna properties.

2.2 Results and Discussions

Figure 5a, b shows the numerical surface circulation current of the proposed antenna for two different frequencies of 4.55 and 7.52 GHz. The most important surface current conducting zone of the suggested antenna is the fed line, especially at electric creation point. When compared to a higher frequency, the current distribution is more stable at a lower frequency because the current flow becomes non-linear at higher frequencies and the primary current conducts around the patch. Moreover, at Hight frequency, there exists a large portion of current around the cutting plane's edge. However, the presence of the parasitic element influences the current conducting route and antenna properties by allowing the operational frequency band to be extended further.

Figure 6 depicts the realized gain and efficiency of the proposed antenna. The efficiency across the BW is calculated by using the following equation [10]:

$$Efficiency = eff = (G\,(measured))/(D\,(theoretical)) * 100\% \quad (1)$$

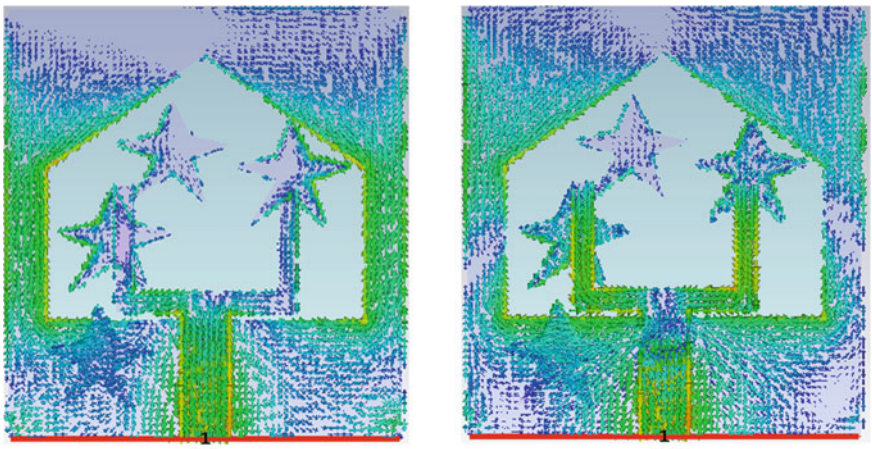

Fig. 5 Surface current distribution at, **a** 4.55 **GHz** and, **b** 7.52 GHz

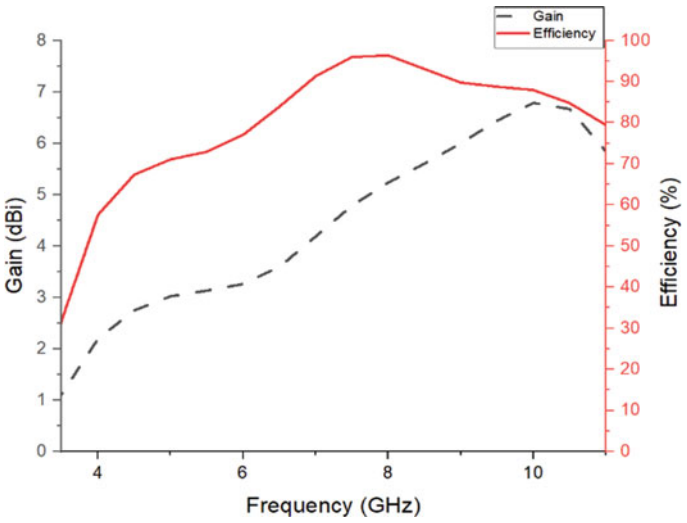

Fig. 6 Peak gain and efficiency

Where D (Directivity) and G (Power Gain) are the theoretical and the measured gain of the antenna respectively. Therefore, the simulated antenna has a maximum gain of 6.8 dBi at 10 GHz and an acceptable efficiency with a maximum of 96% at 8 GHz, which indicates that most of the power at the antenna's input is efficiently radiated out.

Figure 7 shows the simulated radiation pattern at elevation and azimuth planes, co-polarization and cross-polarization for two frequencies of 4.55 and 7.52 GHz. It is clear from the figure that the antenna radiates omnidirectionally in E and H planes. It is observed that with cross-polarization of the E plane, radiation patterns are slightly directional at low frequency of 4.55 GHz.

3 Breast Phantom Conception

A realistic breast model with a tumor is shown in Fig. 8. The proposed breast consists of two layers of biological material: the breast tissue layer, the skin layer and a tumor located 15 mm inside from the skin layer. Table 1 lists all the properties of the breast components [6].

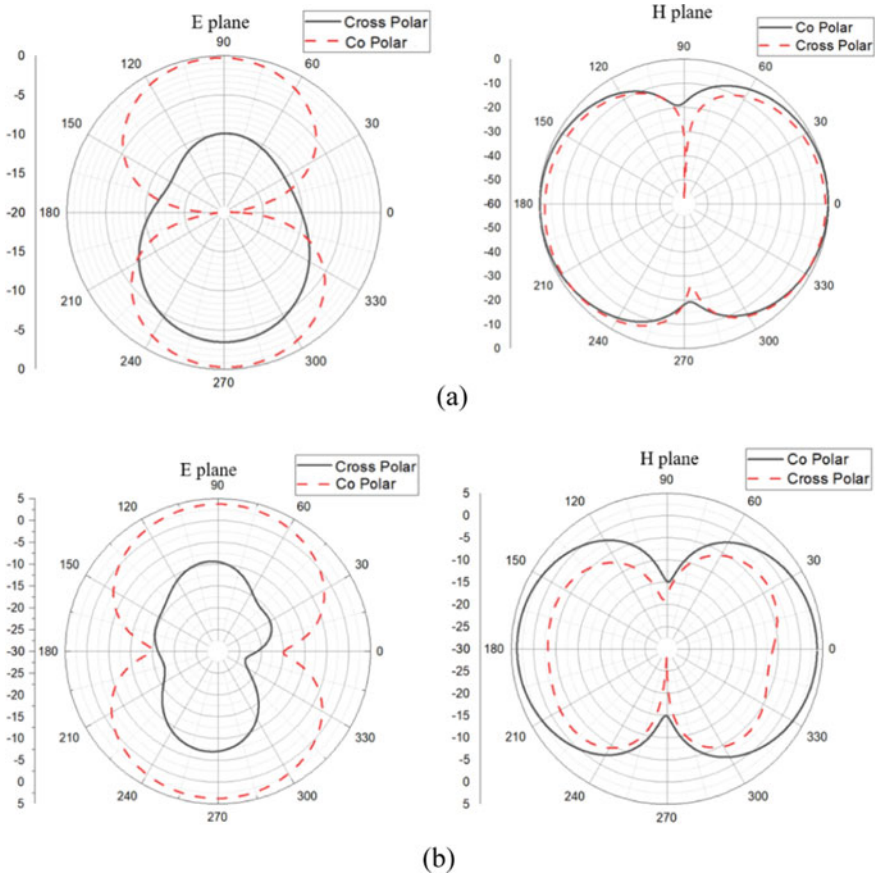

Fig. 7 Simulated radiation pattern at **a** 4.55 GHz and, **b** 7.52 GHz

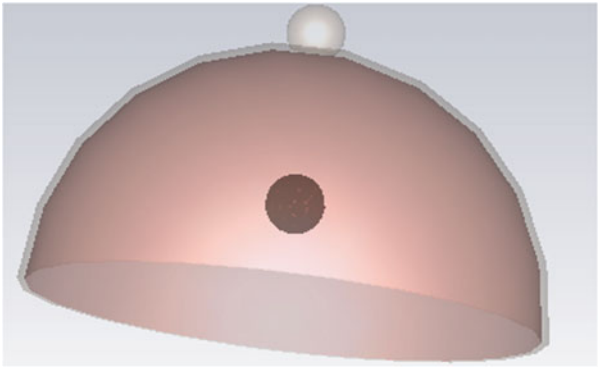

Fig. 8 3D model of the breast phantom with tumor

Table 1 Properties of breast phantom

Tissue	Permitivity (F/m)	Electrical constante (S/m)	Density (Kg/m3)	Width (mm)
Skin	36.7	2.34	1109	2.5
Fat	4.84	0.262	911	87.5
Tumor	67	4	1085	10

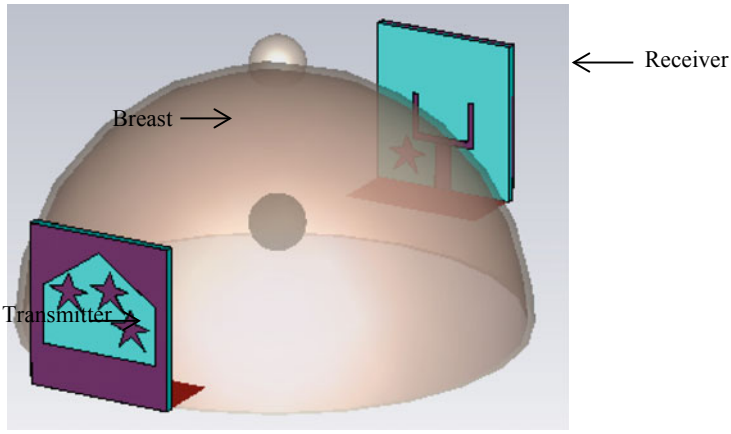

Fig. 9 Simulation setup for MWI system

4 Imaging System Performance

4.1 Microwave Imaging Setup

The proposed antenna will be employed as a radiating element in a MWI based breast cancer detection system. A modest set-up of two antennas surrounding a realistic breast model was developed to analyze the antenna behavior in the imaging system. The proposed breast tumor detection system is displayed in Fig. 9.

4.2 Microwave Imaging Measurement

The correlation between S11 and S21 for three distinct settings (open space, the breast model with and without tumor cell) is studied to evaluate the suggested system's performance. Two antennas facing and on the surrounding of the breast model at 15 mm from the skin layer are used to get the S-parameters. The first acts as a transmitter, while the second acts as a receiver. As a result of the dielectric characteristics of the breast and tumor tissue, the presence of the tumor could well be detected in

RX signals throughout the breast model. Therefore, when the wave passes through the sample apart from air, S11 displays the reflected proportion of the wave. Furthermore, the difference between the simulated S11 result in air and the front of the breast model should be understandable and not very much. Figure 10 shows the simulated S11 result in the first plot. The antennas work in the frequency range of 3.8–10.1 GHz. Additionally, the transmission response (S21) at the intended operating frequency BW [11] should be as flat as feasible to guarantee that the signal transmitted from the antenna to the sample has the least degree of distortion. The transceiver antenna system's S parameters are shown in Fig. 10. The plots of the free space S21 and the breast phantom S21 show a considerable difference. Furthermore, the free space transmission coefficient plot shows the flattest amplitude over most of the working bands. In addition, a considerable difference in RX signal is seen between the transmitter and receiver antennas for the scenarios of with and without tumor cell inside the breast model, and it is a significant magnitude for breast without tumor at most of the BW as compared to breast with tumor.

Figure 11 presents the imaging findings of the E-field distribution of the breast tumor screening device that has been proposed. The imaging of the breast model with the presence of the tumor is presented in Fig. 11a while Fig. 11b shows the outcome without the tumor. With a high-resolution image, the tumor's location and presence can be seen. However, the tumor's sensitivity is highlighted in Red, while the remainder of the normal breast tissue is highlighted in Blue. Because the dielectric properties of cancerous cells are higher than those of the breast tissue, tumor cell transmitting more signal than normal breast tissue. The imaging results show

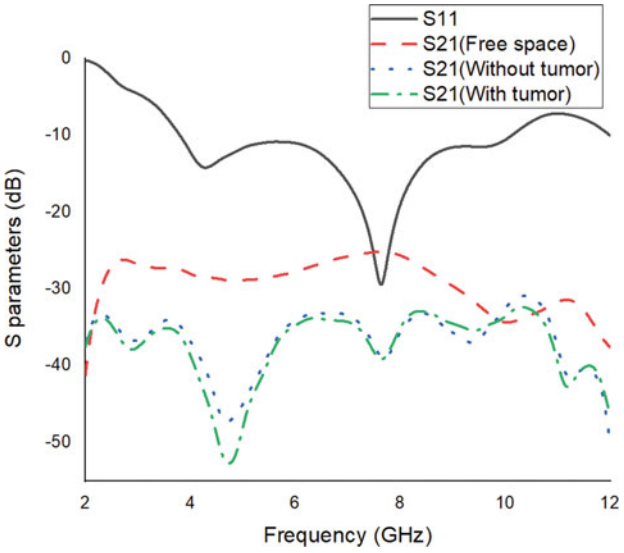

Fig. 10 Simulation setup for MWI system

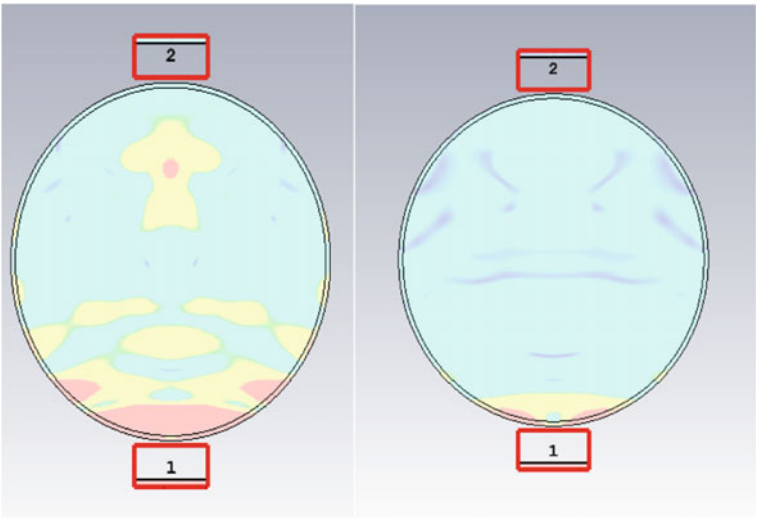

Fig. 11 Imaging results for, **a** unhealthy breast and, **b** healthy breast

a considerable difference in dispersed signals between the tumor and normal breast tissue as a result.

5 Conclusion

To sum up everything that has been stated so far, an imaging performance of a breast tumor detection system is presented in this article. According to the findings, the suggested antenna has a wider BW of 6.3 GHz (3.8–10.1 GHz). Additionally, good radiation efficiency of more than 80% and gain of 6.8 dBi are obtained. Because of its basic construction, small size, and UWB capability, the antenna is a strong candidate for MWI applications. At the end of the article, a simulation configuration with a breast phantom is looked into and therefore the system accurately locates and detects the presence of the tumor within the breast phantom.

References

1. Islam, M.T., Kibria, S., Misran, N.: Metasurface loaded high gain antenna based microwave imaging using iteratively corrected delay multiply and sum algorithm, pp. 1–14 (2019). https://doi.org/10.1038/s41598-019-53857-0
2. Martínez-Lozano, A., et al.: Uwb-printed rectangular-based monopole antenna for biological tissue analysis. Electron **10**(3), 1–20 (2021). https://doi.org/10.3390/electronics10030304

3. Karam, S.A.S., O'Loughlin, D., Oliveira, B.L., O'Halloran, M., Asl, B.M.: Weighted delay-and-sum beamformer for breast cancer detection using microwave imaging. Measurement **177** (2021). https://doi.org/10.1016/j.measurement.2021.109283
4. Vispa, A., et al.: UWB device for breast microwave imaging : phantom and clinical validations. Measurement **146**, 582–589 (2019). https://doi.org/10.1016/j.measurement.2019.05.109
5. Islam, M.T., Mahmud, M.Z., Islam, M.T., Kibria, S., Samsuzzaman, M.: A low cost and portable microwave imaging system for breast tumor detection using UWB directional antenna array. Sci. Rep. **9**(1), 1–13 (2019). https://doi.org/10.1038/s41598-019-51620-z
6. Zerrad, F. et al.: Multilayered metamaterials array antenna based on artificial magnetic conductor's structure for the application diagnostic breast cancer detection with microwave imaging. Med. Eng. Phys. **99**, 103737 (2022). https://doi.org/10.1016/j.medengphy.2021.103737
7. Array, M.N.S.: Experimental breast phantom imaging with metamaterial-inspired nine-antenna sensor array (2018). https://doi.org/10.3390/s18124427
8. Mahmud, M.Z., Islam, M.T., Almutairi, A.F., Samsuzzaman, M., Acharjee, U.K., Islam, M.T.: A parasitic resonator-based diamond-shaped microstrip antenna for microwave imaging applications. Electronics **8**, 434 (2019)
9. Ghimire, J., Choi, D.Y.: Design of a compact ultrawideband U-shaped slot etched on a circular patch antenna with notch band characteristics for ultrawideband applications. Int. J. Antennas Propag. **2019** (2019). https://doi.org/10.1155/2019/8090936
10. Kumar, V., Gupta, B.: On-body measurements of SS-UWB patch antenna for WBAN applications. AEUE Int. J. Electron. Commun. (2016). https://doi.org/10.1016/j.aeue.2016.02.003
11. Saeidi, T., Ismail, I., Alhawari, A.R.H., Wen W.P.: Near-field and far-field investigation of miniaturized UWB antenna for imaging of Near-field and far-field investigation of miniaturized UWB antenna for imaging of wood. vol. 035232, no. Mar 2019. https://doi.org/10.1063/1.5081762